

# Abstract

Title of Dissertation: Elemental Abundances via X-ray Observations  
of Galaxy Clusters and the  
InFOC $\mu$ S Hard X-ray Telescope

Wayne H. Baumgartner, Doctor of Philosophy, 2004

Dissertation directed by: Professor Richard F. Mushotzky  
Department of Astronomy

The first part of this dissertation deals with the oxygen abundance of the Milky Way interstellar medium. Previous measurements had shown that oxygen in the ISM was depleted compared to its abundance in the sun. This dissertation presents new measurements of the ISM oxygen abundance taken in the X-ray band by observing the oxygen 0.6 keV photoionization K-edge in absorption towards 10 galaxy clusters. These measurements show that the ISM oxygen abundance is 0.9 solar, much greater than earlier depleted values. The oxygen abundance is found to be uniform across our 10 lines of sight, showing that it is not dependent on the depth of the hydrogen column. This implies that the galactic oxygen abundance does not depend on density, and that it is the same in dense clouds and in the more diffuse ISM.

The next part of the dissertation measures elemental abundances in the galaxy clusters themselves. The abundances of the elements iron, silicon, sulfur, calcium, argon, and nickel are measured using the strong resonance K-shell emission lines in the X-ray band. Over 300 clusters from the *ASCA* archives are analyzed with a joint fitting procedure to improve the S/N ratio and provide the first average abundance results for clusters as a function of mass. The  $\alpha$  elements silicon, sulfur, argon and

calcium are not found to have similar abundances as expected from their supposed common origin. Also, no combination of SN Ia and SN II yields can account for the cluster abundance ratios, perhaps necessitating a contribution from a cosmologically early generation of massive population III stars.

The last part of this dissertation details the development of the Cadmium Zinc Telluride (CZT) detectors on the InFOC $\mu$ S hard X-ray telescope. InFOC $\mu$ S is a balloon-borne imaging spectrometer that incorporates multi-layer coated grazing-incidence optics and CZT detectors. These detectors are well suited for hard X-ray astronomy because their large bandgap and high atomic number allow for efficient room temperature detection of photons in the 20–150 keV band. The InFOC $\mu$ S CZT detectors achieve an energy resolution of 4.8 keV. A 2000 flight to measure the inflight background is discussed, as well as the results of a 2001 flight to observe Cyg X-1.

**Elemental Abundances via X-ray Observations  
of Galaxy Clusters and the  
InFOC $\mu$ S Hard X-ray Telescope**

by

Wayne H. Baumgartner

Dissertation submitted to the Faculty of the Graduate School of the  
University of Maryland at College Park in partial fulfillment  
of the requirements for the degree of

Doctor of Philosophy

2004

Advisory Committee:

Professor Richard F. Mushotzky, Advisor

Professor Marvin Leventhal, Chairman

Professor Niel Gehrels

Professor M. Coleman Miller

Professor Chris Reynolds

Professor Gregory Sullivan

© Wayne H. Baumgartner 2004

# Preface

Chronologically, the work in this dissertation began in 1998 when I started working with Dr. Jack Tueller at Goddard Space Flight Center on the CZT detectors for the InFOC $\mu$ S hard X-ray telescope. The detectors were in a very early stage at that time and I was put to the task of operating and evaluating a detector scheme realized by the University of Arizona as part of a medical imaging program. I calibrated and operated the device until it became clear that its unacceptable deadtime would not allow us to use it for astronomy. This high deadtime would be fine for medical imaging where the source rate could be increased by raising the dose of the radioactive tracer, but in high energy astronomy where every photon is precious we could not achieve the sensitivity we needed.

I then went on to test and calibrate a new sparse ASIC design that our group had commissioned from an independent ASIC designer. Data I took clearly showed that the device was not working as planned and that problems in its manufacture and design would not allow us to use it as the focal detector for InFOC $\mu$ S. Our group then decided upon a fallback SWIN detector based on the Swift mission's focal plane, and again I tested, calibrated, and worked with the engineers to successfully realize this detector. As a fallback design SWIN was not everything we hoped for, but it was what we needed and it did the job for us in balloon flights in 2000 and 2001.

The experimental nature of balloon missions made clear that it was entirely possible that InFOC $\mu$ S might not get any astronomical data at all. Being at Goddard and interested in things extragalactic, I started work with Dr. Richard Mushotzky on X-ray observations of galaxy clusters. Very soon I became heavily involved in a project to homogeneously analyze all the cluster data in the archives of the *ASCA* satellite. Dr. Keith Gendreau had started this work and explained to me the basic data reduction and got me started. I put together an early version of the database used for the *ASCA* Cluster Project (ACP) and extracted some results on the X-ray redshifts of clusters. Don Horner then took this project in hand and made major modifications and improvements to produce the ACP database that was the core of his dissertation and the source of his results on scaling relations in clusters. I also

started my own separate project to extract surface brightness profiles for over 300 clusters in the *ROSAT* archives. This was completed, but new results from *Chandra* and *XMM-Newton* made this work somewhat obsolete.

In the meantime, I was still heavily involved with InFOC $\mu$ S and was doing a lot of work to integrate the different detector systems of InFOC $\mu$ S into a flyable payload. The anti-coincidence shield was set up and calibrated and merged in with the CZT detectors. I also had a big hand in the cooling system and often came home from a day at the lab with clothes green from anti-freeze.

As flight time came closer for InFOC $\mu$ S and Jack became more involved with seeing that the pointing system and gondola were completed, I did a lot of the scientific work. I successfully proposed for time on *RXTE* for a simultaneous observation of two AGN and Cyg X-1. I also completed the difficult calculation that determined the sensitivity of InFOC $\mu$ S, and did some simulations to check out and plan for some possible targets of the science observations.

During the inevitable gaps in the detector and InFOC $\mu$ S work I continued on the ACP work and implemented a way to analyze the data to obtain new results on elemental abundances not yet readily observed. This work is in Chapter 4. When *XMM-Newton* data started arriving and we started to look at the clusters in those archives to verify my *ASCA* results, the oxygen edge arose as a serendipitous topic and led to the results on the galactic oxygen abundance in Chapter 3.

InFOC $\mu$ S finally flew its maiden science flight in 2001. Unfortunately, problems with the pointing didn't allow us to get high quality astronomical data, but the data we did receive in conjunction with some post processing allowed us to be the first to utilize multi-layer optics and CZT detectors to detect astronomical photons. InFOC $\mu$ S worked. I feel very lucky to have had the opportunity to start on a project near the very beginning, to build, calibrate, and run the detector, plan for the science, control the telescope in flight (no intermediate mission operations people here!), and reduce, analyze, and publish the results.

This work in this dissertation was done under the direction of Dr. Jack Tueller and my advisor Dr. Richard Mushotzky at NASA Goddard Space Flight Center. Prof. Marvin Leventhal graciously gave his additional advice and agreed to serve as my official supervisor in the Astronomy Department and chairman of my committee. Some of the figures in Chapter 2 are from the *ASCA* and *XMM-Newton* Users Guides. Other figures in Chapter 2 and Chapter 1 are from Fukazawa (1997). Dr. Mike Loewenstein provided substantial help with the SN model analysis and discussion in Section 4.8.2. The rest is my original work. Chapters 3 and 4 have been submitted to the *Astrophysical Journal*, and the new results in Part 2 have been published by the SPIE.

# Contents

List of Tables	vii
List of Figures	viii
<b>I Elemental Abundances via X-ray Observations Towards Galaxy Clusters</b>	<b>1</b>
<b>1 Galaxy Clusters</b>	<b>2</b>
1.1 Mass Composition . . . . .	3
1.1.1 Galaxy Content . . . . .	3
1.1.2 Dark Matter . . . . .	5
1.1.3 Hot Gas . . . . .	6
1.2 $\beta$ Model of the Cluster Gas Distribution . . . . .	7
1.3 Hydrostatic Equilibrium and the Cluster Total Mass Estimate . . . . .	8
1.4 Scaling Relations . . . . .	10
1.5 Cooling Flows . . . . .	12
1.6 X-ray Spectra of Galaxy Clusters . . . . .	13
1.7 Chemical Evolution and Elemental Abundances . . . . .	15
1.7.1 Supernovae . . . . .	16
1.7.2 Metal Transport Mechanisms . . . . .	18
<b>2 Satellites, Instruments, and Data Reduction</b>	<b>21</b>
2.1 <i>ASCA</i> . . . . .	21
2.1.1 The X-ray Mirrors . . . . .	22
2.1.2 The GIS Detector . . . . .	25
2.1.3 The SIS Detector . . . . .	28
2.2 <i>XMM-Newton</i> . . . . .	31
2.2.1 The MOS Detector . . . . .	32
2.2.2 The pn Detector . . . . .	33
2.3 Spectral Fitting . . . . .	36

<b>3</b>	<b>Oxygen Abundances in the Milky Way Using X-ray Absorption Measurements Towards Galaxy Clusters</b>	<b>40</b>
3.1	Introduction . . . . .	41
3.1.1	ISM Observations . . . . .	43
3.1.2	Solar Abundances . . . . .	45
3.2	X-ray Observations . . . . .	46
3.2.1	Sample Selection . . . . .	46
3.2.2	Data Reduction . . . . .	49
3.2.3	Extra Edge . . . . .	50
3.2.4	Spectral Fitting . . . . .	52
3.3	Results . . . . .	54
3.3.1	Hydrogen . . . . .	54
3.3.2	Galactic Oxygen Abundance . . . . .	63
3.3.3	Oxygen Abundance Variations . . . . .	64
3.4	Systematic Errors . . . . .	69
3.4.1	Error in the Extra Edge Determination . . . . .	69
3.4.2	Helium Abundance Errors . . . . .	71
3.5	Summary . . . . .	73
<b>4</b>	<b>Intermediate Element Abundances in Galaxy Clusters</b>	<b>78</b>
4.1	Introduction . . . . .	79
4.2	The Elements . . . . .	82
4.2.1	Carbon, Nitrogen and Oxygen . . . . .	83
4.2.2	Neon and Magnesium . . . . .	83
4.2.3	Aluminum . . . . .	84
4.2.4	Silicon and Sulfur . . . . .	84
4.2.5	Argon and Calcium . . . . .	85
4.2.6	Iron and Nickel . . . . .	85
4.3	Solar Abundances . . . . .	86
4.4	Observations and Data Reduction . . . . .	88
4.4.1	Sample Selection . . . . .	88
4.4.2	Stacking Analysis . . . . .	89
4.5	Results for Individual Elements . . . . .	93
4.6	Systematic Errors . . . . .	100
4.7	Comparisons . . . . .	105
4.7.1	Comparison to Other Cluster X-ray Measurements . . . . .	105
4.7.2	Comparison to Measurements in Different Types of Objects . . . . .	108
4.8	Supernovae Type Decomposition . . . . .	112
4.8.1	SN Fraction Analysis using Canonical SN Ia and SN II Models . . . . .	112
4.8.2	Expected Abundances from Standard SN Models . . . . .	116

4.8.3	Alternate Enrichment Scenarios . . . . .	119
4.8.4	Discussion . . . . .	121
4.9	Summary . . . . .	124
<b>II</b>	<b>The InFOC<math>\mu</math>S Hard X-ray Telescope</b>	<b>132</b>
<b>5</b>	<b>The InFOC<math>\mu</math>S Hard X-ray Telescope: Pixellated CZT Detector/Shield Performance and Flight Results</b>	<b>133</b>
5.1	Introduction . . . . .	134
5.2	Focal Plane . . . . .	137
5.3	Detector Test Results . . . . .	139
5.4	Flight Results . . . . .	145
5.4.1	The August 2000 Focal Plane Test Flight . . . . .	145
5.4.2	July 2001 Science Flight . . . . .	146
5.5	Conclusions and Future Plans . . . . .	150
5.5.1	Detector Improvements . . . . .	151
5.5.2	Future Flight Plans . . . . .	152
<b>6</b>	<b>Summary and Conclusions</b>	<b>156</b>
6.1	Galactic ISM Oxygen Abundance . . . . .	156
6.2	Elemental Abundances in Galaxy Clusters . . . . .	158
6.3	The InFOC $\mu$ S Hard X-ray Telescope and its CZT Detectors . . . . .	160
	<b>Bibliography</b>	<b>162</b>

# List of Tables

3.1	Cluster Reference Values . . . . .	47
3.2	X-ray Determined Galactic Absorption towards Galaxy Clusters . . .	56
3.3	Hydrogen Column Decomposition . . . . .	62
4.1	Solar Abundances . . . . .	87
4.2	Stack Parameters . . . . .	91
4.3	Galaxy Cluster Elemental Abundances by Number . . . . .	94
4.4	Classical Galaxy Cluster Elemental Abundances <sup>a</sup> . . . . .	95
4.5	Current Galaxy Cluster Elemental Abundances <sup>a</sup> . . . . .	97
4.6	Elemental Abundance Ratios . . . . .	98
4.7	Observed and Model Abundances . . . . .	117
5.1	InFOC $\mu$ S parameters. These numbers for the low energy mirror and detector document the details of the July 2001 science flight. . . . .	135

# List of Figures

1.1	The rich cluster Abell 1689 observed by the ACS and Hubble Space Telescope . . . . .	4
1.2	The X-ray image of the bright Coma cluster taken with <i>XMM-Newton</i>	7
1.3	The surface brightness distribution of the cluster Abell 1795 from <i>ROSAT</i> . . . . .	9
1.4	The observed cluster mass versus temperature relation from <i>ASCA</i>	11
1.5	The observed cluster luminosity versus temperature relation from <i>ASCA</i>	12
1.6	Model spectra of X-ray emitting hot gas at four different temperatures	14
1.7	Supernovae yields. The yield for each element is given in solar masses per supernova. SN II produce more of the alpha-elements, especially oxygen, while SN Ia produce more of the elements in the iron peak. . . . .	18
2.1	The <i>ASCA</i> X-ray telescope. . . . .	22
2.2	The effective areas of <i>ASCA</i> , <i>ROSAT</i> , and <i>XMM-Newton</i> . . . . .	23
2.3	Nested shell grazing incidence mirror design utilizing Wolter I optics in the <i>XMM-Newton</i> mirror. . . . .	24
2.4	The <i>ASCA</i> mirror . . . . .	24
2.5	Diagram of the <i>ASCA</i> GIS detector. . . . .	26
2.6	Energy resolution of the <i>ASCA</i> GIS and SIS detectors . . . . .	27
2.7	Diagram of the chip placement in the <i>ASCA</i> SIS detector . . . . .	29
2.8	The <i>XMM-Newton</i> X-ray telescope . . . . .	32
2.9	The field of view of the <i>XMM-Newton</i> EPIC cameras . . . . .	33
2.10	The quantum efficiencies of the <i>XMM-Newton</i> EPIC MOS and pn detectors. . . . .	35
3.1	The MW ISM optical depth in oxygen K-shell absorption as a function of the hydrogen column density for an ISM with standard solar abundances as given in Wilms, Allen, & McCray (2000) . . . . .	48
3.2	A map showing the location of the clusters in the ISM absorption sample . . . . .	49
3.3	A spectral fit to the bright quasar 3C 273 with the 3 CCD detectors of the EPIC camera on <i>XMM-Newton</i> . . . . .	51

3.4	The instrumental response of the MOS detector in the region of the oxygen edge . . . . .	52
3.5	Fits to the cluster PKS 0745-19 . . . . .	55
3.6	The X-ray total hydrogen column density plotted against the neutral hydrogen value derived from the 21 cm observations in Dickey & Lockman (1990) . . . . .	57
3.7	The correlation of $n_H$ derived from X-ray observations with other measures of the ISM towards the lines of sight of the 11 clusters in our sample . . . . .	58
3.8	The overabundance of the X-ray derived $n_H$ compared to the 21 cm derived value. . . . .	59
3.9	A comparison of the Arabadjis & Bregman (1999) X-ray derived $n_H$ values to those in this study. . . . .	60
3.10	The Galactic oxygen abundance plotted against the X-ray hydrogen column for 11 lines of sight towards galaxy clusters . . . . .	64
3.11	The distribution of $n_H$ and oxygen on the sky as computed by integrating along all lines of sight through a model of the galaxy . . . . .	67
3.12	A plot showing the constancy of the ISM oxygen abundance with respect to different overdensities of $n_{H_X}$ . . . . .	68
3.13	A comparison of results fit with and without the extra oxygen edge model component . . . . .	70
3.14	A demonstration of the effect of an uncertain helium abundance on oxygen abundance results . . . . .	72
4.1	Counts per cluster histogram . . . . .	90
4.2	Stack selection diagram . . . . .	92
4.3	The galaxy cluster elemental abundances as a function of temperature	96
4.4	The silicon and sulfur abundances ratios with respect to iron. . . . .	99
4.5	An absorbed power law fit to the <i>ASCA</i> 3C 273 data . . . . .	102
4.6	A comparison of abundance results using the GIS alone, the SIS alone, and the GIS and SIS combined . . . . .	103
4.7	The silicon and sulfur abundances as a function of temperature, compared to their abundance in stars . . . . .	109
4.8	The Type Ia and Type II supernovae yields . . . . .	113
4.9	The supernovae-type ratio derived from the silicon and sulfur abundances . . . . .	114
4.10	The supernovae-type ratio derived from the silicon and sulfur abundances, comparing the results from many different SN II models . . . . .	115
4.11	A decomposition of the intermediate element abundances into their nucleosynthetic origins based on Table 4.7 . . . . .	122

5.1	The effective area of the first InFOC $\mu$ S multilayer mirror . . . . .	136
5.2	The sensitivity of the InFOC $\mu$ S telescope . . . . .	137
5.3	The InFOC $\mu$ S detector cube assembly . . . . .	138
5.4	The InFOC $\mu$ S active shield . . . . .	140
5.5	Single pixel CZT spectra . . . . .	141
5.6	$^{133}\text{Ba}$ spectra in the SWIN detector . . . . .	143
5.7	A histogram of the FWHM energy resolution of the SWIN detector pixels at the $^{137}\text{Cs}$ 32.1 keV line. . . . .	144
5.8	The InFOC $\mu$ S Cyg X-1 light curve . . . . .	147
5.9	The InFOC $\mu$ S astronomical results . . . . .	148
5.10	InFOC $\mu$ S background spectrum . . . . .	149

# Part I

Elemental Abundances via X-ray

Observations Towards Galaxy

Clusters

# Chapter 1

## Galaxy Clusters

Most general works on galaxy clusters usually start out with the phrase, “Galaxy clusters are the largest objects in the universe,” for good reason. Galaxy clusters *are* the largest objects in the Universe in the sense that they are the biggest conglomerations of mass gravitationally bound to itself. This fact has many important ramifications in the field of astronomy: Galaxy clusters are formed in what were originally the first parts to condense out of the primordial matter of the Big Bang when the highest density peaks in the matter density distribution started condensing before the lower density peaks, galaxy clusters have a high ratio of dark matter to ordinary matter and are a fair sample of the Universe as a whole, they are bright objects in the X-ray band visible at high redshifts, they lie at the intersection of the cosmic filaments that trace out the matter density in the universe, they often are composed of smaller clusters and galaxies that have merged to form a larger cluster, and their deep gravitational potential wells are the repository for all the enriched matter lost by the constituent galaxies. It is the last statement that is the important one for this chapter. But first, a brief review of clusters and their general properties.

## 1.1 Mass Composition

Galaxy clusters are defined as gravitationally bound massive objects ranging from  $10^{14}$ – $10^{15} M_{\odot}$ . This roughly equates to X-ray temperatures of 1–10 keV. Clusters with masses between  $10^{12.5}$ – $10^{14} M_{\odot}$  are known as groups. Individual galaxies typically have masses below  $10^{12.5} M_{\odot}$ . The composition of this mass is described below.

### 1.1.1 Galaxy Content

Clusters of galaxies generally have between 20–1000 galaxies concentrated in a spherical region with a radius of about 1.5 Mpc. This is close to the definition used by Abell (1958) when compiling his optical catalog; in modern terms Abell’s definition would be  $R_A = 3h^{-1}$  Mpc (Sarazin 1988). Figure 1.1 is an optical image of the rich galaxy cluster Abell 1689, illustrating the concentration of the galaxies in the cluster core and the prominence of the galaxies in an optical image. The distribution of the galaxies within the cluster is similar to the distribution of stars within a globular cluster, and both distributions are typical of a relaxed system in gravitational equilibrium. The galaxies found in clusters differ from those in the field, containing more elliptical and S0 galaxies.

This distribution is often compared to that of an isothermal sphere. King (1962) showed that the globular density distribution can be empirically modeled as:

$$N(R) = N_0 \left[ 1 + \left( \frac{R}{R_C} \right)^2 \right]^{-3/2}, \quad (1.1)$$

where  $N_0$  is the central density and  $R_C$  is the core radius. The cluster galaxy distribution is often well fit by this model. The velocities of the individual galaxies in a cluster are large, and can be from 500–1300  $\text{km s}^{-1}$ .

Abell (1958) compiled a very large catalog of galaxy clusters found by visual



Figure 1.1: The rich cluster Abell 1689 observed by the ACS and Hubble Space Telescope

inspection of the Palomar Observatory Sky Survey plates. Abell's catalog of  $\sim 2000$  clusters was one of the largest early cluster catalogs, and remains important today as a flux-limited compilation of local clusters useful for observations at X-ray and other wavelengths.

### **cD Galaxies**

Large galaxy clusters are often found with a giant cD elliptical galaxy in their centers. The velocities of the cD galaxies are generally consistent with the center of the distribution of member galaxy velocities. This means that cD galaxies usually lie at the center of the cluster gravitational potential. cD galaxies are very extended and luminous, with luminosities about  $10^{11} L_{\odot}$  in the  $B$  band and outer envelopes extending farther out than usual for elliptical galaxies.

cD galaxies are usually found in clusters that appear uniformly relaxed, and not in clusters that show substructure or evidence for recent mergers.

### **1.1.2 Dark Matter**

Zwicky (1937) first pointed out that the measured velocity dispersion of the Coma cluster leads to a very high value for the mass to light ratio in the cluster, and that dark matter was needed to provide the mass to bind the cluster together. Zwicky's observation has held up with the passage of time, and the presence of dark matter in most astronomical systems has become one of the most important components of modern astronomy. X-ray observations have shown that dark matter makes up roughly 90% of the cluster mass. The dark matter dominates the cluster, and its gravitational potential sets the galaxy velocity dispersion and the temperature of the hot gas found throughout the cluster. The distribution of the dark matter is slightly more concentrated than that of the luminous matter in the cluster because the dark

matter has a low (or non-existent) cross section for self interaction. However, the dark matter is known to follow a similar mass distribution as the luminous matter, and is usually modeled by what is known as an NFW profile (Navarro, Frenk, & White 1997):

$$\frac{\rho(r)}{\rho_{\text{crit}}} = \frac{\delta_c}{(r/r_s)(1 + r/r_s)^2}, \quad (1.2)$$

where  $r_s$  is a scale radius,  $\delta_c$  is a dimensionless characteristic density, and  $\rho_{\text{crit}}$  is the critical density of the universe.

### 1.1.3 Hot Gas

Early X-ray observations in the 1960s discovered that clusters of galaxies were strong sources. Figure 1.2 shows the X-ray image of the Coma cluster with data from *XMM-Newton*.

Several theories were proposed to explain this unexpected emission, but it wasn't until the 7 keV line from ionized He-like iron was detected in the 1970s (Serlemitsos et al. 1977; Mitchell, Culhane, Davison, & Ives 1976) that it became clear that the X-ray emission was produced by hot gas caught in the cluster potential, known as the intra-cluster medium, or ICM. The detection of the iron line proved that the gas was hot, since only hot plasma would have iron in such a high ionization state. Once the nature of the emission was clear, the X-ray spectrum could easily be fit with a thermal bremsstrahlung model, and the high temperatures required for a good fit to the spectrum showed that the gas was in thermal equilibrium with the galaxies and their high velocity dispersions. The metallicity of the gas derived from the equivalent width of the ionized lines was 1/3 solar, indicating that the gas was not solely primordial but that it had been enriched by processed material from stars.

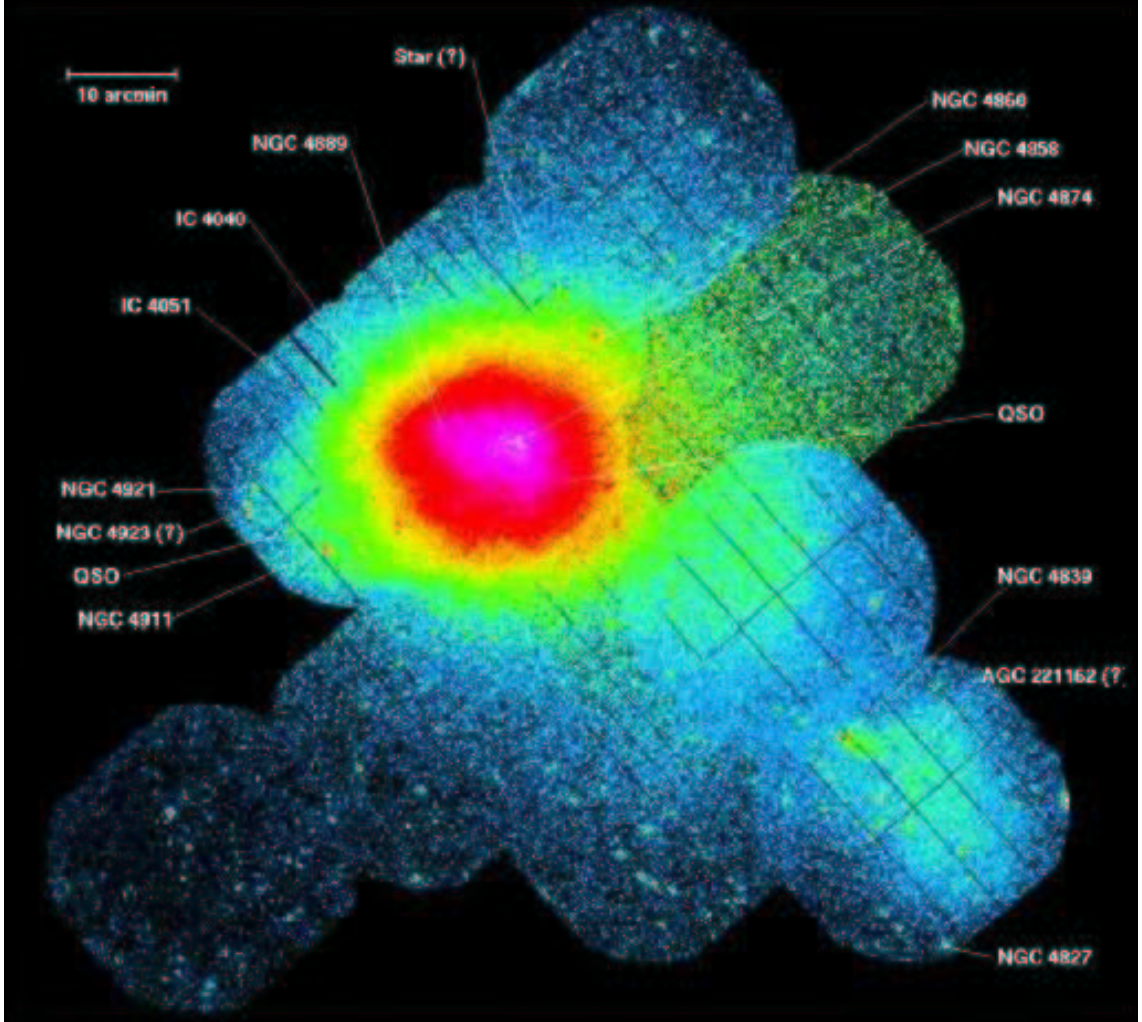


Figure 1.2: The X-ray image of the bright Coma cluster taken with *XMM-Newton*.

## 1.2 $\beta$ Model of the Cluster Gas Distribution

Cavaliere & Fusco-Femiano (1976) noticed the similarity of the gas distribution to that of the galaxies, and modeled the spatial distribution of the ICM with a modified King model,

$$\rho(r) = \rho_0 \left[ 1 + \left( \frac{r}{r_c} \right)^2 \right]^{-3\beta/2}, \quad (1.3)$$

where  $\rho$  is the gas density,  $\rho_0$  the central gas density,  $r_c$  the core radius, and  $\beta$  the asymptotic slope of the gas at large radii. This expression is known as the beta

model.

The luminosity of the gas goes as the integral of the emission measure,

$$L = \int \rho^2(r) \Lambda(T(r)) dV, \quad (1.4)$$

where  $\Lambda$  is the cooling function of the gas and is only mildly dependent on temperature ( $\Lambda \sim T^{-1/2}$  for  $T > 2$  keV) for thermal bremsstrahlung in the X-ray band. With the assumption of isothermality, the surface brightness distribution of the gas obtained in this way is

$$I(b) = I_0 \left[ 1 + \left( \frac{b}{r_c} \right)^2 \right]^{-3\beta+1/2}, \quad (1.5)$$

where  $b$  is the projected radius from the center of the cluster. Figure 1.3 shows the surface brightness distribution of the massive cluster Abell 1795 fit to the beta model.

This gas density distribution can be integrated to arrive at an expression for the total gas mass of the cluster. Comparisons of the cluster gas masses obtained in this manner to the mass in galaxies shows that nearly 80% of the luminous matter in clusters is in the gas, and that the galaxies can be thought of as test particles in a gravitational potential formed by the dark matter distribution and the ICM gas.

### 1.3 Hydrostatic Equilibrium and the Cluster Total Mass Estimate

The sound crossing time in galaxy clusters is much shorter than the Hubble time, so the gas can be treated as a hydrostatic fluid (Sarazin 1988). For such a gas, the equation

$$\nabla P_{\text{gas}} = -\rho_g \nabla \phi \quad (1.6)$$

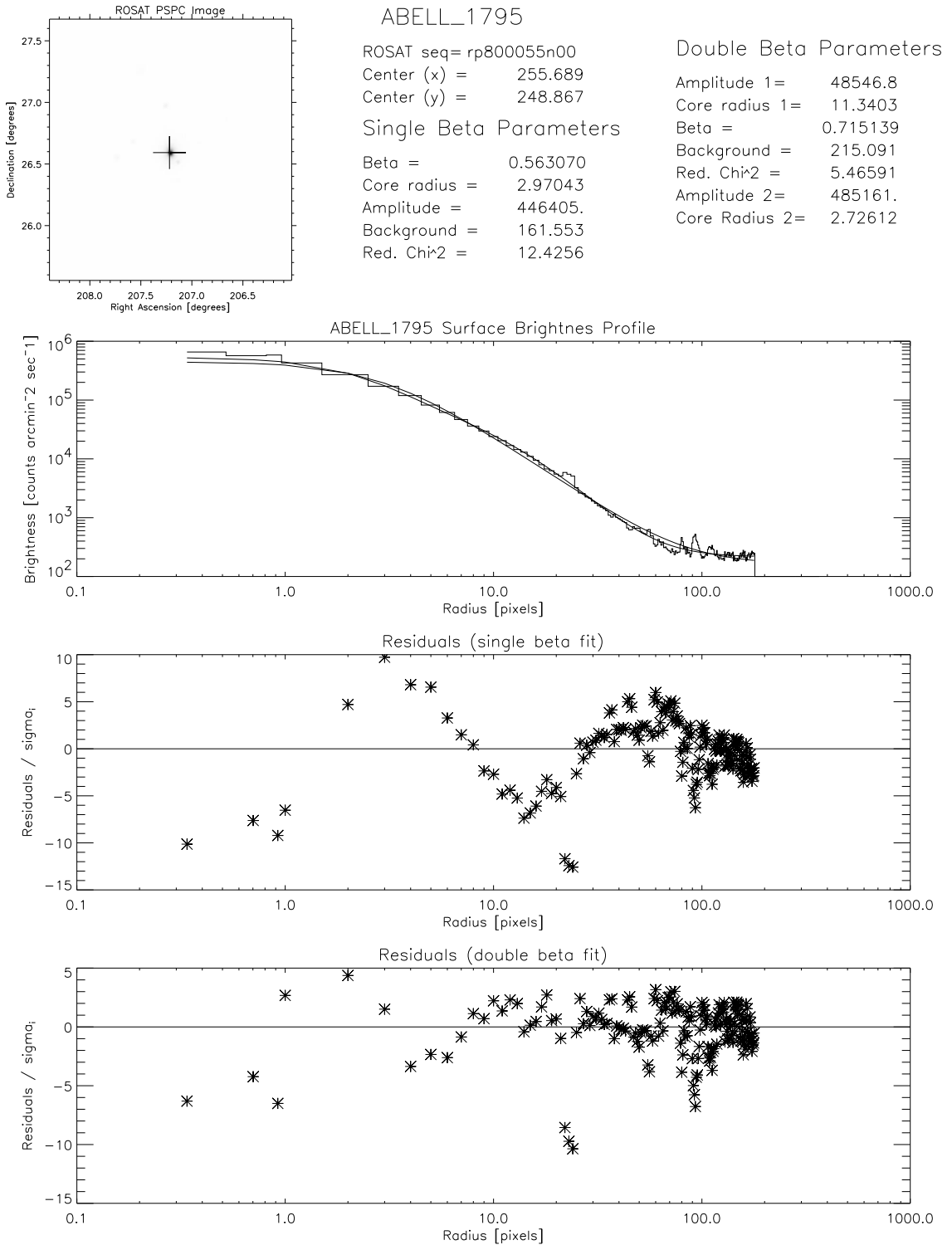


Figure 1.3: The surface brightness distribution of the cluster Abell 1795 from *ROSAT*.

can be used to describe the spatial structure of the gas. Observations show that the assumption of a spherical symmetry can apply, and the above equation can be written as

$$\frac{1}{\rho_g} \frac{dP}{dr} = -\frac{d\phi}{dr} = -\frac{GM(r)}{r^2}, \quad (1.7)$$

where  $\phi$  is the gravitational potential and  $M(r)$  is the mass interior to a radius  $r$ . The low density ( $\sim 10^{-3} \text{ cm}^{-3}$ ) of the gas means that the perfect gas law applies, and we can safely assume that  $P = \rho_g \mu m_p kT$ , where  $T$  is the gas temperature,  $\rho_g$  is the gas number density,  $m_p$  is the proton mass, and  $\mu \sim 0.6$  is the mean molecular weight of the gas. The spherical hydrostatic equation can now be written as

$$M(< r) = -\frac{kT}{G\mu m_p} r \left[ \frac{d \log T(r)}{d \log r} + \frac{d \log \rho_g(r)}{d \log r} \right], \quad (1.8)$$

which gives the total mass (gas + dark matter) as a function of the gas temperature and density. The simplest temperature distribution  $T(r)$  is an isothermal one, and is also backed by recent *XMM-Newton* observations (Pratt & Arnaud 2003).

## 1.4 Scaling Relations

Because the gas in the cluster potential is in hydrostatic and thermal equilibrium, its large scale properties can be related using simple theoretical arguments. For example, a simple relation between the cluster mass and temperature can be derived,

$$E \sim kT \quad \text{and} \quad E \sim \frac{GM}{r} \quad \text{and} \quad M \propto \frac{1}{r^3}, \quad (1.9)$$

which lead to

$$T \sim M^{2/3} \quad \text{or} \quad M \sim T^{3/2}. \quad (1.10)$$

The same can be done to derive the cluster luminosity as a function of temperature, with the result that

$$L \sim T^2. \quad (1.11)$$

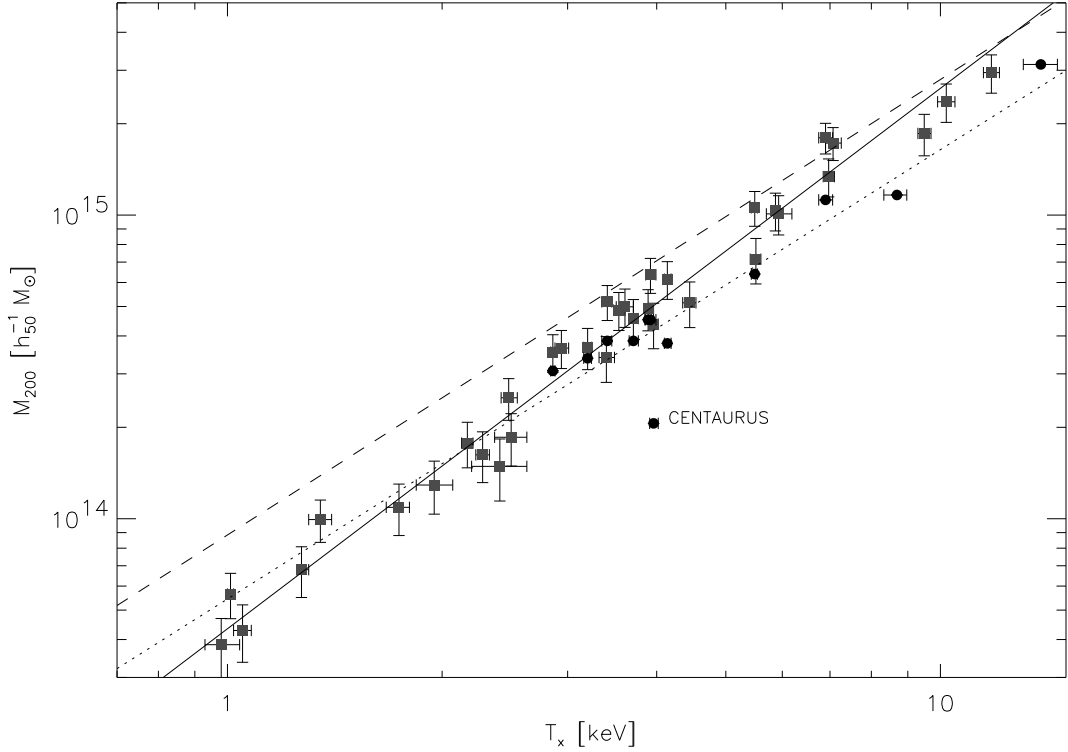


Figure 1.4: The observed cluster mass versus temperature relation from *ASCA*.

However, recent observations of a very large sample of galaxy clusters observed by *ASCA* (Horner 2001) and others have shown that the actual cluster scaling relations do not follow the theoretically expected ones. Figure 1.4 shows how the observed cluster mass depends on its measured temperature. The observed slope of the  $M$  versus  $T$  relation is 1.7, and not the expected  $3/2$ . Similarly, Figure 1.5 shows that the luminosity versus temperature relation also does not follow the theoretical expectation, and that the slope is steeper—closer to  $L \sim T^3$  than  $T^2$ . The  $L$ – $T$  discrepancy arises because the low temperature clusters and groups are underluminous, which steepens the overall slope. These underluminous clusters are probably the result of extra energy injected into their ICM. This extra energy “puffs up” the gas in the ICM, lowering its density and thereby decreasing its luminosity. The extra energy could be the result of preheating of the gas before cluster formation

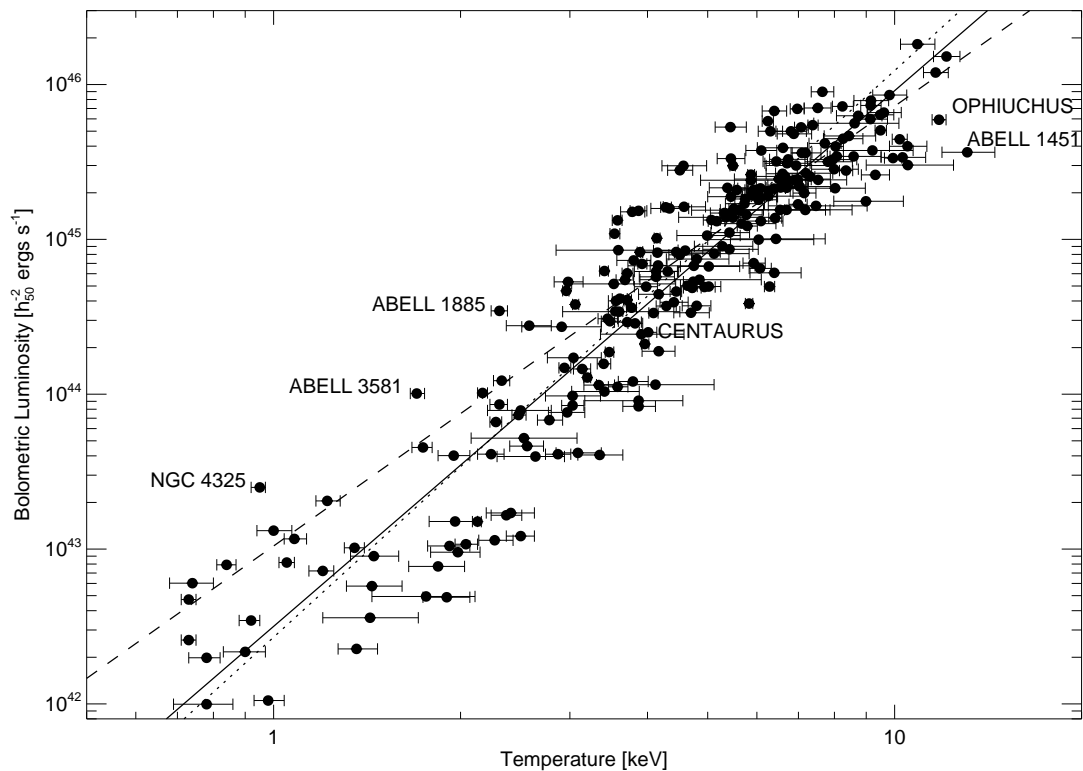


Figure 1.5: The observed cluster luminosity versus temperature relation from *ASCA*.

or energy injected afterwards from sources like the jets of AGN and large radio galaxies in the centers of clusters. The reason behind the discrepancy in the cluster scaling relations is currently an ongoing topic of research, and is being studied by new observations such as those of cluster entropy profiles (Ponman, Sanderson, & Finoguenov 2003).

## 1.5 Cooling Flows

Observations of massive, relaxed galaxy clusters show that they often have a very large peak in the X-ray emission in the center of the cluster much above that expected for emission that follows the canonical beta model (equation 1.5). The enhanced emission arises from an area of high density in the cluster center (since

emission goes as  $\rho^2$ ). High density regions cool more quickly, allowing the gas in the center to contract and enabling gas farther out to stream towards the center, hence the name “cooling flow.” The cooling times for the centers of these clusters ( $t_{cool} \propto \rho^{-1} T^{1/2}$ ) are less than the Hubble time, supporting this interpretation for the enhanced emission. However, evidence for the cool gas has proved elusive; *XMM-Newton* observations of cluster centers by Peterson et al. (2003) have shown that the gas has not cooled nearly as much as the standard cooling flow models predict. Also, evidence for any increased star formation that might be expected from a large reservoir of cool gas has so far not been found at the levels needed to match the X-ray derived mass deposition rates.

The presence of cool gas in the centers of cooling flow clusters sometimes makes spectral fits to one temperature models troublesome. This is more often the case for fits to regions that are extracted from the centers of clusters. All of the cluster data in this thesis are extracted from regions encompassing as much as possible of the cluster emission; since most of the cluster gas is in the outer regions the possible presence of cooling flows does not greatly influence spectral fits to these data.

## 1.6 X-ray Spectra of Galaxy Clusters

The bolometric luminosity of galaxy clusters derived from X-ray measurements ranges from  $10^{43}$ – $10^{46}$  ergs s<sup>-1</sup>. The stellar luminosity of clusters is  $10^{12}$ –( $2 \times 10^{13}$ )  $L_{\odot}$ .

The main component of the X-ray spectra of galaxy clusters is thermal bremsstrahlung. This free-free emission is the result of the large mass of hot gas in the cluster potential in thermal equilibrium and interacting with itself. Since bremsstrahlung results from interaction between charged particles, the emissivity is proportional to the

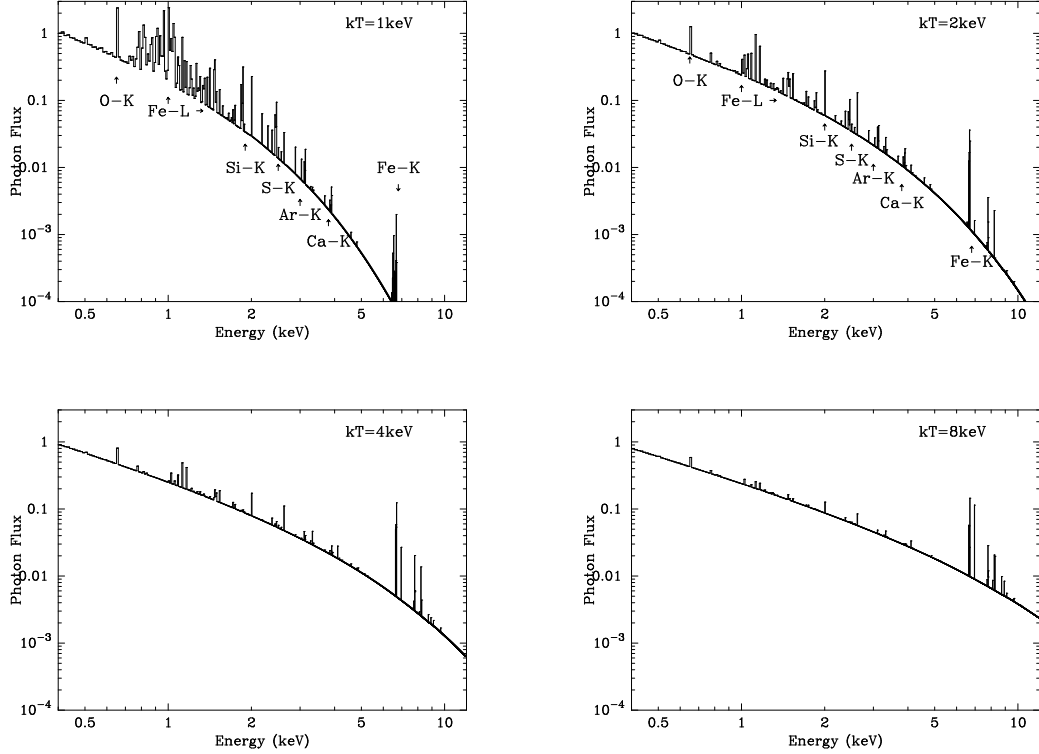


Figure 1.6: Model spectra of X-ray emitting hot gas at four different temperatures. The shape of the underlying bremsstrahlung continuum extends out to higher energies as the temperature increases while the equivalent width of the spectral lines goes down.

square of the electron density (Rybicki & Lightman 1979),

$$\epsilon = 6.8 \times 10^{-38} Z^2 n_e n_i T^{-1/2} e^{-h\nu/kT} g_{ff}, \quad (1.12)$$

where  $n_e$  and  $n_i$  are the electron and ion density (we can assume  $n_e \approx n_i$ ),  $T$  is the gas temperature,  $Z$  is the ionic charge, and  $g_{ff}$  is the free-free Gaunt factor that incorporates quantum effects. The optical depth of the gas to Compton scattering and photoelectric absorption is much less than one, so we can safely ignore the effects of radiative transfer with the assumption that the gas is optically thin.

In addition to this continuum emission is the line emission from metals in the ICM. Figure 1.6 shows some model spectra for four different gas temperatures of an ICM with a metal abundance of 0.3 solar. The most predominant spectral lines

are the those from transitions between low lying energy levels from the K-shells of the abundant elements in the ICM. Lines from the elements oxygen through nickel have their K-shell lines in the X-ray spectrum lying between 0.5–10 keV. The energy of these lines can be simply approximated with the Bohr formula for H-like ionized atoms,

$$E_n = 13.6 \text{ eV} \left( \frac{Z^2}{n^2} \right), \quad (1.13)$$

which leads to an energy for the K-shell lines ( $n \rightarrow 1$ ) of

$$E_K(Z) = \left( \frac{3}{4} \right) Z^2 13.6 \text{ eV}, \quad (1.14)$$

where  $Z$  is the atomic number of the element. Lines from the L-shell ( $n \rightarrow 2$ ) are also present in spectra of the ICM from higher  $Z$  elements like iron and nickel. However, these lines are generally not as strong as the K-shell lines in clusters, and are only important in lower temperature clusters where the ionization balance is such that lower ionization states are populated.

The equivalent width of the spectral lines is a strong function of temperature. This can be seen in Figure 1.6 where the higher temperature plasmas are too severely ionized to allow many lines. The other important factor determining the equivalent width is of course the element's natural abundance, a subject taken up in more detail in later chapters. In the X-ray band, some abundant elements with observable line emission are oxygen, neon, magnesium, silicon, sulfur, iron and nickel.

## 1.7 Chemical Evolution and Elemental Abundances

Chemical evolution in the astronomical sense means the history of metal enrichment of a system. This requires a knowledge of how the elements are formed and how they arrive in the different astronomical systems.

The primordial elements produced in the Big Bang are mainly limited to the light elements up to lithium. Heavier elements are produced in the interiors of stars as a byproduct of stellar fusion reactions, and in the explosive nucleosynthesis that occurs in supernovae. The intermediate elements up to iron can be produced during the normal lifetime of the star, while the heaviest elements are produced by mechanisms such as the  $s$ ,  $r$ , and neutrino processes during the actual supernova explosion.

The relative abundances of the different elements produced in supernovae depends strongly on the type of progenitor star present before the supernova explosion.

### 1.7.1 Supernovae

The many different types of supernovae can be broadly classified into two different categories, Type I and Type II. Originally, this classification was based on the detection of hydrogen lines in the optical spectra, with Type Is not showing hydrogen lines while Type IIs do.

A more useful classification is one based on the physics of the underlying supernovae and the mass of the progenitor star. Type IIs (SN II) have as their progenitors massive stars of several solar masses. When they reach the end of their normal lifetimes, they undergo core collapse and then explode as supernovae. Supernovae of Type Ia (SN Ia) have a different formation mechanism; they are believed to have as their progenitors white dwarfs that are members of a binary pair. As the white dwarf accretes material from its companion star it can exceed the Chandrasekhar mass limit and initiate explosive burning and a supernovae.

Other classes of supernovae exist (eg., Ib, Ic, IIn, IIp, etc.), mainly based on differences in the optical spectra. They can all be broken down into the two main classes of core collapse supernovae (SN II) formed from massive, short-lived stars;

and mass accretion supernovae (SN Ia), formed from less massive, longer-lived stars that have left the main sequence and become white dwarfs. This thesis will only discuss SN Ia and SN II, and ignore the subtypes.

## **Supernovae Models and Yields**

The important practical differences between the two supernovae types lie in the yields of the elements produced by the supernovae. Because the progenitors of SN II have progressed farther down the nuclear burning chain, they have a core containing intermediate elements such as carbon, silicon, etc. The progenitors of SN Ia are less massive and not able to synthesize these elements during normal nuclear burning, and are composed of mainly hydrogen, helium, and carbon.

The presence of a different combination of elements before the supernova explains some of the difference in the final yields of the two different types of supernovae. The other main difference has to do with the energetics of the explosion, and the detailed physics of the explosions themselves. This is usually investigated by computer modeling. However, the yields for these models depend sensitively on hard to compute reaction rates, and upon the implementation of the computer code. The yields from these models are often normalized to produce the abundance results expected for the solar neighborhood (see § 3.1.2 & § 4.3) and so must be kept up to date with the latest abundance measurements. The uncertainties in the yields for individual elements can be up to about a factor of two (see § 4.8.1).

The yields for two models representative of the two classes are presented in Figure 1.7. The SN II produce more of the alpha-elements than do the SN Ia, while the SN Ia dominate the production of elements in the iron peak.

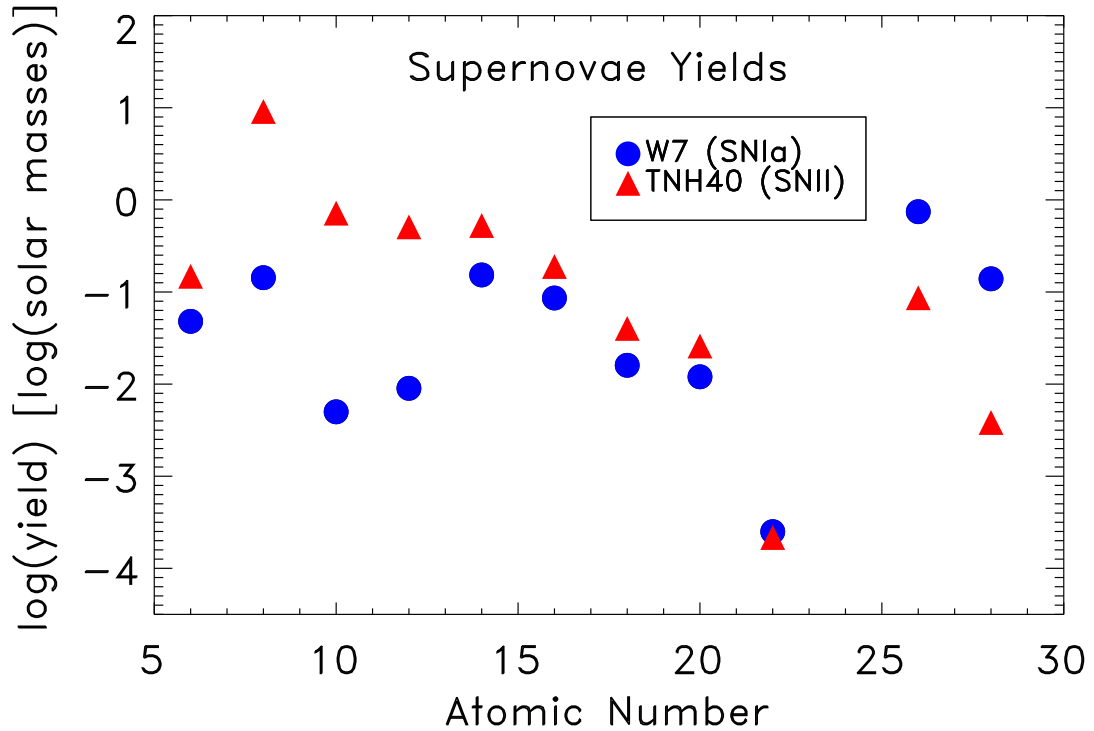


Figure 1.7: Supernovae yields. The yield for each element is given in solar masses per supernova. SN II produce more of the alpha-elements, especially oxygen, while SN Ia produce more of the elements in the iron peak.

### 1.7.2 Metal Transport Mechanisms

There are several suggested mechanisms for transporting metals from the immediate stellar neighborhoods and the galactic ISM into the cluster ICM. Two of the most likely include winds produced by the energetic explosions of the supernovae themselves, and ram pressure stripping.

Ram pressure stripping occurs when a galaxy travels through the dense material of the cluster ICM and has gas ablated from its outer layers into the ICM. The detailed mechanisms of supernovae winds are not well known, but significant evidence for winds is often found in observations of star forming galaxies. Galaxies like M82 show streamers of material flowing from their cores, and spectroscopic velocities of

the gas that often exceed the binding potential of the galaxy.

Evidence for the transport of metals away from supernovae can be found in X-ray observations of SN remnants. Areas of the remnant are often found highly enriched in metals produced in the explosion. Some evidence is seen for presence of concentric layers of different elements, although other evidence is found that shows that mixing is often present as the SN wind encounters the ISM. Constraining the yields of SN models by X-ray observations of their remnants is difficult because of the complex physics involved in the explosion, winds, shocks, and the differing composition of the ISM.

# Bibliography

- Abell, G. O. 1958, *ApJS*, 3, 211
- Cavaliere, A. & Fusco-Femiano, R. 1976, *A&A*, 49, 137
- Horner, D. 2001, Ph.D. Dissertation, Department of Astronomy, University of Maryland College Park
- King, I. 1962, *AJ*, 67, 471
- Mitchell, R. J., Culhane, J. L., Davison, P. J. N., & Ives, J. C. 1976, *MNRAS*, 175, 29P
- Navarro, J. F., Frenk, C. S., & White, S. D. M. 1997, *ApJ*, 490, 493
- Peterson, J. R., Kahn, S. M., Paerels, F. B. S., Kaastra, J. S., Tamura, T., Bleeker, J. A. M., Ferrigno, C., & Jernigan, J. G. 2003, *ApJ*, 590, 207
- Ponman, T. J., Sanderson, A. J. R., & Finoguenov, A. 2003, *MNRAS*, 343, 331
- Pratt, G. W. & Arnaud, M. 2003, *A&A*, 408, 1
- Rybicki, G. B. & Lightman, A. P. 1979, New York, Wiley-Interscience, 1979. 393 p.160
- Sarazin, C. L. 1988, Cambridge Astrophysics Series, Cambridge: Cambridge University Press, 1988
- Serlemitsos, P. J., Smith, B. W., Boldt, E. A., Holt, S. S., & Swank, J. H. 1977, *ApJ*, 211, L63
- Zwicky, F. 1937, *ApJ*, 86, 217

# Chapter 2

## Satellites, Instruments, and Data Reduction

“Pretty pictures are great, but the real science is done with spectroscopy.”

*Anonymous Astronomer*

### 2.1 *ASCA*

The *ASCA* satellite (*Advanced Satellite for Cosmology and Astrophysics*) was a Japanese X-ray telescope launched in 1993 (Tanaka, Inoue, & Holt 1994). *ASCA* (see Fig. 2.1) had four X-ray mirrors coaligned with four detectors sensitive in the 0.5–10 keV energy range. *ASCA* was a great improvement over the previous dominant X-ray satellite *ROSAT* in that it had a factor of three larger effective area (see Fig. 2.2) that allowed for much greater sensitivity, had a high energy bandpass that extended above *ROSAT*'s limit of 2.5 keV all the way to 10 keV, and had improved CCD-level spectral resolution. This enabled observations of much harder and fainter sources and allowed observations of many important metal lines. The improvement in collecting area and spectral bandpass came from the use of

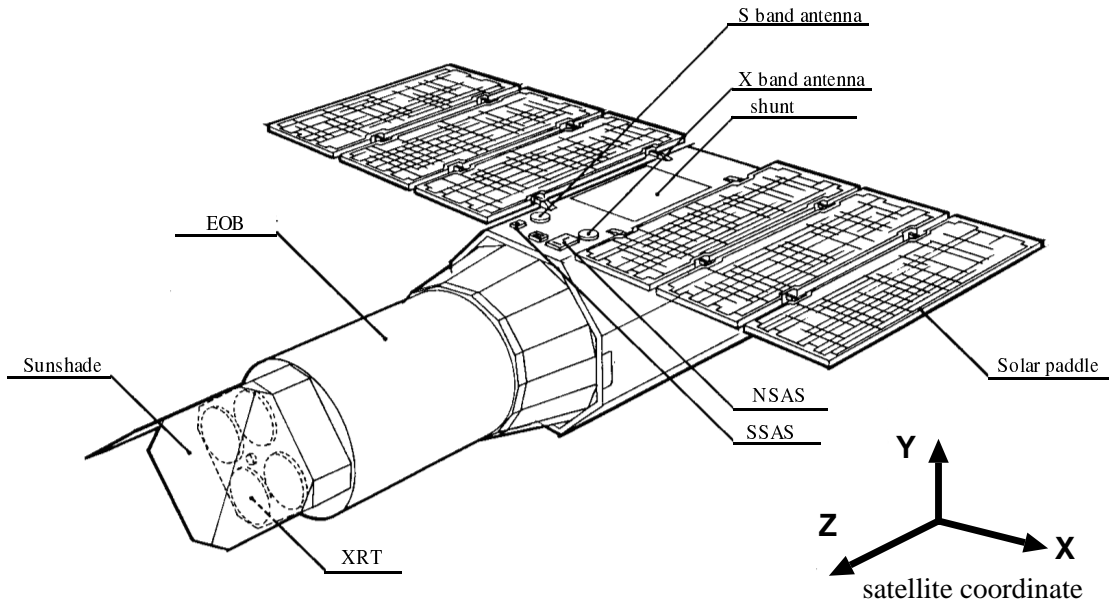


Figure 2.1: The *ASCA* X-ray telescope.

lightweight foil nested optics compared to the precise machined figure of *ROSAT*'s more massive mirrors. *ASCA*'s spatial resolution of 3 arcminutes (HPD) did not equal *ROSAT*'s PSF (25 arcseconds), but with the publication of the *ROSAT* All Sky Survey and the use of data from both missions, *ASCA*'s spectroscopic power very neatly complemented *ROSAT*'s spatial imaging strengths.

### 2.1.1 The X-ray Mirrors

The reflectivity of most materials is low at X-ray energies. In order to achieve high reflectivity, grazing incidences must be used. However, the reflective area of a mirror is much decreased by utilizing it at a grazing angle. X-ray astronomers have accommodated these necessities by building nested shell grazing incidence mirrors based on the Wolter I design shown in Figure 2.3. The *ASCA* mirror (see Figure 2.4) implemented this design by using a large number (120) of very thin shells that were a close approximation to the precise Wolter I figure. This tradeoff resulted in increased

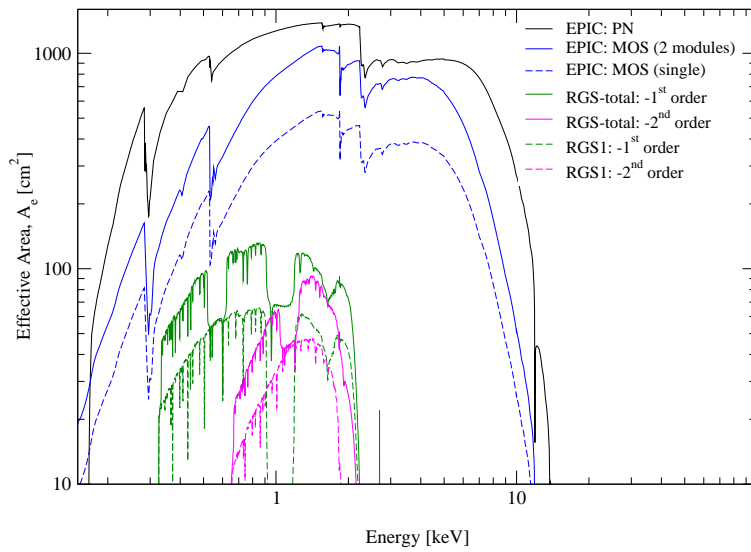
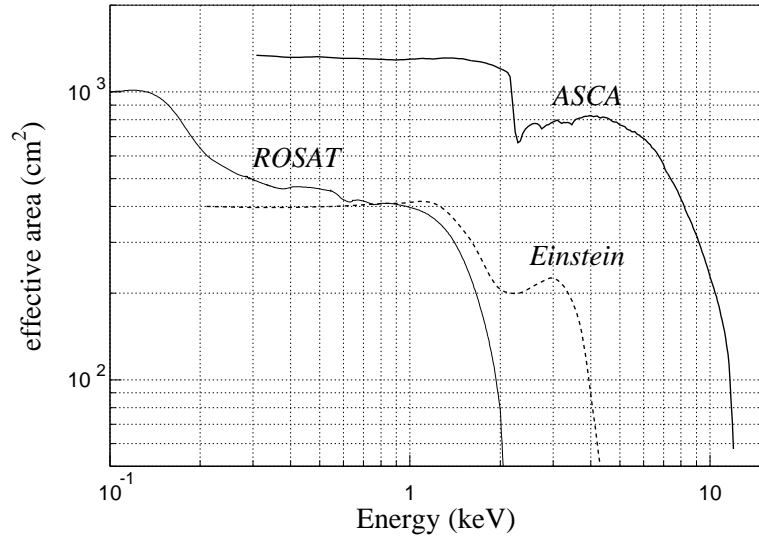


Figure 2.2: The effective areas of *ASCA*, *ROSAT*, and *XMM-Newton*.

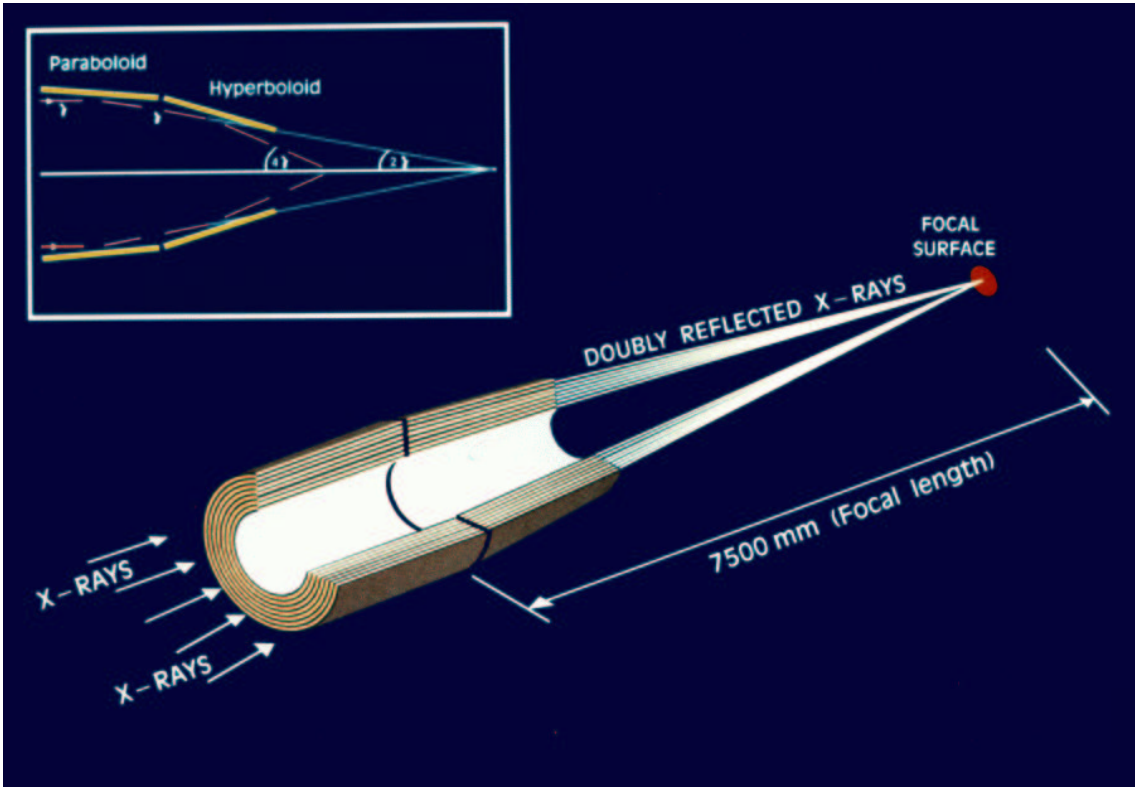


Figure 2.3: Nested shell grazing incidence mirror design utilizing Wolter I optics in the *XMM-Newton* mirror.

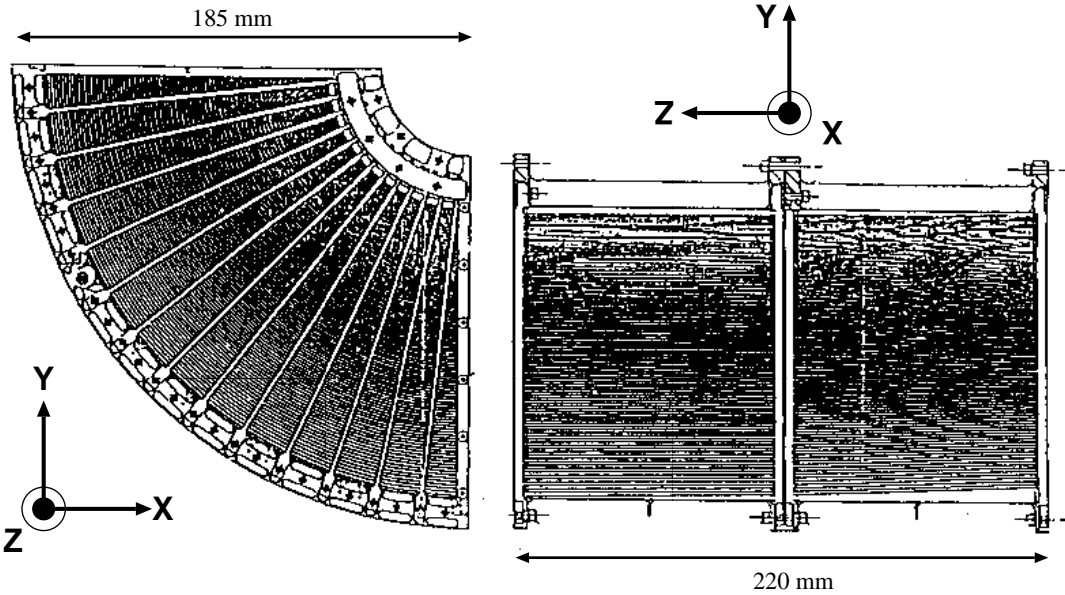


Figure 2.4: The *ASCA* mirror. One quadrant of the mirror is shown on the left. The 120 foils can be seen end on as well as the radial alignment bars.

effective area because of the very close packed thin shells, but a degradation of the PSF compared to the finely figured *ROSAT* design. The on-axis effective area of the *ASCA* mirrors is high, but because of the close spacing, vignetting becomes a problem for large off-axis angles. This reduces the effective areas at these angles, and causes the *ASCA* PSF to be somewhat dependent upon off-axis angle.

The *XMM-Newton* mirror was built along more traditional lines. Instead of very many thin shells the *XMM-Newton* mirror utilized a fewer number of highly polished metal cylinders. This implementation results in a better figure for the mirrors and an improved PSF. A large effective area is produced by using larger diameter mirrors and more mirror modules than *ASCA*.

### **2.1.2 The GIS Detector**

The Gas Imaging Spectrometer (GIS) is one of the two types of X-ray detector on *ASCA*. The GIS consists of a gas cell coupled to a position sensitive phototube (see Fig. 2.5). X-ray photons enter through the beryllium entrance window of the GIS into the xenon filled gas cell. There they interact with the gas through the photoelectric effect and generate a cloud of charge around the interaction site. The charge cloud is then accelerated across 5300 Volts until it interacts with the xenon and emits UV photons. These UV photons then enter the position-sensitive phototube through a quartz window, where they interact with a sensitive bialkali photocathode that converts the UV photons into photoelectrons which are then amplified down the electronics chain of the phototube. The resultant output of the phototube is analyzed to determine the interaction position by looking at the signal distribution on the tube anodes, and the energy of the initial interaction by measuring the strength of the resultant UV flux.

The field of view of the GIS is circular and is about 3/4 of a degree across. The

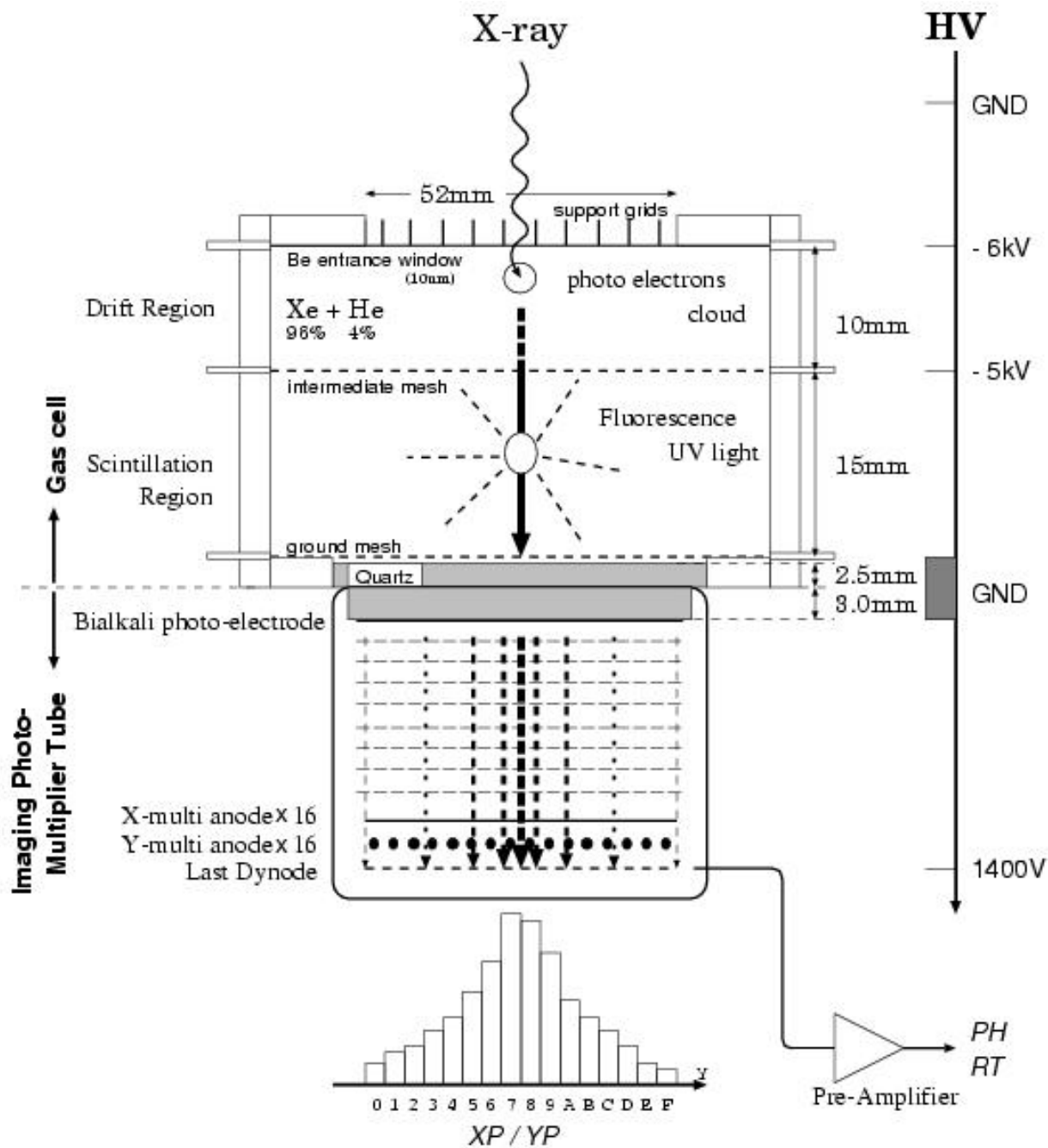


Figure 2.5: Diagram of the ASCA GIS detector.

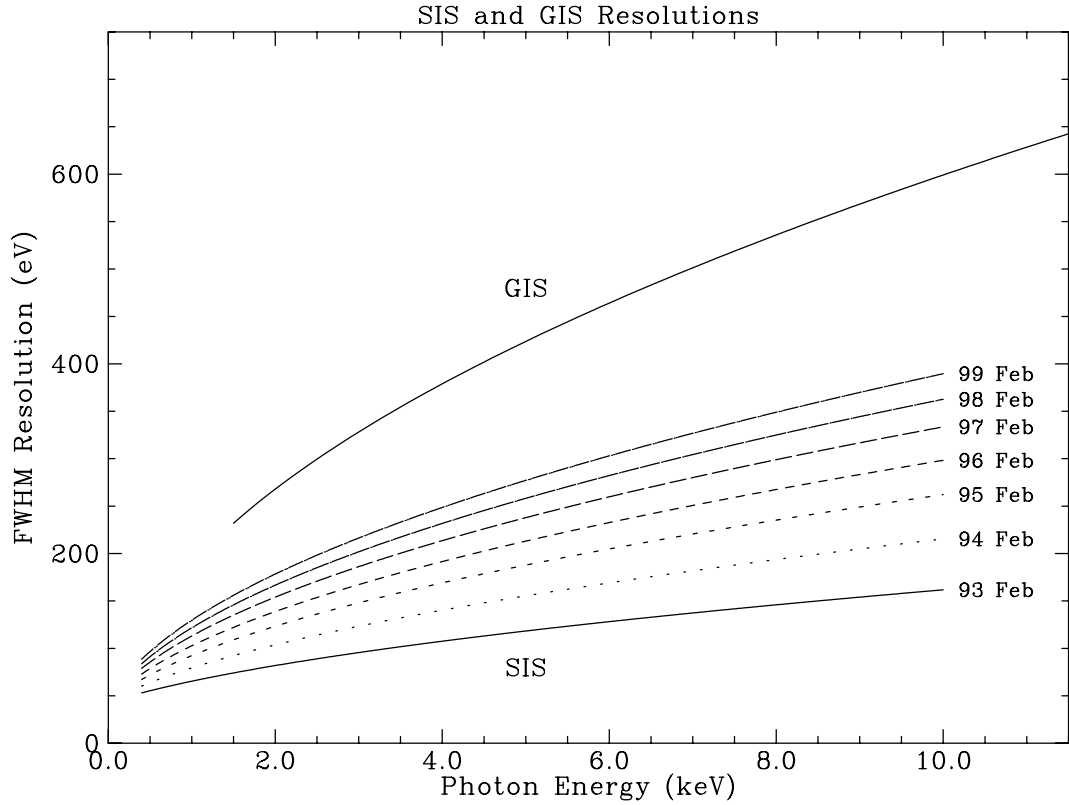


Figure 2.6: Energy resolution of the *ASCA* GIS and SIS detectors.

energy resolution of the GIS is dependent on counting statistics, and is accurate to several percent (see Figure 2.6). The spatial resolution of the GIS is determined by the size of the scintillation photon distribution, which is significant compared to the PSF of the X-ray mirror. For this reason the GIS PSF is broader than the SIS PSF.

One of the major goals of the GIS design was to reduce the non-X-ray background, and the GIS software employs risetime, pulse height, and spatial distribution filtering to discriminate between X-rays and background particles.

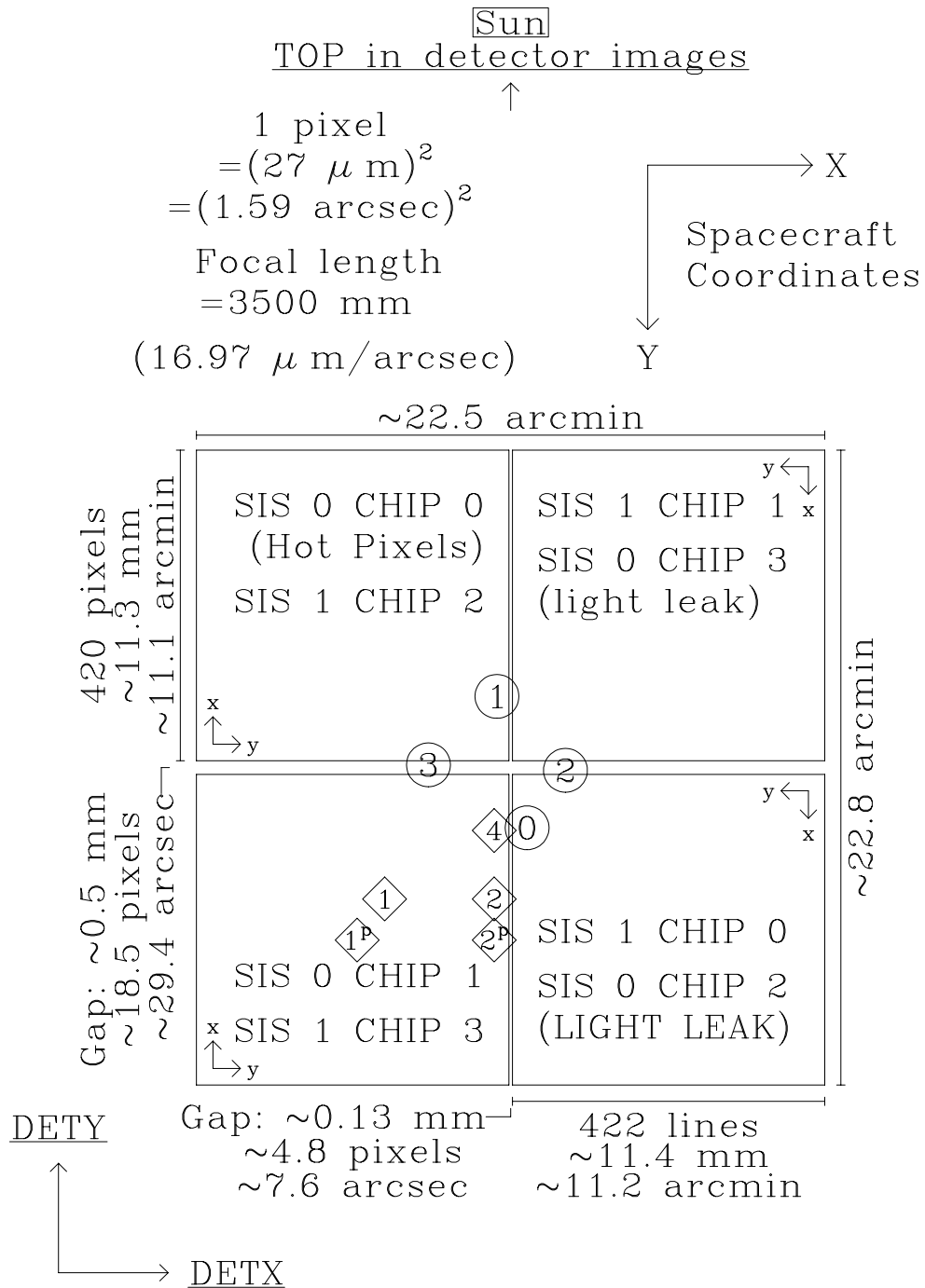
### 2.1.3 The SIS Detector

The SIS (*Solid-state Imaging Spectrometer*) detector is at the focus of the other two of *ASCA*'s four mirrors. Each SIS consists of 4 silicon CCD chips arranged in a square array. Each chip has a  $422 \times 420$  array of  $27 \mu\text{m}$  pixels and is 11 mm on a side. The total array of four chips has a field of view of about 22 arcminutes on a side and is shown diagrammatically in Figure 2.7.

The CCD detector (*Charge Coupled Device*) is a solid state device fabricated on a wafer of silicon. Its operation is similar to that of an optical CCD, although at X-ray energies astrophysical photons are capable of inducing enough charge in the detector to permit the counting of individual events. A portion of the thickness of the silicon wafer under each pixel is used as the detection region and is kept depleted of free charge carriers by the application of an electric field between an electrode on the back of the CCD and electrodes associated with the pixel circuit on the front. Above the depletion region a  $\text{SiO}_2$  insulating layer is applied to the wafer, and the CCD electronics for each pixel are laid down above this insulating layer.

An incoming X-ray photon can interact in the depletion layer via the photoelectric effect and generate a charge cloud of electrons and holes. The charges are kept in the pixel potential well by the application of appropriate voltages on the pixel electrodes. When the integration time of the sensor is completed, the charges are passed along pixel by pixel towards a readout node on the CCD by modulating the voltages on the electrodes and are then sequentially readout through the preamplifier. The charge in each pixel is converted to a digital signal proportional to the energy of the initial incoming X-ray photon.

The SIS is typically operated with integration times such that each incoming photon is readout and its energy determined before another photon can impinge on



NOTE: Diamonds show estimated default positions for point sources in 1, 2 and 4 CCD modes ( $1^P$  and  $2^P$  are old defaults). Circles show estimated optical axes of the 4 telescopes. Chip boundaries are shown for SIS-0; SIS-1 is displaced ~1 mm to negative DETY.

Figure 2.7: Diagram of the chip placement in the ASCA SIS detector.

the same pixel. For observations of diffuse sources like galaxy clusters, photon pile-up is almost never a problem, but does need to be taken into account for observations of bright galactic point sources like the Crab and Cyg X-1.

Each event is labeled with the time, pixel location, the pulse height (energy), and a grade that indicates which (if any) neighboring pixels also accumulated charge during the same integration time. Downstream processing later filters on the grade in order to separate out background events and to choose events of a particular quality. The energy resolution of single pixel photon events is better than adding the signal from neighboring pixels because the uncertainty associated with the energy determination increases as more pixels are added together. However, if high quality spectroscopy is not needed or desired, multiple pixel events can be used in order to increase the number of detected photons and the sensitivity of the instrument. Observations in this thesis generally use only single or double pixel events.

The energy resolution of the SIS detector is significantly better than that of the GIS (see Figure 2.6). The SIS has an energy resolution of about 150 eV at 2 keV, while the GIS has an energy resolution of only about 250 eV at this energy.

Unfortunately, the SIS detector increasingly suffered from a low energy efficiency problem throughout its lifetime. The effective area below 1 keV has continually degraded since launch. It is thought that this problem is the result of a buildup of contamination on the SIS detector or the degradation of the charge transfer efficiency. This problem is generally dealt with by allowing the galactic hydrogen absorption component of the spectral model to vary freely in the fitting process.

## 2.2 *XMM-Newton*

The *XMM-Newton* X-ray telescope is in the next generation of X-ray telescopes after *ASCA* and *ROSAT*. *XMM-Newton* was launched in December 1999 by the European Space Agency and is currently still operating in 2004. Whereas the American telescope *Chandra* can be seen as a successor to *ROSAT* because of its superb spatial resolution (less than one arcsecond), *XMM-Newton* follows in the footsteps of *ASCA* by utilizing a very large effective area that provides the sensitivity needed for high resolution spectroscopy. For spectroscopic observations of large diffuse objects like galaxy clusters, high spatial resolution is generally not needed.

*XMM-Newton* consists of three X-ray mirrors, three different types of X-ray detectors, and a UV/optical telescope with its own mirror and detector. All of the instruments are coaligned and can take data simultaneously, as shown in Figure 2.8. The three types of X-ray detector are the EPIC (European Photon Imaging Camera) pn, the EPIC MOS, and the RGS. The EPIC cameras are CCD detectors, while the RGS is a reflecting grating spectrometer which focuses onto a set of CCD detectors not in the focal plane of the X-ray mirrors. Two of the X-ray mirrors are equipped with both a MOS camera and an RGS grating array; the RGS diverts about 40% of the incoming flux from the mirror onto the gratings, while another 44% goes towards the MOS camera. The third X-ray mirror is focused solely onto the pn camera which receives all of the incoming light from its mirror. Thus, the two MOS cameras together receive 88/300 of the X-ray flux received by *XMM-Newton*, while the pn camera receives 100/300, over twice as much as each MOS camera alone. Together the EPIC cameras see 188/300 of the X-ray flux received by *XMM-Newton*.

The data in chapter 3 of this thesis is taken solely with the EPIC cameras. While the RGS gratings could provide useful information as a result of their better energy

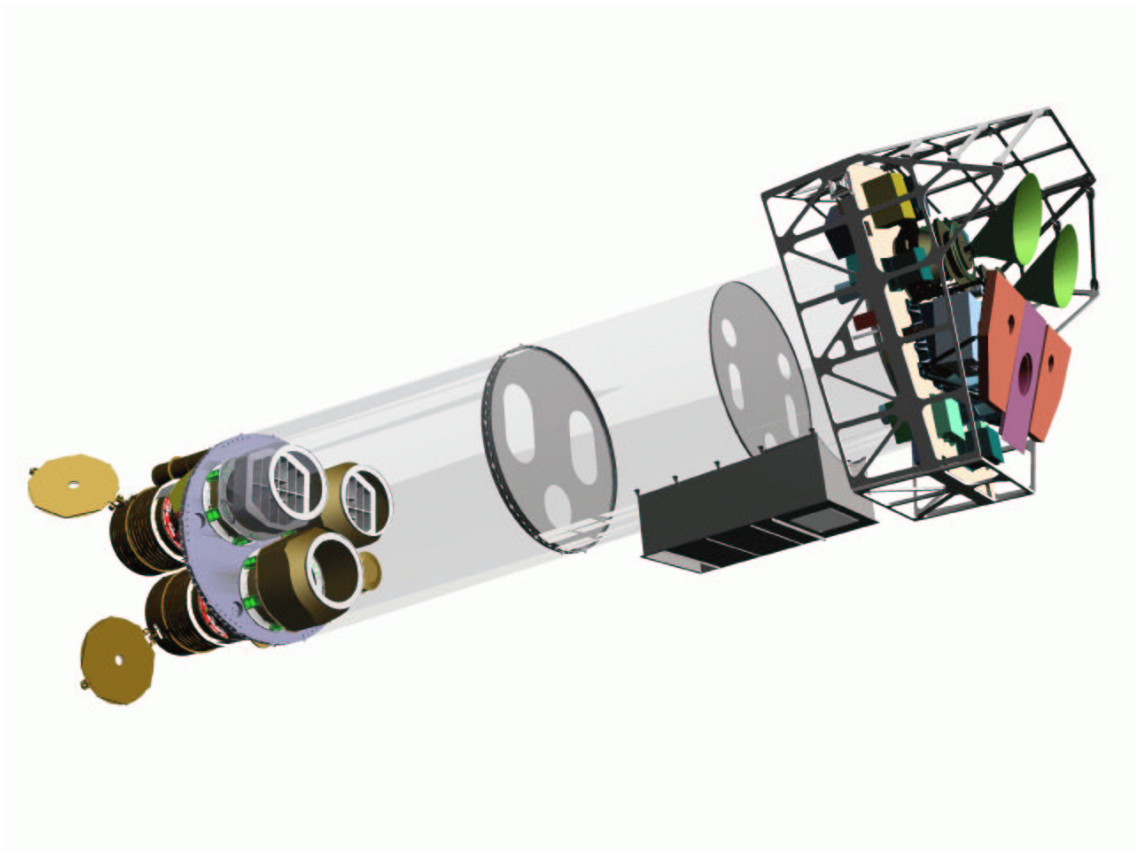


Figure 2.8: The *XMM-Newton* X-ray telescope.

resolution compared to the EPIC cameras, the flux from diffuse objects such as galaxy clusters is more difficult to analyze because the RGS is sensitive to a much smaller area of the *XMM-Newton* field of view, and because the diffuse nature of the emission degrades the inherent spectral resolution of the gratings. Also, the RGSs receive only 80/300 of the *XMM-Newton* X-ray flux, less than half the amount seen by the EPIC cameras.

### 2.2.1 The MOS Detector

The MOS (Metal Oxide Semiconductor) detector operates in a manner similar to the *ASCA* SIS detector, with the pixel electronics on the front side of the detector. Each of the two MOS cameras is an array of 7 square 600 by 600 pixel chips arranged

## Comparison of focal plane organisation of EPIC MOS and pn cameras

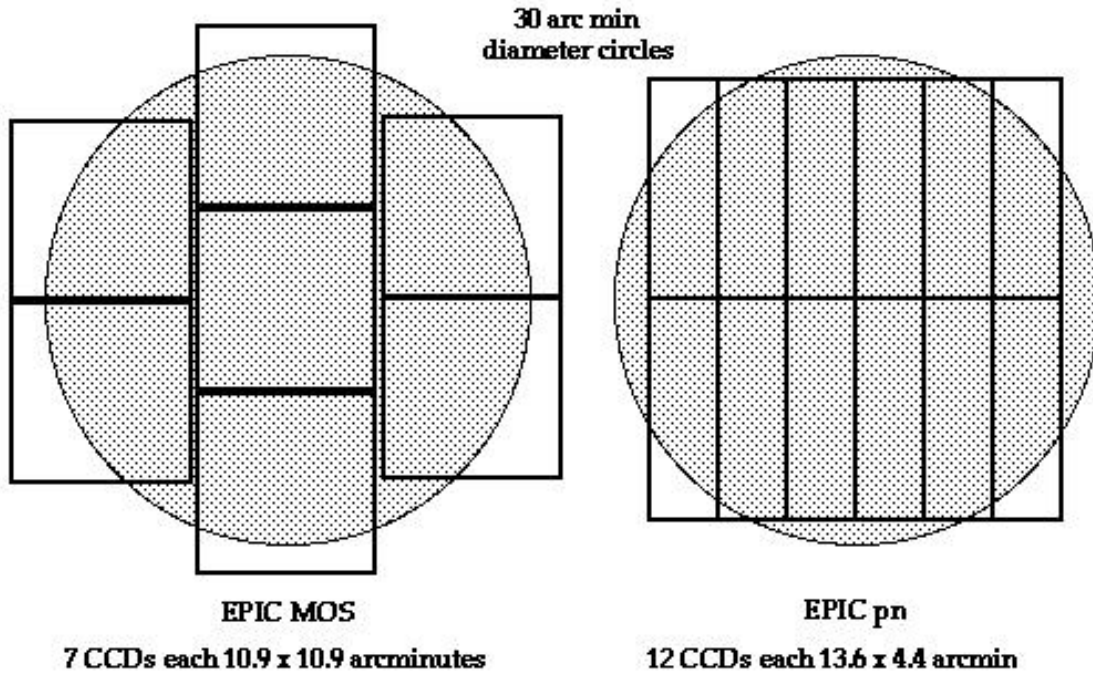


Figure 2.9: The field of view of the *XMM-Newton* EPIC cameras.

in a filled hexagon pattern as in Figure 2.9. The field of view of each MOS is about 30 arcminutes across and the spectral resolution at 1 keV is about 70 eV. Unfortunately, the MOS detectors have been prone to increasing charge transfer inefficiency (CTI) caused by background particles and cosmic rays deteriorating the performance of the CCD. This has resulted in a small but steady degrading of the MOS spectral resolution. However, a recent deep cooling of the EPIC cameras has significantly improved the CTI.

### 2.2.2 The pn Detector

The EPIC pn detector on *XMM-Newton* is named simply for the type of semiconductor junction that forms the heart of the CCD. However, the pn camera has a few important differences with respect to the MOS camera. The pn camera uses what are known as a backside illuminated chips, or one in which the pixel electronics are

behind the photon interaction region. The absence of extra circuitry in front of the detector leads to improvements in quantum efficiency, especially in the lower part of the *XMM-Newton* bandpass below 1 keV. Figure 2.10 shows that while the MOS CCDs have a quantum efficiency ranging from 0.2 to 0.5 below the oxygen edge at 0.5 keV, the pn CCDs have quantum efficiencies ranging from 0.8–0.9 in the same energy band. The quantum efficiency of the MOS detectors also falls at higher energies, resulting in a practical upper limit of about 10 keV, while the pn can observe usefully up to about 15 keV.

The pn detector also offers a faster sampling interval for those wishing to do timing studies. Also, the the improved quantum efficiency of the chip combined with the unimpeded view of the X-ray mirror (no RGS to siphon off some of the flux) means that the pn detector has a much higher effective area compared to the MOS detectors. Practically, this means that spectral fits made by jointly fitting data to all three EPIC detectors will be driven by the pn data, since its much greater effective area leads to smaller statistical error bars and thus a much higher weighting in the fit.

The field of view of the pn detector is identical to that of the MOS, but its spectral resolution of 80 eV at 1 keV is slightly worse than the MOS resolution of 70 eV at the same energy. However, the pn detector has not suffered from the effects of CTI that have plagued the MOS detectors because each column of the pn pixel array has its own readout node, much reducing the number of transfer steps required and the ill effects of CTI.

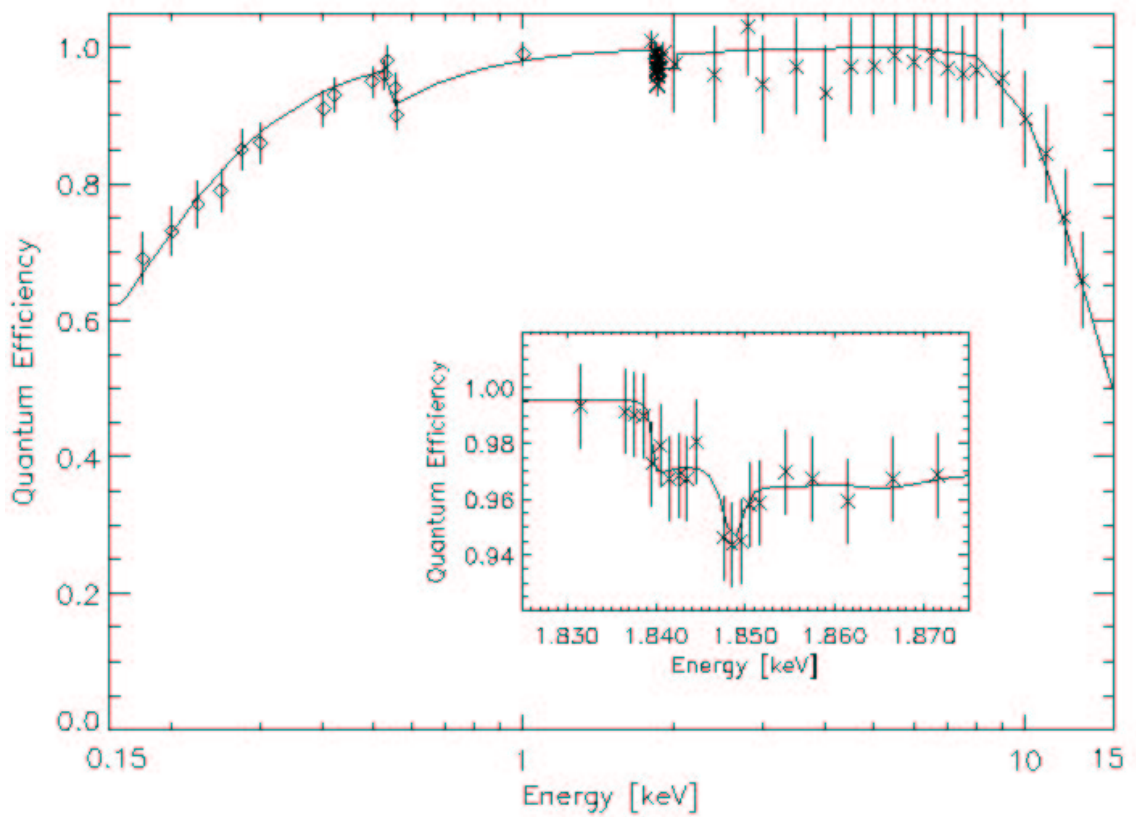
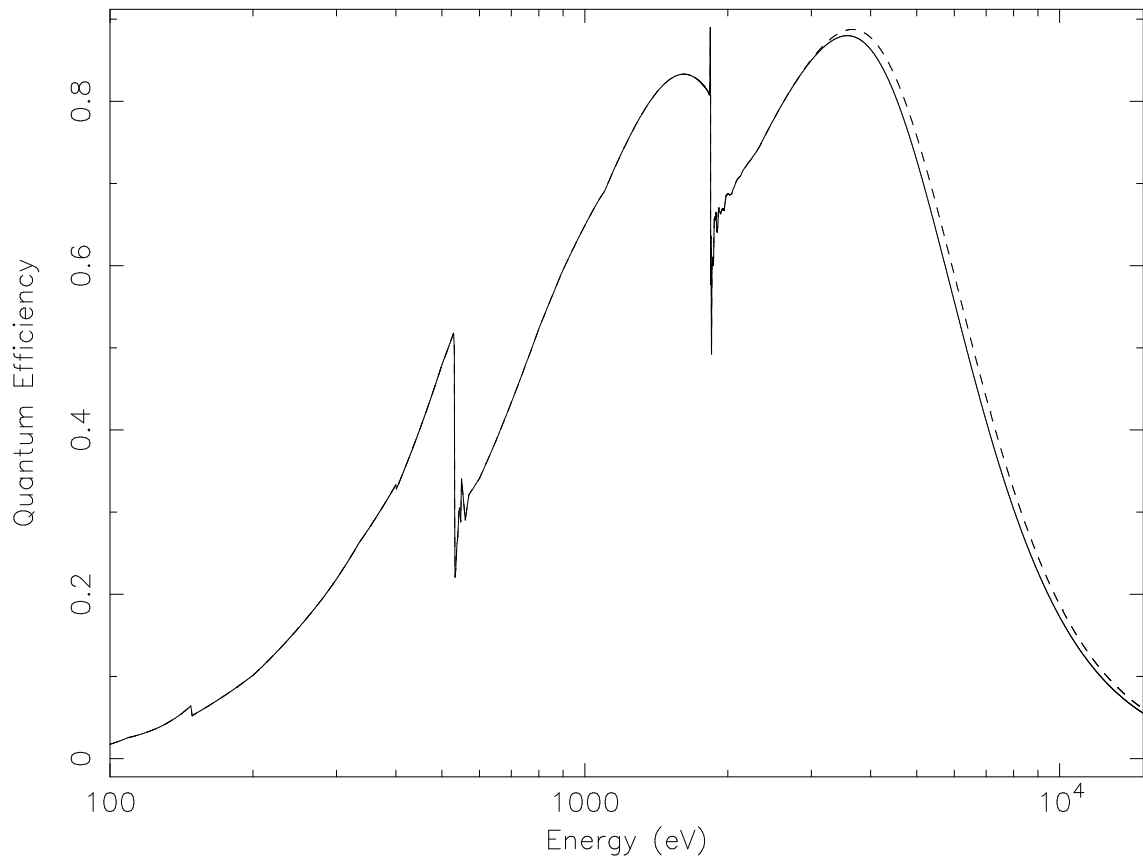


Figure 2.10: The quantum efficiencies of the *XMM-Newton* EPIC MOS and pn detectors.

## 2.3 Spectral Fitting

In order to make meaningful sense of the data, it must be fit to a spectral model so that we can test the validity of our assumptions about the source. Although we would like to measure the real spectrum of the source in the form of the source flux as a function of energy,  $F(E)$ , what is actually measured is the number of photons counted in each detector channel  $I$ , or  $C(I)$ . For typical detectors in X-ray astronomy, the number of spectral channels over the X-ray energy range can be from 128 to a few thousand<sup>1</sup>.

The difference between  $F(E)$  and  $C(I)$  is caused by the imperfect response of the telescope. The part contributed by the detector alone can be represented by  $R(E, I)$ , which can be thought of as a two dimensional matrix containing the channel space response of the detector to monoenergetic photons. The remaining portion of the telescope response can be represented by the function  $A(E)$ , called the effective area of the telescope. This portion of the telescope response contains contributions from things like the filter transmission function, the quantum efficiency of the detector, the window transmission, and the effective area of the X-ray mirror. The combination of the two responses act on the source spectrum to produce a photon count spectrum:

$$C(I) = \int_0^{\infty} F(E) R(E, I) A(E) dE.$$

The instrument is calibrated and the results are kept in the redistribution matrix file (RMF) and ancillary response file (ARF). The RMF contains the part of the response due to the detector alone,  $R(E, I)$ , and does not vary with position on the

---

<sup>1</sup>The *ASCA* GIS detector had relatively poor energy resolution and employed 256 channels across the 0.3–10.0 keV band. The *ASCA* SIS used 1024 channels for the same band, while the *XMM-Newton* MOS CCDs use 800, and the pn CCD 4096.

detector. The ARF contains the part of the response corresponding to  $A(E)$  and can vary with detector position because the effective area of the mirror varies across the detector. Generally, for *ASCA* and *XMM-Newton* observations the ARF must be generated for each observation.

In theory, the measured counts spectrum  $C(I)$  could be inverted to find the source spectrum by using the known quantities  $R(E, I)$  and  $A(E)$  in the RMF and ARF. In reality, this inversion process is not unique and is challenging because small errors in the counts spectrum have a large effect on the recovered source spectrum.

The problems with the inversion process generally require that the source flux spectrum be found by forward fitting. A model source spectrum,  $M(E)$ , is produced that depends on a few variable parameters. This model spectrum is combined with the RMF and ARF file to generate a model counts spectrum:

$$C_p(I) = \int_0^\infty M(E) R(E, I) A(E) dE.$$

Then, the model counts spectrum is compared with the actual observed counts spectrum,  $C(I)$  (the observed data), in order to ascertain if the model spectrum is a good representation of the source spectrum. If the model does not lead to a good match with the data, then the model parameters are varied until it does.

This comparison and the adjustment of the model parameters is done by numerically minimizing the goodness of fit parameter  $\chi^2$ :

$$\chi^2 = \sum \frac{(C(I) - C_p(I))^2}{\sigma(I)^2},$$

where  $\sigma(I)$  is the uncertainty associated with the data in channel  $I$ . In practice, the X-ray counts spectrum is binned up so that the number of counts in each channel is great enough to allow the use of Gaussian statistics, where  $\sigma(I) = \sqrt{C(I)}$ . In this thesis, the actual generation of the model and the numerical fitting is done by the computer program *XSPEC*, which is widely used in X-ray astronomy.

The value of  $\chi^2$  is an indicator of the goodness of fit. When  $\chi^2/\nu \approx 1$  (where  $\nu$  is the number of degrees of freedom in the fit), the fit is judged acceptable. When  $\chi^2/\nu$  (called the reduced chi-square,  $\chi_r^2$ ) is much greater than one, then the model is judged an inaccurate representation of the source spectrum. Roughly, a value of  $\chi_r^2 < 1.4$  is an acceptable fit.

The  $\chi_r^2$  statistic can also be used to ascertain the likely errors on the fit parameters of the model. A single parameter of the model is varied until the  $\chi^2$  of the overall fit rises from its minimum by a certain amount. This range in the parameter is called the confidence interval around the parameter, and means that if the fit were repeated many more times with data drawn from the same statistical distribution, the true value of the parameter would lie in the confidence interval. For example, the 90% confidence interval is defined to be the range of the parameter that causes  $\chi^2$  to change by  $\Delta\chi^2 = 2.71$ . If this fit were to be repeated many times with data from the same distribution, then the true value of the parameter would fall within the 90% confidence interval 90% of the time.

# Bibliography

Tanaka, Y., Inoue, H., & Holt, S. S. 1994, PASJ, 46, L37

# Chapter 3

## Oxygen Abundances in the Milky Way Using X-ray Absorption Measurements Towards Galaxy Clusters

### Abstract

We present measurements of the oxygen abundance of the Milky Way's ISM by observing the K-shell X-ray photoionization edge towards galaxy clusters. This effect is most easily observed towards objects with galactic columns ( $n_H$ ) of a few times  $1.0 \times 10^{21} \text{ cm}^{-2}$ . We measure X-ray column densities towards 11 clusters and find that at high columns above about  $1.0 \times 10^{21} \text{ cm}^{-2}$  the X-ray columns are generally 1.5–3.0 times the 21 cm H I columns, indicating that molecular clouds become an important contributor to  $n_H$  at higher columns. We find the ISM oxygen abundances to be  $(\text{O}/\text{H}) = (4.46 \pm 0.11) \times 10^{-4}$ , or 0.9 solar when using the most recent solar photospheric values. Since X-ray observations are sensitive to the total amount of

oxygen present (gas + dust), these results indicate a high gas to dust ratio. Also, the oxygen abundances along lines of sight through high galactic columns ( $n_H$ ) are the same as abundances through low columns, suggesting that the composition of denser clouds is similar to that of the more diffuse ISM.

### 3.1 Introduction

The measurement of the chemical abundances in our galaxy has been an important continuing area of research in astronomy because knowledge of these abundances has a significant impact on many other areas. Measurements constrain theories of primordial nucleosynthesis, and are a strong constraint on models of elemental production in stars and chemical evolution of the galaxy.

Measurements of galactic abundances are usually measured in stars by observing specific optical lines from the stellar atmosphere. Measurements of abundances in other galactic objects such as H II regions and planetary nebulae proceed along the same lines. Two questions that are always asked of these measurements are whether the result is a true measure of the chemical abundances in the object, and whether this measurement is indicative of the true abundances of the galaxy.

The optical measurements of chemical abundances in stellar atmospheres depend heavily on the particular model used to fit and interpret the result, which depends on a correct determination of the ionization balance, line blending and other physical processes like microturbulence, granulation, and non-LTE effects. In the case of oxygen, a steady procession of papers (Anders & Grevesse 1989; Grevesse & Sauval 1998; Allende Prieto, Lambert, & Asplund 2001; Wilms, Allen, & McCray 2000; Asplund et al. 2003) has shown how the determined solar abundance has changed substantially over time as the models have been revised. Also, optical measurements

can typically be made for only a few ionization states of any given element, further complicating a determination of a total elemental abundance.

Another obstacle to determining chemical abundances with optical observations is the unknown gas to dust ratio. Since the optical lines measured in the ISM are produced only by gas, the fraction of the elemental abundance tied up in dust or other ionization states is not well determined. When this abundance for the gas is compared to a standard solar composition, it often is less than the sun. This difference is usually attributed to depletion of the element onto dust grains in the ISM, although no direct measurement of the dust abundance was made. Direct measurements of the composition of the dust are difficult because they depend on assumptions about hard to determine parameters such as grain sizes and distributions.

We address these problems by observing a sample of eleven galaxy clusters with the X-ray observatory *XMM-Newton*. We use the clusters as a background white light source against which we can see the absorption edge at 542 eV produced by photoionization of the inner K-shell electrons of oxygen. Dust grains are transparent to X-rays of this energy, and the total oxygen cross section is not very sensitive to ionization stage. Measurements of the K-shell oxygen edge therefore provide an excellent measure of the total oxygen column along the line of sight, and when combined with a measurement of the total hydrogen column can yield an oxygen abundance determined with X-ray observations sensitive to dust and to all ionization levels of the gas phase.

Galaxy clusters provide one of the best sets of available X-ray sources for observing galactic abundances in absorption. Clusters are bright, and have relatively simple spectra at the energies of interest. Their spectra are dominated by continuum emission caused by thermal bremsstrahlung in the hot intracluster plasma. They

are extragalactic, occur at all galactic latitudes, and their emission does not change appreciably on terrestrial time scales. They are optically thin and have no intrinsic absorption to complicate galactic measurements. Further, a few bright clusters are objects suitable for observation by high resolution gratings; however, we limit ourselves to imaging spectroscopy in this paper.

The *XMM-Newton* satellite is the ideal instrument for this purpose because of its very high sensitivity and good CCD spectral resolution. Also, its low energy broad band response below 2 keV has a fairly well understood calibration, which has not always been the case for X-ray telescopes at this energy.

### 3.1.1 ISM Observations

Until recently, observations of the Milky Way ISM such as those made by Fitzpatrick (1996) using absorption lines towards halo stars with GHRS have shown that the galactic abundances were subsolar. This result also held for oxygen explicitly (Meyer, Jura, Hawkins, & Cardelli 1994; Cardelli, Meyer, Jura, & Savage 1996). These observations, along with others such as the one by Cardelli et al. (1994) that found the ISM krypton abundance to be 60% of the solar value led to the idea that the ISM abundances were about  $\frac{2}{3}$  the solar values (Mathis 1996). Sofia & Meyer (2001) later summarized these developments and showed that they were no longer tenable because of new data such as the lower solar oxygen abundance of Holweger (2001). Recent data from *FUSE* observations of many ISM sightlines (André et al. 2003; Jensen, Rachford, & Snow 2003) show that the ISM gas phase oxygen abundance is  $(\text{O}/\text{H})_{\text{gas}} = 4.08 \times 10^{-4}$  and  $4.39 \times 10^{-4}$ , respectively. This is close to the solar value from Asplund et al. (2003) of  $4.79 \times 10^{-4}$ , and supports only mild depletion of oxygen in the ISM. Other *FUSE* results from Oliveira et al. (2003) support a lower gas phase oxygen abundance of  $3.63 \times 10^{-4}$  along the lines of sight

towards four white dwarfs.

X-ray observations of absorption in the ISM have produced similar results. Arabadjis & Bregman (1999) used the PSPC on *ROSAT* to measure the X-ray hydrogen column  $n_{H_X}$  towards 26 clusters and found that the X-ray column exceeds the 21 cm column for columns above  $5 \times 10^{20} \text{ cm}^{-2}$  and that extra absorption from molecular hydrogen is required. Higher resolution grating observations of the ISM with *Chandra* (de Vries et al. 2003; Juett, Schulz, & Chakrabarty 2003) have started to reveal the structure of the oxygen K-edge and put constraints on the oxygen ionization fraction. Juett, Schulz, & Chakrabarty (2003) have found that the ratio of O II/O I  $\approx 0.1$ , and that the precise energy of the gas phase oxygen K-edge is 542 eV.

The resolution of the grating observations from *Chandra* and *XMM-Newton* are unsurpassed, and allow for a very careful determination of the absorbing galactic oxygen column towards background sources (Paerels et al. 2001; Juett, Schulz, & Chakrabarty 2003; de Vries et al. 2003; Page et al. 2003). However, the hydrogen column towards these sources is often not measured directly and as a result the oxygen abundance is not obtained. Paerels et al. (2001) using the *Chandra* LETGS did derive an equivalent  $n_H$  from the overall shape of the spectrum towards the galactic X-ray binary X0614+091, and obtained an oxygen abundance of 0.93 solar. Weisskopf et al. (2004) performed a similar measurement towards the Crab with the *Chandra* LETGS and obtained a galactic oxygen abundance of 0.68 solar. Willingale et al. (2001) has used the MOS CCD detectors onboard *XMM-Newton* to measure the abundance towards the Crab and finds an oxygen abundance of 1.03 solar, and Vuong et al. (2003) presents measurements towards star forming regions that are best fit with the new solar abundances. All of these abundances are with respect to the Wilms, Allen, & McCray (2000) solar abundance scale.

### 3.1.2 Solar Abundances

There has been some controversy in the literature as to the canonical values to use for the solar elemental abundances. The values for the elemental abundances by number that are found for metals by fitting to X-ray spectra do not depend on the chosen values for the solar abundances. However, for the sake of convenience elemental abundances are often reported with respect to the solar values.

The compilation of Anders & Grevesse (1989) has been a standard for this purpose. They published abundances for the natural elements compiled from observations of the solar photosphere and from measurements of primitive CI carbonaceous chondritic meteorites. For many of the elements presented, there was a good agreement between the meteoritic and photospheric values for elements where both types can be measured. However, there was still a discrepancy for some important elements such as iron.

Since 1989, the situation has improved. Reanalysis of the stellar photospheric data for iron that includes lines from Fe II in addition to Fe I as well as improved modeling of the solar lines (Grevesse & Sauval 1999) have brought the meteoritic and photospheric values into agreement. Grevesse & Sauval (1998) incorporate these changes and others. Of more importance to our work on the galactic oxygen abundance, the solar abundances of carbon, nitrogen, and oxygen have also changed since the compilation of Anders & Grevesse (1989). Measurements of these elements in the sun cannot be easily reconciled with meteoritic measurements because they form gaseous compounds easily and are found at much lower abundances in the CI meteorites than in the sun. Holweger (2001); Allende Prieto, Lambert, & Asplund (2001); Asplund et al. (2003) have made improvements to the solar oxygen abundance by including non-LTE effects, using three dimensional models, deblending

unresolved lines, and incorporating a better understanding of solar granulation on the derived measurements. The carbon (Allende Prieto, Lambert, & Asplund 2001) and nitrogen (Holweger 2001) abundances have also improved in a similar fashion, as reported by Lodders (2003). The Wilms, Allen, & McCray (2000) compilation available in `XSPEC` has solar abundance values for carbon, nitrogen, and oxygen ( $O/H = 4.90 \times 10^{-4}$  by number) consistent with the most recent values. These downward revisions in the solar photospheric oxygen abundance have allowed ISM oxygen measurements to finally agree with the solar standard.

## 3.2 X-ray Observations

### 3.2.1 Sample Selection

Our sample of 11 galaxy clusters was chosen from the public archives of the *XMM-Newton* satellite. The main criteria for selection are that the cluster have a hydrogen column greater than  $0.5 \times 10^{21} \text{ cm}^{-2}$  and that the observation have more than  $5 \times 10^4$  counts in the EPIC spectra in order to ensure a good measurement of the absorption from galactic oxygen.

The choice of  $n_H$  greater than  $0.5 \times 10^{21} \text{ cm}^{-2}$  was set by the need to have galactic oxygen optical depths near  $\tau = 1$  in order to allow good measurements of the oxygen abundance. Figure 3.1 shows how the galactic oxygen optical depth is related to  $n_H$  given an ISM with the solar abundances of Wilms, Allen, & McCray (2000). An oxygen optical depth of 1.0 is reached at a hydrogen column of about  $1.5 \times 10^{21} \text{ cm}^{-2}$ .

Reference data for these clusters can be found in Table 3.1. We include the cluster coordinates, the  $n_H$  column from the 21 cm work of Dickey & Lockman (1990), previously determined X-ray values for the cluster temperature and metallicity from

Table 3.1. Cluster Reference Values

Cluster	RA [J2000.0]	dec	l	b	$n_H^a$	$A_B^b$	$E(B - V)^c$	IRAS <sup>d</sup> 100 $\mu\text{m}$	$kT$ [keV]	$Z^e$	$z$	Exposure [ksec]	XMM Rev.
PKS 0745-19	116.883	-19.296	236.444	3.030	$4.24 \times 10^{21}$	2.252	0.522	36.9	6.25	0.61	0.103	17.61	164
ABELL 401	44.737	13.582	164.180	-38.869	$1.05 \times 10^{21}$	0.678	0.157	10.2	8.07	0.49	0.074	12.80	395
Tri aus	249.585	-64.516	324.478	-11.627	$1.30 \times 10^{21}$	0.592	0.137	7.7	10.19	0.45	0.051	9.40	219
AWM7	43.634	41.586	146.347	-15.621	$0.98 \times 10^{21}$	0.504	0.117	5.5	3.71	0.89	0.018	31.86	577
ABELL 478	63.336	10.476	182.411	-28.296	$1.51 \times 10^{21}$	2.291	0.531	18.1	7.07	0.54	0.088	46.77	401
RX J0658.4-5557	104.622	-55.953	266.030	-21.253	$0.65 \times 10^{21}$	0.335	0.078	4.6	11.62	0.28	0.296	21.05	159
ABELL 2163	243.892	-6.124	6.752	30.521	$1.21 \times 10^{21}$	1.528	0.354	21.8	12.12	0.38	0.203	10.99	132
ABELL 262	28.210	36.146	136.585	-25.092	$0.54 \times 10^{21}$	0.373	0.086	4.3	2.17	0.87	0.016	23.62	203
2A 0335+096	54.647	9.965	176.251	-35.077	$1.78 \times 10^{21}$	1.771	0.410	18.9	2.86	1.01	0.035	1.81	215
ABELL 496	68.405	-13.246	209.568	-36.484	$0.46 \times 10^{21}$	0.586	0.136	4.0	3.89	0.82	0.033	30.14	211
CIZA 1324	201.180	-57.614	307.394	4.969	$3.81 \times 10^{21}$	3.164	0.733	36.8	3.00	0.87	0.019	10.76	675

<sup>a</sup>Values are the hydrogen column [atoms  $\text{cm}^{-2}$ ] from the 21 cm work of Dickey & Lockman (1990).

<sup>b</sup>From Schlegel, Finkbeiner, & Davis (1998).

<sup>c</sup>From NED.

<sup>d</sup>Values in  $\text{MJy sr}^{-1}$  taken from the all sky maps of Schlegel, Finkbeiner, & Davis (1998).

<sup>e</sup>Total metal abundance from Horner (2001), rescaled from the Anders & Grevesse (1989) to the Wilms, Allen, & McCray (2000) solar abundances.

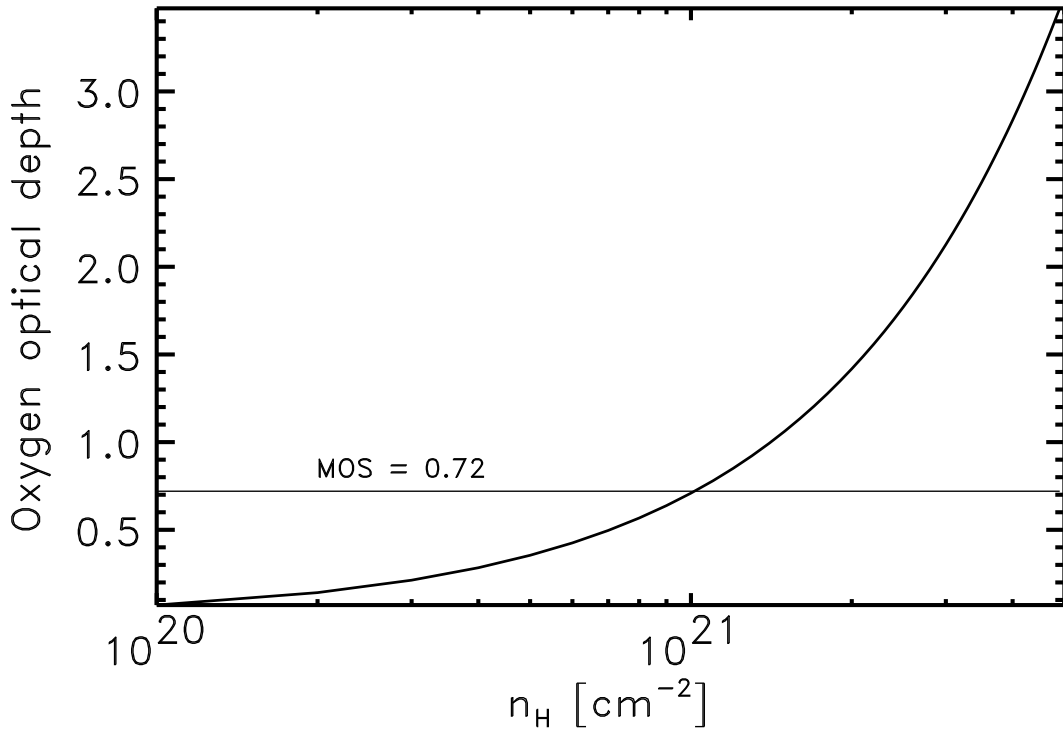


Figure 3.1: The MW ISM optical depth in oxygen K-shell absorption as a function of the hydrogen column density for an ISM with standard solar abundances as given in Wilms, Allen, & McCray (2000). The optical depth of the oxygen edge in the MOS detectors resulting from filters, windows, etc. is also plotted for comparison and is  $\tau = 0.72$ .

the *ASCA* observations in Horner (2001) and Horner et al. (ApJS submitted), the optical redshift, the optical extinction, color excess, *IRAS* 100  $\mu\text{m}$  count, and the length of the *XMM-Newton* exposure.

The requirement of a high  $n_H$  column places most of our sample near the galactic plane. Figure 3.2 shows the location of each of the clusters in our sample superimposed upon the all sky map of the 100  $\mu\text{m}$  emission observed by *IRAS*. The *IRAS* map is a good tracer of dust in the galaxy, and shows that the clusters in our sample that do not lie in the galactic plane are still located in areas with high  $n_H$ . Figure 3.2 also shows that our clusters sample a wide range of galactic sight lines.

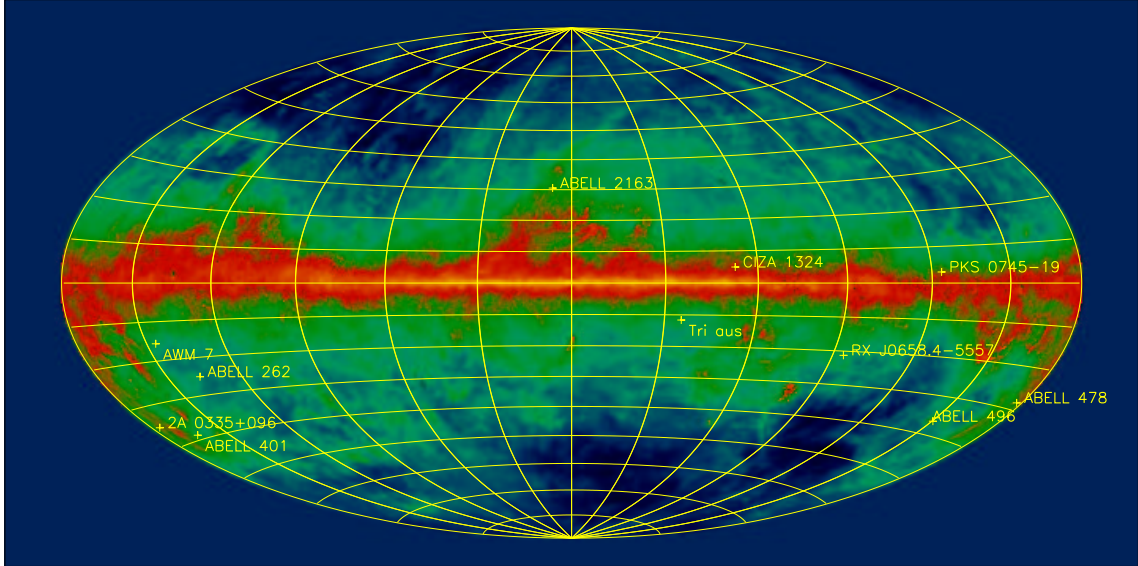


Figure 3.2: A map showing the location of the clusters in our sample. Each cluster is shown plotted on a full sky map in galactic coordinates, with the galactic center at the figure center. The color image is the *IRAS* 100  $\mu\text{m}$  map, a good tracer for dust in the galaxy.

### 3.2.2 Data Reduction

We extracted spectra from the pn and two MOS CCD detectors that comprise the EPIC camera on *XMM-Newton*. These detectors' moderate resolution of 50–100 eV and large field of view are well matched to our requirements. The cluster data are re-reduced from the raw ODF files using SAS version 5.4.1 in order to incorporate the most recent calibration data. After filtering to eliminate periods with high background rates, we choose regions on the CCDs that encompass most of a cluster's emission without a significant contribution from the background. Backgrounds were local, and taken from areas in the field of view without cluster emission. Ancillary response files and response matrices are generated using `arfgen` and `rmfgen` within SAS.

We extracted spectra between 0.49–10.0 keV in the MOS1 and MOS2 detectors, and between 0.48–7.2 keV in the pn in order to avoid large background lines above

7.2 keV in the pn. Our lower energy cutoff is 0.48 keV in order to avoid problems with the calibration of the redistribution function at very low energies. Since the spectral region of interest for our analysis is around the oxygen edge at 0.542 keV, this lower energy cutoff should have little effect on the results.

### 3.2.3 Extra Edge

In order to obtain the greatest signal to background ratio, we would like to fit the data from all three CCD detectors on *XMM-Newton*. However, early on we discovered that oxygen absorption results from the three detectors did not agree. While the MOS detectors showed substantial absorption, the pn detector showed almost none. We examined data from an *XMM-Newton* observation of the bright quasar 3C 273 (a good continuum source at the energies of interest) in order to investigate this effect at low galactic columns (3C 273 has  $n_H = 1.8 \times 10^{20} \text{ cm}^{-2}$ ). We found that there are substantial residuals in the MOS detectors at the location of the oxygen edge. Figure 3.3 shows the residuals to the 3C 273 fit at the location of the oxygen edge and illustrates the large deviation in the MOS detectors. We also observe this effect towards the Coma cluster, another low galactic column source ( $n_H = 9.2 \times 10^{19} \text{ cm}^{-2}$ ).

We interpret this effect as an inaccuracy in the response matrices for the MOS detectors. Such an effect could possibly be caused by the outgassing of organic materials onto the surface of the MOS detectors, and is seen in observations taken with both the thin and medium filters. The oxygen edge in the detector is caused by molecular compounds of oxygen, and its energy of 0.53 keV is slightly offset from the ISM atomic edge at 0.542 keV. However, the correct determination of this instrumental feature will strongly effect any measurements of the ISM oxygen abundance. Figure 3.4 shows the magnitude of the instrument edge in the MOS

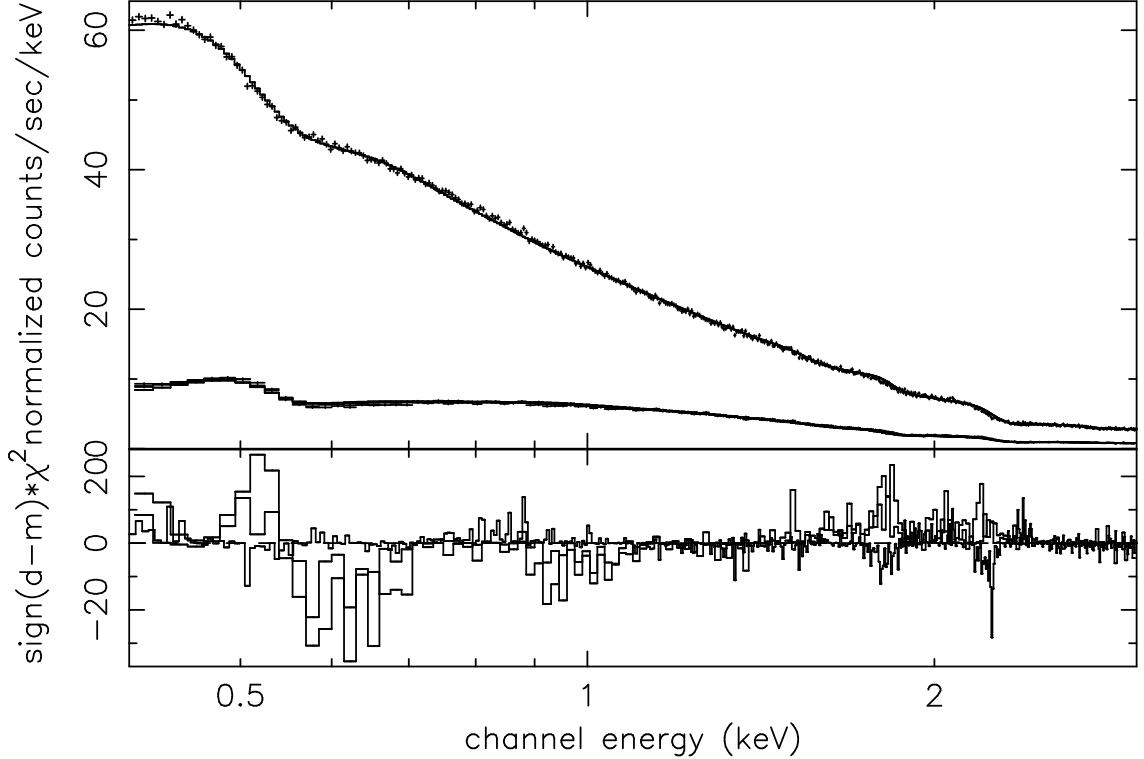


Figure 3.3: A spectral fit to the bright quasar 3C 273 with the 3 CCD detectors of the EPIC camera on *XMM-Newton*. The residuals above the oxygen edge at 544eV show the large discrepancy between detectors; the pn detector is well fit, while the MOS detectors have significant residuals. We address this problem by including an extra edge to the model that is discussed in section §3.2.3.

detectors.

We compensate for this problem by introducing an extra edge into the fit at the solid state oxygen K-shell energy of 0.53 keV. When the extra edge component has optical depths of 0.22 for the MOS1 and 0.20 for the MOS2 the fitted oxygen absorption is consistent between all three detectors for 3C 273 and Coma, so we use these values for our cluster fits.

This problem has been brought to the attention of the *XMM-Newton* EPIC instrument team. They have kindly supplied a beta version of a revised quantum efficiency file that is meant to address this problem. The tests we have made using this file have provided results that are consistent with the extra edge method

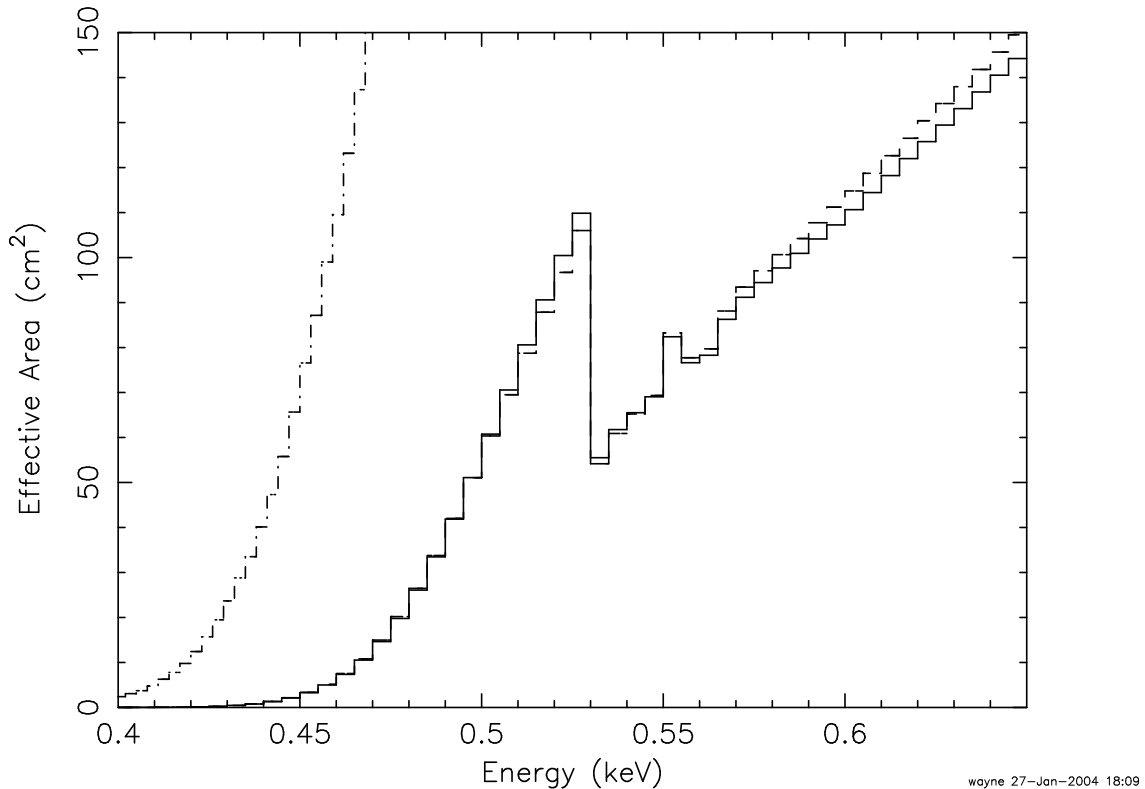


Figure 3.4: The instrumental response of the MOS detector in the region of the oxygen edge. The optical depth of the instrumental edge is  $\tau = 0.72$ . The trace on the left is the response of the pn detector.

described above.

### 3.2.4 Spectral Fitting

We use XSPEC version 11.3.0 to fit the data. The cluster emission is modeled by the `apec` (v. 1.3.1) plasma code (Smith, Brickhouse, Liedahl, & Raymond 2001), and the intervening galactic material by the `tbvarabs` model (Wilms, Allen, & McCray 2000) (XSPEC model: `edge * tbvarabs * apec`; the edge component of the model is discussed in §3.2.3).

The `tbvarabs` model models the absorption due to photoionization from the abundant elements up to nickel. It also takes into account absorption from molecular hydrogen and depletion of the elements onto grains. The abundance of each of

the elements can be individually fit, as well as the depletion fraction. The model elemental abundances are computed from the observables (e.g., spectral line equivalent width, optical depth) by specifying a table of solar elemental abundances selectable by the user. We choose the compilation of theoretical X-ray absorption cross sections by Verner, Ferland, Korista, & Yakovlev (1996)<sup>1</sup>, and the solar abundances of Wilms, Allen, & McCray (2000)<sup>2</sup>. Although Lodders (2003) has published a more recent compilation, we feel that her solar abundance for helium that takes into account heavy element settling in the sun results in an abundance that is too low for good ISM modeling. Her compilation of recent results for carbon, nitrogen, and oxygen need to be taken into account. However, the Wilms et al. model has very similar abundances for carbon and nitrogen, and precisely the same abundance for oxygen. Because carbon and nitrogen have less of an effect on our fits than oxygen, we use the Wilms et al. abundances.

For our investigation, the dominant contributors to galactic absorption are hydrogen, helium, and oxygen. Secondary contributors observable in the *XMM-Newton* band are neon and iron (from the L-shell). We initially set the hydrogen column to the Galactic 21 cm value from Dickey & Lockman (1990), but allow it to vary with the fit. The helium abundance is not well constrained independently of the hydrogen value, and is set to solar in our fit. Neon and iron are also initially set to their solar abundance values, but are allowed to vary with the fit. All other elements are fixed to their solar abundance values as determined by Wilms, Allen, & McCray (2000). The grain and depletion parameters are set to their default value in the `tbvarabs` model, but these parameters do not significantly affect the results of our fitting. All of the parameters in the `tbvarabs` portion of the model are

---

<sup>1</sup>implemented with the XSPEC command: `xsect vern`

<sup>2</sup>implemented with the XSPEC command: `abund wilm`

constrained to have the same value for each of the three EPIC detectors.

Initial values for the cluster temperature, metal abundance, and redshift are given in Table 3.1, taken from the work of Horner (2001). The cluster temperature and metal abundance are constrained to have the same value for the three EPIC detectors, but the cluster redshift is allowed to vary separately in each detector in order to compensate for any small gain errors in the data.

The spectrum with residuals to the fit for a typical cluster are given in Figure 3.5.

In the top panel we show the spectrum fit with the model, while in the bottom panel we set the galactic oxygen abundance to zero to illustrate the strength of the absorption signal.

### 3.3 Results

The results from the spectral fits are shown in Table 3.2. The main results are for the elemental abundance of galactic oxygen along the line of sight towards the background cluster and are given in column 6. We also give the results for the observed X-ray column of galactic hydrogen in column 5 of the table. Columns 7, 8, and 9 of the table are meant to illustrate the quality of the fit and list the number of photons in the X-ray spectrum from all three EPIC detectors, the reduced  $\chi^2$ , and the number of degrees of freedom of the fit.

#### 3.3.1 Hydrogen

The total galactic hydrogen column density is composed of several parts: the neutral atomic gas measured by 21 cm radio observations; the warm, ionized H II gas that is sometimes associated with H $\alpha$  emission; and molecular hydrogen, H<sub>2</sub>, often associated with CO emission. The X-ray measure of the hydrogen column,  $n_{HX}$ , is

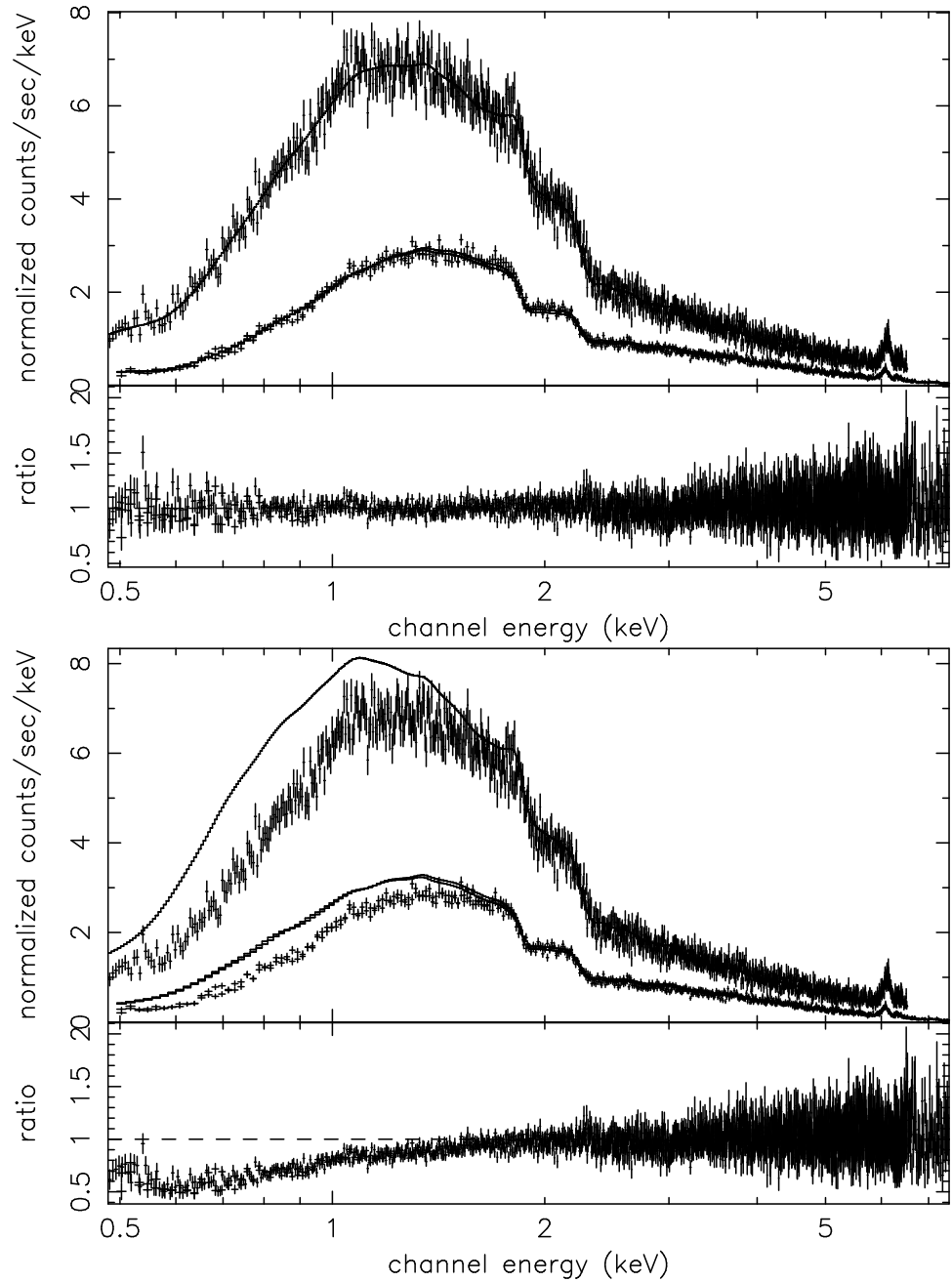


Figure 3.5: Fits to the cluster PKS 0745-19. The data are shown with errors and the model is a solid line in the top plot of each panel. The residuals are shown in the bottom plot of each panel. The top panel shows that the overall fit is good to a model that includes an extra edge component in the MOS detectors, as is the .5 keV region where the oxygen signal lies. The biggest residual is at 1 keV and is from iron L-shell emission, and does not affect the oxygen fit. In the bottom panel, the data was first fit with the standard model. Then, the model oxygen abundance was arbitrarily set to zero to illustrate the strength and importance of the galactic oxygen absorption component.

Table 3.2. X-ray Determined Galactic Absorption towards Galaxy Clusters

Cluster	$z$	$kT$ [keV]	$Z^a$	$n_H^b$	Oxygen <sup>c</sup> abundance	Counts <sup>d</sup>	$\chi^2$ per dof	dof
PKS 0745-19	0.100	7.173	0.68	$5.550_{5.260}^{5.910}$	$0.77_{0.60}^{0.93}$	3.7e+05	1.10	2113
ABELL 0401	0.069	8.730	0.58	$1.050_{0.970}^{1.130}$	$0.55_{0.37}^{0.82}$	2.8e+05	1.06	1910
Tri aus	0.050	10.098	0.58	$1.520_{1.440}^{1.600}$	$1.00_{0.82}^{1.20}$	4.2e+05	1.05	2194
AWM7	0.016	3.637	1.14	$1.090_{1.070}^{1.110}$	$1.09_{1.01}^{1.16}$	1.4e+06	1.24	2354
ABELL 0478	0.082	6.587	0.67	$3.580_{3.510}^{3.640}$	$1.04_{0.96}^{1.11}$	1.9e+06	1.43	2344
RX J0658.4-5557	0.298	12.789	0.39	$0.220_{0.170}^{0.270}$	$1.22_{0.21}^{2.38}$	1.5e+05	0.99	1466
ABELL 2163	0.194	13.036	0.40	$2.190_{2.020}^{2.420}$	$0.89_{0.59}^{1.17}$	1.1e+05	1.02	1420
ABELL 0262	0.014	2.058	0.78	$1.060_{1.020}^{1.080}$	$0.43_{0.33}^{0.53}$	4.4e+05	1.48	1723
2A 0335+096	0.034	2.654	0.97	$3.160_{2.930}^{3.340}$	$0.83_{0.62}^{1.04}$	5.8e+04	1.17	930
ABELL 0496	0.031	3.544	0.95	$0.620_{0.600}^{0.640}$	$0.89_{0.78}^{1.02}$	5.8e+05	1.28	2051
CIZA 1324	0.018	2.944	0.94	$6.010_{5.470}^{6.440}$	$1.18_{0.78}^{1.68}$	8.8e+04	1.09	1217

Note. — All values are from the X-ray fit to the *XMM-Newton* data. Values in sub and superscript are the range of the 90% confidence interval.

<sup>a</sup>Cluster metal abundance with respect to Wilms, Allen, & McCray (2000).

<sup>b</sup>Total hydrogen column in units of  $10^{21}\text{cm}^{-2}$ .

<sup>c</sup>The oxygen abundance of the galactic absorption component is given with respect to the solar value of Wilms, Allen, & McCray (2000).

<sup>d</sup>Total counts in the EPIC detectors after background particle filtering.

sensitive to all these forms and is indicative of the total hydrogen column.

The X-ray total column is also sensitive to the helium component along the line of sight. At the X-ray energies of these observations, the absorption cross section due to helium is substantial and is greater than the hydrogen component. However, the helium is mostly primordial in origin and the hydrogen to helium ratio in the galaxy is assumed to be uniform. Therefore, variations in the helium abundance or distribution are not expected to have a significant effect on the total hydrogen

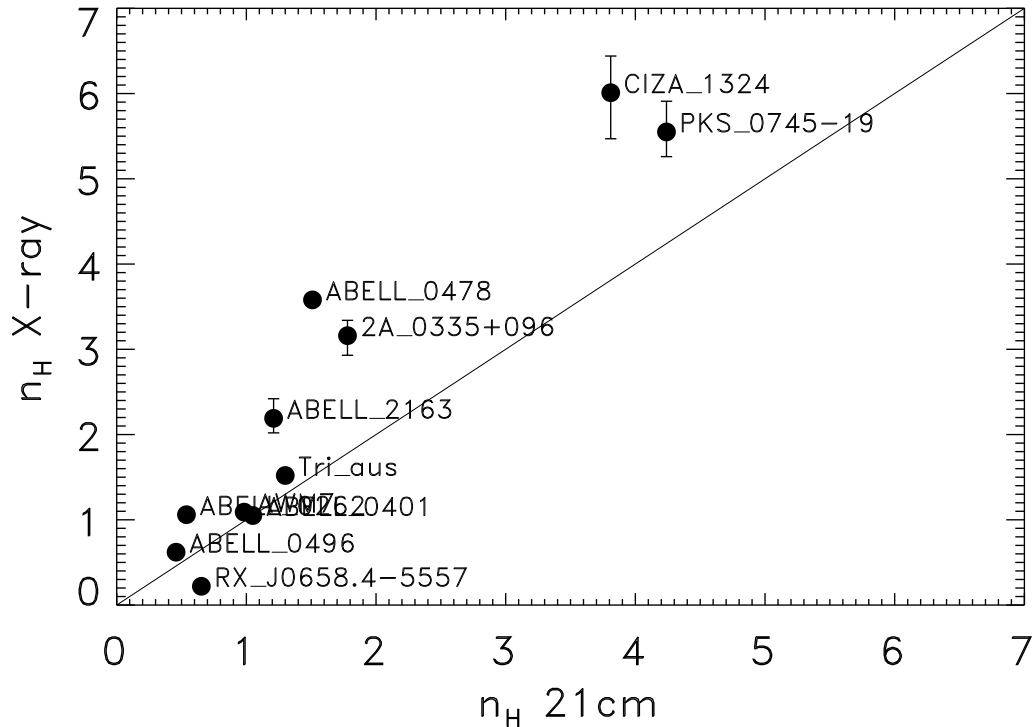


Figure 3.6: The X-ray total hydrogen column density plotted against the neutral hydrogen value derived from the 21 cm observations in Dickey & Lockman (1990). The hydrogen columns are in units of  $10^{21}$  atoms  $\text{cm}^{-2}$ . The X-ray values are generally higher because these observations are sensitive to all forms of hydrogen and detect  $\text{H}_2$  that could not be seen with the 21 cm observations. The molecular component of  $n_H$  becomes most important above columns of  $\sim 0.5 \times 10^{21}$   $\text{cm}^{-2}$  where the  $\text{H}_2$  is sufficiently dense enough to shield itself from dissociating radiation from hot young galactic stars.

columns.

Figure 3.6 shows the X-ray determined total hydrogen column plotted against the column of neutral hydrogen measured by the 21 cm observations of Dickey & Lockman (1990). The X-ray measure of the hydrogen column is well correlated with the 21 cm observations, as well as with the optical reddening  $E_{B-V}$  determined by *IRAS* (Schlegel, Finkbeiner, & Davis 1998) as shown in Figure 3.7. The direct comparison of the X-ray and 21 cm derived columns in Figure 3.6 shows that the

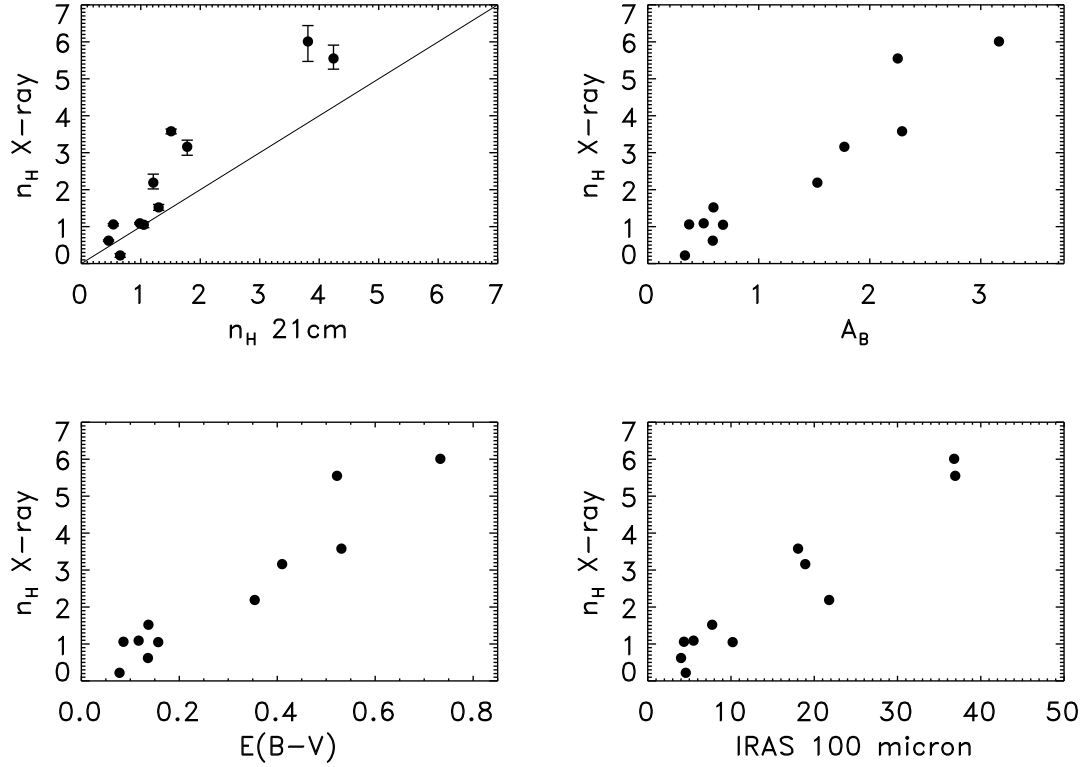


Figure 3.7: The correlation of  $n_H$  derived from X-ray observations with other measures of the ISM towards the lines of sight of the 11 clusters in our sample. The top left panel shows  $n_{H_X}$  against the 21 cm radio observation of neutral atomic hydrogen [the data are in units of  $10^{21} \text{ cm}^{-2}$ ]; the top right panel shows  $n_{H_X}$  against the  $B$ -band optical extinction data in magnitudes; the lower left panel shows  $n_{H_X}$  against the optical reddening; and the lower right panel shows  $n_{H_X}$  against the *IRAS* 100 $\mu\text{m}$  emission in  $\text{MJy sr}^{-1}$ . The X-ray emission is better correlated with the reddening and *IRAS* emission which are also sensitive to the effects of dust and molecular clouds.

X-ray columns are in general higher than the 21 cm ones. Arabadjis & Bregman (1999) (AB) showed that below columns of about  $0.5 \times 10^{21} \text{ atoms cm}^{-2}$  the X-ray derived  $n_H$  column closely matches the 21 cm value, suggesting that neutral atomic hydrogen can account for all of the observed column below these densities. However, above  $0.5 \times 10^{21} \text{ atoms cm}^{-2}$ , the X-ray column exceeds the 21 cm column and the contribution from other hydrogen sources such as molecular hydrogen become important. This effect can most easily be seen by plotting the ratio of the X-ray

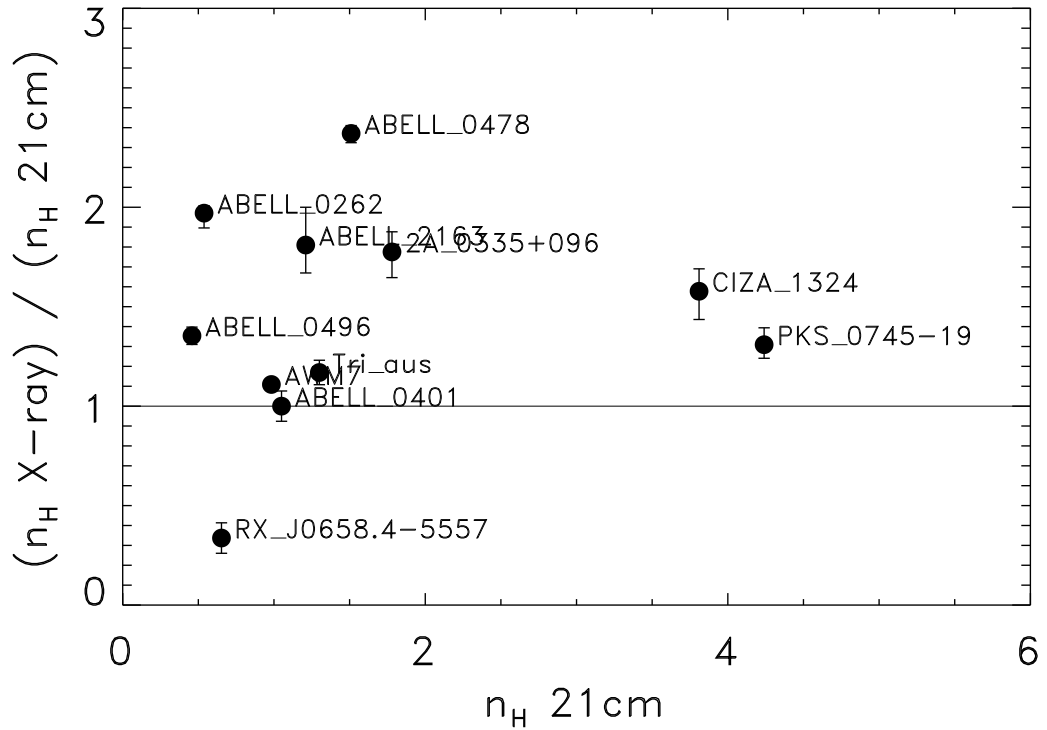


Figure 3.8: The overabundance of the X-ray derived  $n_H$  compared to the 21 cm derived value.

to 21 cm column as a function of the X-ray column, as we do with our data in Figure 3.8.

Many of the clusters in our sample are common to the sample of AB. However, the *XMM-Newton* spectra of our sample extend to higher energies and are better able to characterize the thermal emission of the underlying cluster. In Figure 3.9 we plot our derived X-ray columns against those of AB and find that they are in good agreement.

Figure 3.8 indicates that above columns of  $0.5 \times 10^{21}$  atoms  $\text{cm}^{-2}$  the total hydrogen column cannot be accounted for solely by neutral atomic hydrogen and that other contributors must be taken into account. These contributors include ionized hydrogen, H II, and molecular hydrogen,  $\text{H}_2$ , discussed in the sections below.

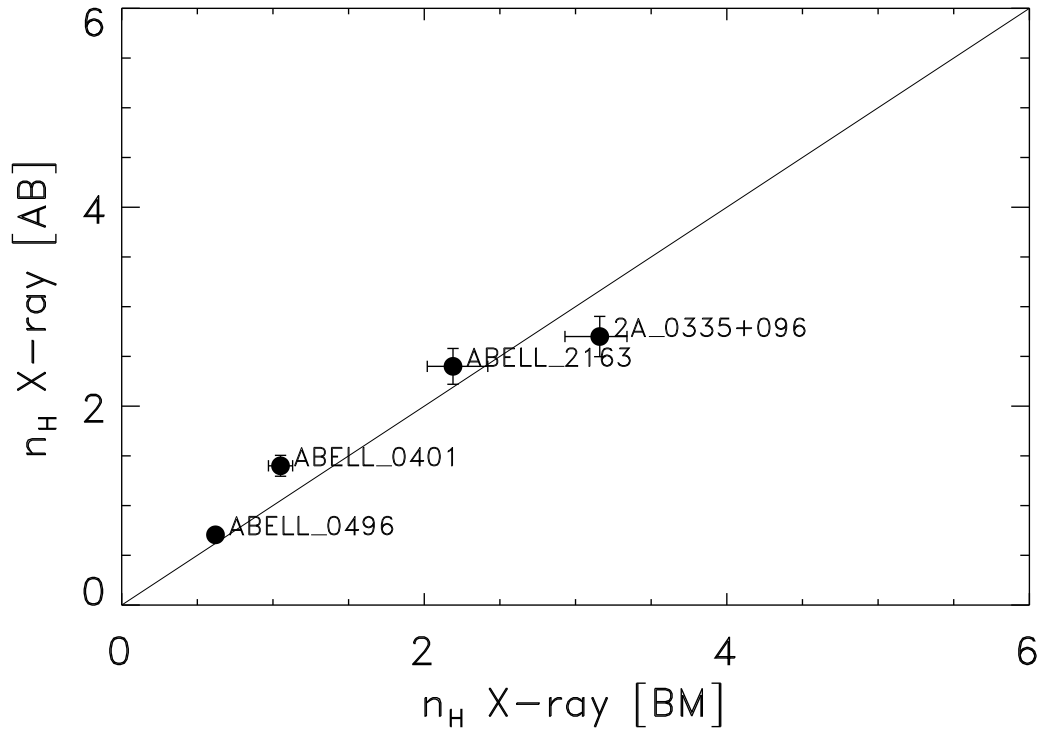


Figure 3.9: A comparison of the Arabadjis & Bregman (1999) X-ray derived  $n_H$  values to those in this study.

It is also possible that for high columns the 21 cm derived columns are incorrect because they assume that the neutral atomic hydrogen is optically thin. At higher columns, the gas becomes sufficiently optically thick to undergo self shielding and self-absorption. Strasser & Taylor (2004) have conducted an emission-absorption study of H I in the galactic plane which measures this effect. They have found that the 21 cm columns derived from emission alone (such as Dickey & Lockman (1990)) require only a  $\sim 2\%$  correction at columns of  $1.0 \times 10^{21}$  atoms  $\text{cm}^{-2}$  in order to arrive at the actual galactic hydrogen column. This correction is less than the statistical error of our X-ray fits and so we ignore it.

## Ionized Hydrogen

The contribution of ionized H II to the total column  $n_H$  is small. AB noted in their study that below columns of  $0.5 \times 10^{21}$  atoms  $\text{cm}^{-2}$  the X-ray total column can be completely explained solely by contributions from neutral atomic hydrogen as measured by 21 cm observations. Laor et al. (1997) observed the X-ray spectra of AGN and came to a similar conclusion. Attempts to constrain H II using *IRAS* 100  $\mu\text{m}$  data by Boulanger et al. (1996) have also led to low values for H II, with Kuntz (2001) suggesting that less than 20% of the *IRAS* emission can be associated with H II.

Recently, the *WHAM* project has measured H II emission by observing at  $\text{H}\alpha$  (Haffner et al. 2003). They also find that H II is not a significant contributor to  $n_H$ .

## Molecular Hydrogen and CO Measurements

CO emission is known to be correlated with concentrations of molecular hydrogen. Although the correspondence does not hold exactly for all densities, the correlation is sufficient that a constant coefficient can be used to estimate the amount of  $\text{H}_2$  present from the measured CO emission. The value of this so-called X factor is somewhat controversial and is thought to vary somewhat depending on the local environment. However, Dame, Hartmann, & Thaddeus (2001) have measured CO emission across the entire galactic plane and have derived an overall X factor of  $1.8 \times 10^{20} \text{K}^{-1} \text{km}^{-1} \text{s cm}^{-2}$ .

These CO measurements and the X factor can be used to provide a measure of the molecular hydrogen content along our lines of sight. This information can be combined with the X-ray and 21 cm derived hydrogen column densities in order to diagnose the hydrogen composition. The X-ray derived  $n_{\text{Hx}}$  measures the total column of hydrogen in all forms, while the 21 cm column measures the dominant

Table 3.3. Hydrogen Column Decomposition

	PKS 0745-19 [cm <sup>-2</sup> ]	CIZA 1324 [cm <sup>-2</sup> ]
$n_H$ (21 cm)	$4.24 \times 10^{21}$	$3.81 \times 10^{21}$
$n_{H_2}$ (CO)	$8.02 \times 10^{20}$	$3.09 \times 10^{20}$
equivalent $n_H$ (CO)	$2.29 \times 10^{21}$	$8.81 \times 10^{20}$
$n_H$ (21 cm + CO) <sup>a</sup>	$6.53_{5.9}^{7.2} \times 10^{21}$	$4.69_{4.2}^{5.2} \times 10^{21}$
$n_H$ (X-ray) <sup>b</sup>	$5.6_{5.3}^{5.9} \times 10^{21}$	$6.2_{5.4}^{6.4} \times 10^{21}$

<sup>a</sup>The values in sub and superscript are the upper and lower range of the error region assuming errors of  $\pm 10\%$ .

<sup>b</sup>The values in sub and superscript are the extent of the 90% confidence region from the X-ray spectral fit.

neutral atomic component. The CO measurements can then be used to constrain the proportion of the remaining component that is molecular hydrogen.

PKS 0745-19 and CIZA 1324 are the only clusters in our sample that have spatial coordinates that place them within the bounds of the Dame et al. CO galactic plane survey. We have extracted CO fluxes of 4.46 and 1.72 K km s<sup>-1</sup> for these lines of sight, which can be converted to molecular hydrogen columns ( $n_{H_2}$ ) of  $8.02 \times 10^{20}$  and  $3.09 \times 10^{20}$  cm<sup>-2</sup> using the X factor from Dame et al. . Equivalent hydrogen columns of  $n_H = 2.29 \times 10^{21}$  and  $8.81 \times 10^{20}$  are computed using a factor 2.85 for the conversion of H<sub>2</sub> to  $n_H$  as recommended by Wilms, Allen, & McCray (2000).

Table 3.3 shows the breakdown of the total hydrogen column into its components for the two lines of sight towards PKS 0745-19 and CIZA 1324. The fourth row shows the sum of the 21 cm neutral hydrogen component and the CO derived molecular component, and the fifth row shows the total column derived from the

X-ray observations. The errors on the  $n_H(21\text{ cm} + \text{CO})$  values come from assuming a 10% error. Arabadjis & Bregman (1999) show that the error on the 21 cm data is about 5%; we believe that when combined with the uncertainty in the CO data and the CO to H<sub>2</sub> conversion 10% is a plausible value. The error in the  $n_{H_X}$  value is the 90% confidence interval from the X-ray fit.

The results from these two lines of sight show that the  $n_H(21\text{ cm} + \text{CO})$  and  $n_{H_X}$  values are in fair agreement within the errors. PKS 0745-19 is in better agreement, but even though the error bars on the  $n_{H_X}$  measurement for CIZA 1324 are larger, the numbers still agree to within 25%

Other evidence supports our claim that the excess absorption in the X-ray hydrogen column can be ascribed to H<sub>2</sub>. Federman, Glassgold, & Kwan (1979) show that at the columns where we begin to see  $n_{H_X}$  larger than those measured by 21 cm measurements, H<sub>2</sub> is dense enough to start shielding itself from incident ionizing radiation that dissociates it at lower densities. Also, the *Copernicus* satellite has found that these are the columns at which H<sub>2</sub> starts to become abundant (Savage, Drake, Budich, & Bohlin 1977).

### 3.3.2 Galactic Oxygen Abundance

The main result from this work is the X-ray measurement of the galactic oxygen abundance. Column 6 of Table 3.2 gives our results for the abundance of oxygen using the best fit galactic absorption model. These results are plotted against the X-ray  $n_H$  from column 5 in Figure 3.10.

The galactic oxygen abundance is uniform for all our lines of sight and is centered on the solar value. The best fit value is O/H = 0.90 with a standard deviation of 0.024. Figure 3.10 shows that there is no trend in the oxygen abundance with increasing hydrogen column, and that a single value for the oxygen abundance is a

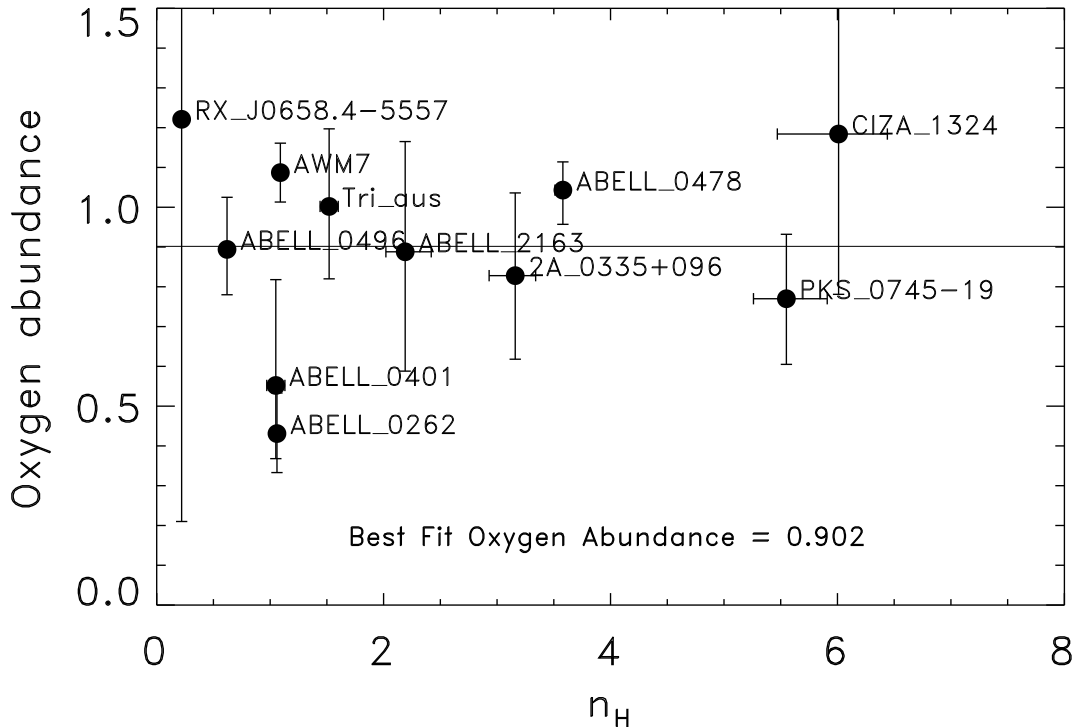


Figure 3.10: The Galactic oxygen abundance plotted against the X-ray hydrogen column for 11 lines of sight towards galaxy clusters. The abundances are given with respect to the solar value in Wilms, Allen, & McCray (2000), and the hydrogen columns are in units of  $10^{21}$  atoms  $\text{cm}^{-2}$ . The best fit value for the oxygen abundance is  $\text{O}/\text{H} = 0.90 \pm 0.024$  solar.

reasonable fit to the individual data points. These results stand in contrast to many years of work on metal depletion in the ISM and support the recent compilation by Jenkins (2003) that shows that oxygen has little depletion in our galaxy.

### 3.3.3 Oxygen Abundance Variations

Is the oxygen we observe in dense clouds or spread out along the line of sight? If in clouds, we would expect a lower abundance because the denser regions of clouds are more amenable to dust formation and depletion of oxygen (Jenkins 1987; Crinklaw, Federman, & Joseph 1994).

In order to try and observe this effect and separate it from the *a priori* expected abundance variations caused by the galactic abundance gradient and galactic hydrogen distribution, we use the Milky Way mass models of Wolfire, McKee, Hollenbach, & Tielens (2003) and the measurements of the spatial gradient of the oxygen abundance measured in planetary nebulae by Henry, Kwitter, & Balick (2004). Our approach is to simply take the Wolfire et al. density model for galactic neutral hydrogen, multiply it by the oxygen abundance in Henry et al. (taking into account the spatial gradient across the galaxy) and integrate outward from the Sun to determine the total hydrogen and oxygen columns. The idea is to get a rough estimate of a global oxygen abundance as a function of position in the sky, so errors in the model<sup>3</sup> are not important unless they substantially change our results. We generate a simple 360 by 180 pixel skymap with pixels spaced every degree in latitude and longitude. The resulting map does give a good idea of the variation of the hydrogen and oxygen columns across the sky given our simple model, even though the pixel spacing and map projection emphasize regions at high latitudes.

The Wolfire et al. model for neutral hydrogen has an exponential falloff with galactic radius for large radii, and a Gaussian distribution in the height above the disk. Also, the center of the galaxy is low in atomic hydrogen, and Wolfire et al. exclude hydrogen from the central part of the galaxy:

$$\Sigma_{\text{H I}}(R) = \begin{cases} 1.4R_k - 0.6 & (3 \leq R_k < 4) \\ 5 & (4 \leq R_k < 8.5) \\ 6.12(R_k/8.5) - 1.12 & (8.5 \leq R_k < 13) \\ 8.24 e^{-(R_k-13)/4} & (13 \leq R_k < 24) \end{cases}$$

where  $\Sigma_{\text{H I}}(R)$  is the H I surface density in  $M_{\odot} \text{pc}^{-2}$ ,  $R_k \equiv R/(1 \text{ kpc})$ , and where

---

<sup>3</sup>e.g., using the Henry et al. gradient that was determined for the galactic plane as a proxy for the oxygen abundance in the halo

we use the conversion  $1 M_{\odot} \text{pc}^{-2} = 1.25 \times 10^{20} \text{ H I cm}^{-2}$ .

The Henry et al. spatial oxygen abundance gradient has the logarithmic abundance going linearly as the galacto-centric radius:

$$\text{O/H}(r) = 10^{(8.97-0.037r)-12.0},$$

where  $\text{O/H}(r)$  is the abundance of oxygen by number with respect to hydrogen as a function of the galactic radius  $r$  in kpc. The Henry et al. results are normalized to the solar oxygen abundance given in Allende Prieto, Lambert, & Asplund (2001)<sup>4</sup> and measure oxygen abundances in planetary nebulae which are consistent with measurements made in H II regions by Deharveng, Peña, Caplan, & Costero (2000).

Figure 3.11 shows the hydrogen column across the sky, the oxygen abundance, and a scatterplot of the oxygen abundance versus the hydrogen column for sightlines across the entire sky. This figure shows that we should expect the hydrogen column and oxygen abundance to be very uniform across most of the sky, except for the region within a few degrees of the galactic plane. This is in agreement with the oxygen results shown in Figure 3.10.

### **Spatial Consistency of the Oxygen Abundance**

In order to check whether this effect is seen in our data observations, we plot the oxygen abundance against the ratio of the X-ray to 21 cm  $n_H$  in Figure 3.12. The ratio of the X-ray to 21 cm derived  $n_H$  stands in for density: we expect that any hydrogen seen in the X-ray but not in the radio is most likely molecular and found in denser clouds. If the denser regions are more depleted than the more diffuse regions, we would expect a downward trend in the plot. However, Figure 3.12 shows that the oxygen abundance shows no trend with the X-ray to 21 cm  $n_H$  ratio, and

---

<sup>4</sup>which is nearly identical to the most recent solar oxygen abundance given in Asplund et al. (2003)

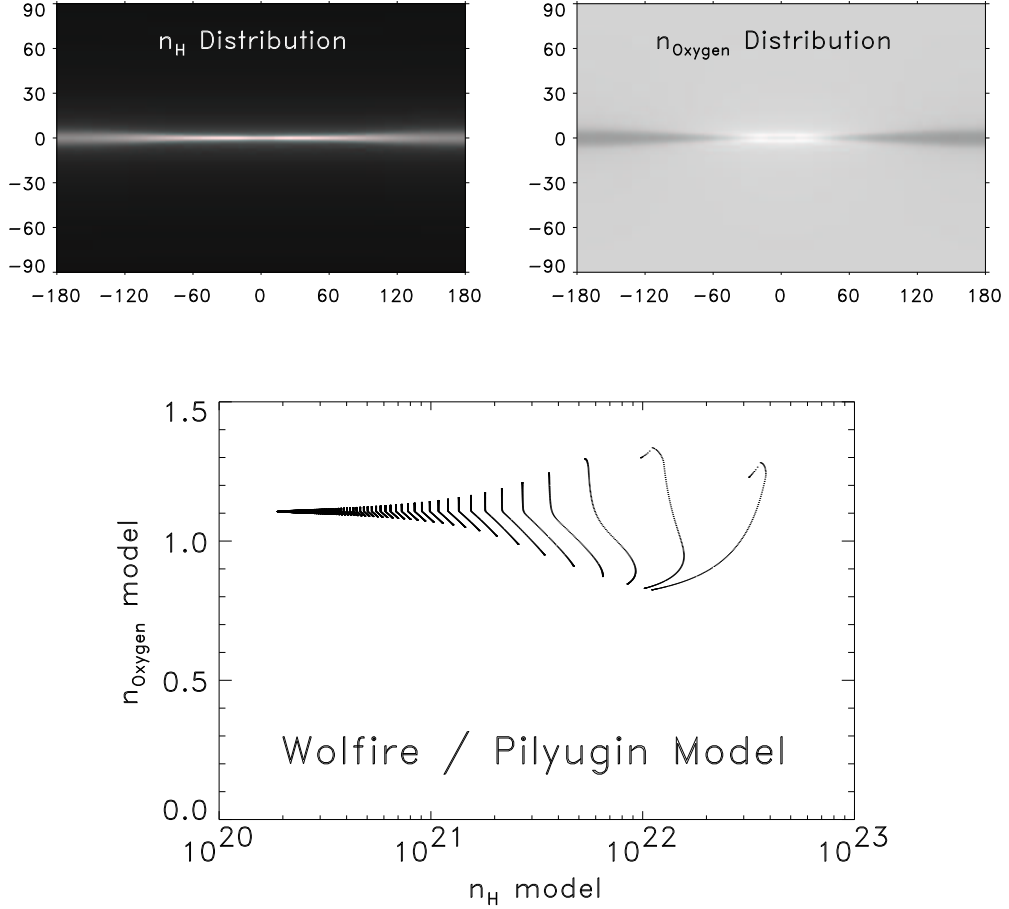


Figure 3.11: The distribution of  $n_H$  and oxygen on the sky as computed by integrating along all lines of sight through a model of the galaxy. The first panel shows the integrated neutral hydrogen column density integrated from the solar position through the galactic density model given by Wolfire, McKee, Hollenbach, & Tielens (2003), the second panel shows the oxygen abundance derived by incorporating the Henry, Kwitter, & Balick (2004) oxygen gradient into the hydrogen model, and the third panel is a scatterplot of the oxygen abundance against the hydrogen column for each location in the skymaps. The oxygen abundance is very uniform across most of the sky, but shows some variation within two degrees of the galactic plane.

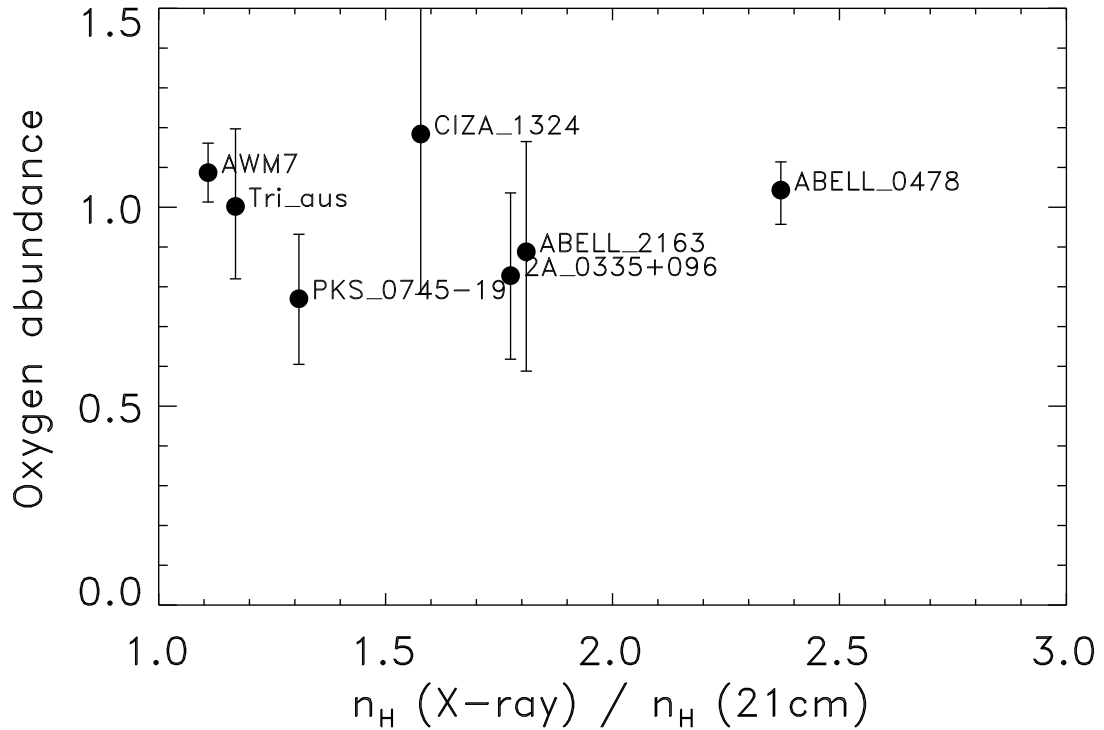


Figure 3.12: A plot showing the constancy of the ISM oxygen abundance with respect to different overdensities of  $n_{H_X}$ . If the high column density lines of sight can be associated with denser molecular clouds, this result indicates that the relative abundance of oxygen in these clouds is not different from its value in other parts of the galaxy.

shows that the galactic oxygen abundance is the same in all regions measured. This disagrees with the STIS observations reported in Cartledge, Meyer, Lauroesch, & Sofia (2001), but agrees with the more recent *FUSE* data of Jensen, Rachford, & Snow (2003). Vuong et al. (2003) also claims with X-ray observations towards Galactic star forming regions that the local diffuse ISM has similar abundances as denser parts of the ISM.

## 3.4 Systematic Errors

The contribution to the uncertainty of our measurements from systematic errors outweighs the statistical uncertainty. The main contributors to the systematic error include the correct determination of the extra edge component in the spectral fits, the galactic helium abundance, and the possible correlation of the measured oxygen abundance with the X-ray hydrogen column.

### 3.4.1 Error in the Extra Edge Determination

In §3.2.3 we measured the size of the extra edge necessary to reconcile the MOS and pn oxygen abundances by looking at high signal to noise data from the bright sources 3C 273 and the Coma cluster and added an extra edge component at oxygen to the mos fits so that they would match the pn. However, it is possible that this method would not completely reconcile the MOS and pn derived abundances for all epochs. If the magnitude of the extra edge component is changing with time (e.g., if there is a progressive buildup of a contaminant in the camera), then we can expect that the extra edge determined from the calibration sources to not accurately reflect the value necessary for each of the cluster observations, which are taken at several different epochs.

Figure 3.13 shows two different ways to check this potential problem. The first panel of Figure 3.13 shows the ISM oxygen abundances that result from running the fits with the magnitude of the extra edge component set to zero. Also, the third panel of Figure 3.13 shows the oxygen abundances found from fitting to only the pn data, which does not require the extra edge component.

We would expect that the fits without the extra edge would show a higher ISM oxygen abundance in order to compensate for the missing extra edge. Panel one

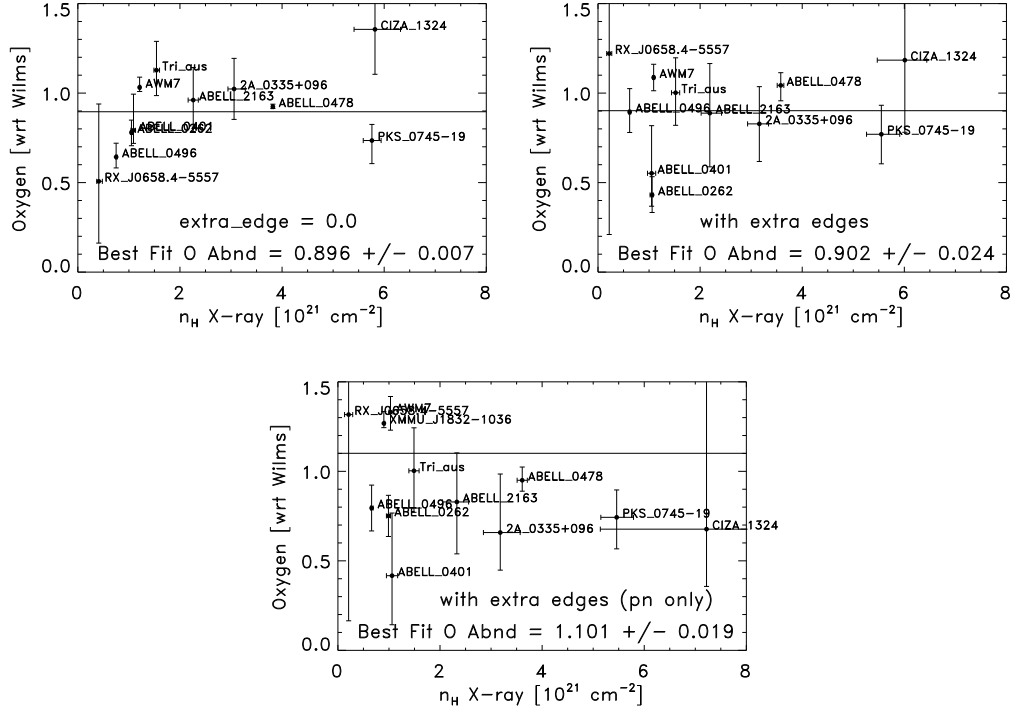


Figure 3.13: A comparison of results fit with and without the extra oxygen edge model component. The first panel shows the results of fitting a model with the extra edge component set to zero. In general, the derived oxygen abundances for the data points with the smallest errors are slightly higher than the fits that include the extra edge (panel 2) because the fit compensates for the extra absorption missing from the instrumental response matrix. The third panel shows the oxygen abundances derived from fits using only data from the pn detector in order to avoid the problems with the MOS detectors. The errors are greater, but the results are consistent with the other two panels. In general, the pn data dominates the fit when data from all three detectors are present because of its greater effective area and larger number of photons. When the MOS data are included without the extra edge component, the extra absorption in the response matrix drives down the derived oxygen abundances at the lowest galactic columns where the fractional contribution of the extra absorption is greatest.

does show that the oxygen abundances for some of the cluster lines of sight are higher without the extra edge than the normal fits in panel two. However, the effect is not large and is greater than the measurement errors for only a few of the lines of sight.

We would also expect the oxygen abundances found from fitting only to the pn data to be lower than those found with all three detectors and the extra edge component in the MOS set to zero. In fact, although the pn only abundances in panel three are slightly lower than abundances without the extra edge in panel one, the difference is small, and only of the same order as the measurement errors. This result, and the similarity of the oxygen abundances found with and without the extra edge, show that we are not sensitive to small errors in the correct determination of the extra edge component for each observation.

### 3.4.2 Helium Abundance Errors

Below the oxygen edge at 542 eV, the absorption due to helium in the ISM dominates the contribution from all other elements. Above the edge oxygen dominates the ISM absorption, but the helium component is still much larger than the hydrogen absorption which is falling off rapidly approximately as  $E^{-3}$ . The galactic helium abundance is somewhat uncertain, and errors in this value could affect our abundance measurements because of its dominant contribution to the ISM X-ray absorption at our energies of interest. If the helium abundance in our model is too low, the hydrogen component will be increased to compensate. This will affect the oxygen abundance, since it is measured with respect to the hydrogen component. If the adopted helium abundance is too high, a similar result occurs, but in the opposite direction.

We have investigated this effect by fitting our data with two different helium

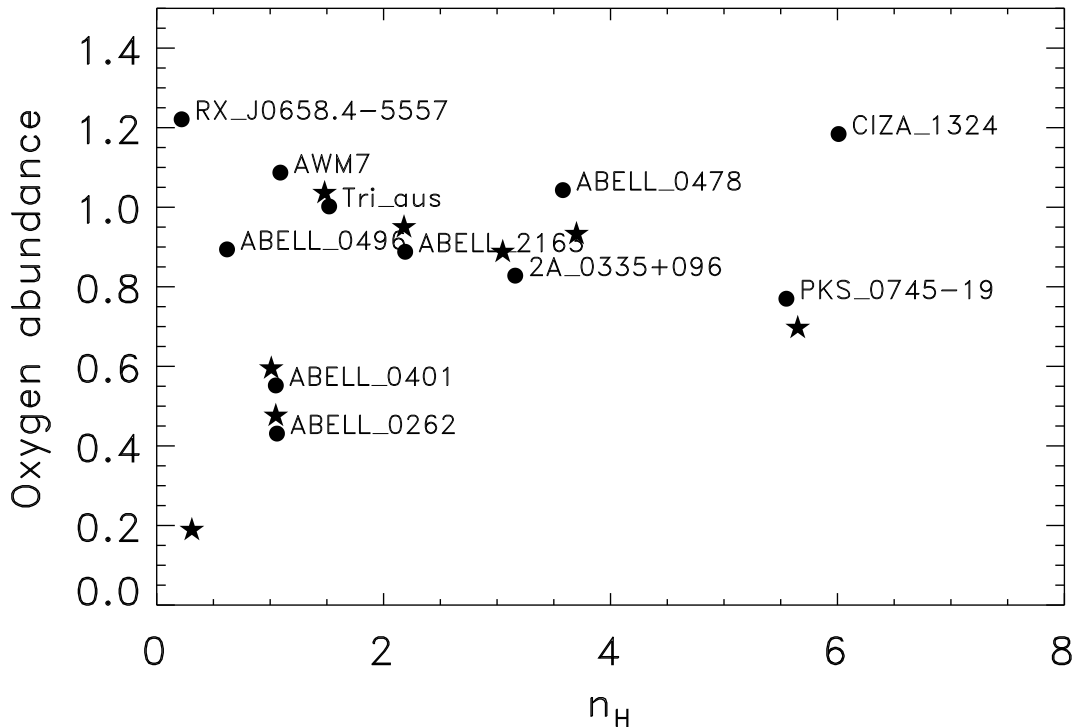


Figure 3.14: A demonstration of the effect of an uncertain helium abundance on oxygen abundance results. The circular points result from a fit to the data using the solar abundances of Wilms, Allen, & McCray (2000). The stars are fit using the solar photospheric abundances of Lodders (2003), which have a substantially lower helium abundance. As expected, the lower solar helium abundance drives up the derived value of  $n_H$  which in turn reduces the normalized oxygen abundance. The effect is noticeable, but much smaller than the errors on the fits (shown in Figure 3.10).

abundances. The first data set is fit with the standard `wilm` abundances in `XSPEC`, and the second set is fit with the `lodd` abundances as implemented in `XSPEC` v.11.3.0. The `wilm` helium abundance is  $9.77 \times 10^{-2}$  by number with respect to hydrogen, and the `lodd` helium abundance is  $7.92 \times 10^{-2}$ , about a 20% difference. Figure 3.14 shows the results from these fits. The points plotted as circles (with the cluster name attached) are from the `lodd` fit, and the stars are from the `wilm` fit. As expected, the lower helium abundance in the `lodd` fit raises the hydrogen abundance found

in the fit and lowers the oxygen abundance. However, the effect is less than 5% in the oxygen abundance, and is much smaller than the scatter between the multiple cluster observations.

### 3.5 Summary

We have used X-ray observations of galaxy clusters to measure the oxygen abundance and total hydrogen column of the ISM. Our measurements of galactic absorption have shown that the X-ray column,  $n_{H_X}$ , is in close agreement with the 21 cm value for neutral hydrogen for columns less than about  $0.5 \times 10^{21} \text{cm}^{-2}$ . Above  $0.5 \times 10^{21} \text{cm}^{-2}$ , the X-ray column is much higher than the 21 cm value by up to a factor of 2.5. This result indicates that there is substantial absorption at high columns in addition to that provided by neutral hydrogen, and is most likely from clouds of molecular hydrogen. Measurements of the contribution to  $n_{H_X}$  from  $\text{H}_2$  derived from CO observations show that the molecular hydrogen column density makes up for the observed difference.

We also measure the ISM oxygen abundance by observing the K-shell photoionization edge at 542 eV. After taking into account calibration problems in the EPIC MOS detectors on *XMM-Newton*, we find that the galactic oxygen abundance is consistent with the most recent solar values. Previously, oxygen abundance measurements have suggested that oxygen is depleted in the ISM because gas phase measurements have shown the abundance to be lower than the adopted solar value. However, the accepted solar value has recently decreased as a result of better modeling of solar spectra (Asplund et al. 2003). Our measurement in conjunction with the recent solar value shows that oxygen is not depleted in the ISM, in agreement with Jenkins (2003). We also find that the oxygen abundance is uniform across

an order of magnitude in  $n_{H_X}$ , suggesting similar compositions for higher density regions in the ISM and more diffuse regions, in agreement with the conclusions of Vuong et al. (2003).

The authors would like to thank H. Ebeling and T. Furusho for sharing their *XMM-Newton* data for CIZA 1324 and AWM 7 before the public release dates, and K. Kuntz for many valuable discussions. This work has made use of data from the High Energy Astrophysics Science Archive Research Center (HEASARC), provided by NASA's Goddard Space Flight Center as well as data from the NASA/IPAC Extragalactic Database (NED) which is operated by the Jet Propulsion Laboratory, California Institute of Technology, under contract with the National Aeronautics and Space Administration.

# Bibliography

- Anders, E. & Grevesse, N. 1989, *Geochim. Cosmochim. Acta*, 53, 197
- Allende Prieto, C., Lambert, D. L., & Asplund, M. 2001, *ApJ*, 556, L63
- André, M. K. et al. 2003, *ApJ*, 591, 1000
- Arabadjis, J. S. & Bregman, J. N. 1999, *ApJ*, 510, 806
- Asplund, M., Grevesse, N., Sauval, A. J., Prieto, C. A., & Kiselman, D. 2003, *ArXiv Astrophysics e-prints*, astro-ph/0312290
- Boulangier, F., Abergel, A., Bernard, J.-P., Burton, W. B., Desert, F.-X., Hartmann, D., Lagache, G., & Puget, J.-L. 1996, *A&A*, 312, 256
- Burstein, D. & Heiles, C. 1982, *AJ*, 87, 1165
- Cardelli, J. A., Sofia, U. J., Savage, B. D., Keenan, F. P., & Dufton, P. L. 1994, *ApJ*, 420, L29
- Cardelli, J. A., Meyer, D. M., Jura, M., & Savage, B. D. 1996, *ApJ*, 467, 334
- Cartledge, S. I. B., Meyer, D. M., Lauroesch, J. T., & Sofia, U. J. 2001, *ApJ*, 562, 394
- de Vries, C. P., den Herder, J. W., Kaastra, J. S., Paerels, F. B., den Boggende, A. J., & Rasmussen, A. P. 2003, *A&A*, 404, 959
- Crinklaw, G., Federman, S. R., & Joseph, C. L. 1994, *ApJ*, 424, 748
- Dame, T. M., Hartmann, D., & Thaddeus, P. 2001, *ApJ*, 547, 792
- Deharveng, L., Peña, M., Caplan, J., & Costero, R. 2000, *MNRAS*, 311, 329

- Dickey, J. M. & Lockman, F. J. 1990, *ARA&A*, 28, 215
- Draine, B. T. 2003, *ArXiv Astrophysics e-prints*, astro-ph/0312592
- Federman, S. R., Glassgold, A. E., & Kwan, J. 1979, *ApJ*, 227, 466
- Fitzpatrick, E. L. 1996, *ApJ*, 473, L55
- Grevesse, N. & Sauval, A. J. 1998, *Space Science Reviews*, 85, 161
- Grevesse, N. & Sauval, A. J. 1999, *A&A*, 347, 348
- Haffner, L. M., Reynolds, R. J., Tufte, S. L., Madsen, G. J., Jaehnig, K. P., & Percival, J. W. 2003, *ApJS*, 149, 405
- Henry, R. B. C., Kwitter, K. B., & Balick, B. 2004, *ArXiv Astrophysics e-prints*, astro-ph/0401156
- Holweger, H. 2001, *AIP Conf. Proc.* 598: Joint SOHO/ACE workshop "Solar and Galactic Composition", 598, 23
- Horner, D. 2001, Ph.D. Dissertation, Department of Astronomy, University of Maryland College Park
- Horner, D. J., Baumgartner, W. H., Gendreau, K. C., & Mushotzky, R. F. 2004, *ApJS*, submitted
- Jenkins, E. B. 1987, *ASSL Vol. 134: Interstellar Processes*, 533
- Jenkins, E. B. 2003, *ArXiv Astrophysics e-prints*, 9651
- Jensen, A. G., Rachford, B. L., & Snow, T. P. 2003, *American Astronomical Society Meeting*, 203,
- Juett, A. M., Schulz, N. S., & Chakrabarty, D. 2003, *ArXiv Astrophysics e-prints*, astro-ph/0312205
- Kuntz, K. D. 2001, Ph.D. Thesis, Department of Astronomy, University of Maryland College Park
- Laor, A., Fiore, F., Elvis, M., Wilkes, B. J., & McDowell, J. C. 1997, *ApJ*, 477, 93
- Lodders, K. 2003, *ApJ*, 591, 1220

- Mathis, J. S. 1996, *ApJ*, 472, 643
- Meyer, D. M., Jura, M., Hawkins, I., & Cardelli, J. A. 1994, *ApJ*, 437, L59
- Moos, H. W. et al. 2002, *ApJS*, 140, 3
- Oliveira, C. M., Hébrard, G., Howk, J. C., Kruk, J. W., Chayer, P., & Moos, H. W. 2003, *ApJ*, 587, 235
- Paerels, F. et al. 2001, *ApJ*, 546, 338
- Page, M. J., Soria, R., Wu, K., Mason, K. O., Cordova, F. A., & Priedhorsky, W. C. 2003, *MNRAS*, 345, 639
- Pilyugin, L. S., Ferrini, F., & Shkvarun, R. V. 2003, *A&A*, 401, 557
- Schlegel, D. J., Finkbeiner, D. P., & Davis, M. 1998, *ApJ*, 500, 525
- Savage, B. D., Drake, J. F., Budich, W., & Bohlin, R. C. 1977, *ApJ*, 216, 291
- Smith, R. K., Brickhouse, N. S., Liedahl, D. A., & Raymond, J. C. 2001, *ApJ*, 556, L91
- Sofia, U. J. & Meyer, D. M. 2001, *ApJ*, 554, L221
- Strasser, S. T. & Taylor, A. R. 2004, *ArXiv Astrophysics e-prints*, astro-ph/0401248
- Verner, D. A., Ferland, G. J., Korista, K. T., & Yakovlev, D. G. 1996, *ApJ*, 465, 487
- Vuong, M. H., Montmerle, T., Grosso, N., Feigelson, E. D., Verstraete, L., & Ozawa, H. 2003, *A&A*, 408, 581
- Weisskopf, M. C., O'Dell, S. L., Paerels, F., Elsner, R. F., Becker, W., Tennant, A. F., & Swartz, D. A. 2004, *ApJ*, 601, 1050
- Willingale, R., Aschenbach, B., Griffiths, R. G., Sembay, S., Warwick, R. S., Becker, W., Abbey, A. F., & Bonnet-Bidaud, J.-M. 2001, *A&A*, 365, L212
- Wilms, J., Allen, A., & McCray, R. 2000, *ApJ*, 542, 914
- Wolfire, M. G., McKee, C. F., Hollenbach, D., & Tielens, A. G. G. M. 2003, *ApJ*, 587, 278

# Chapter 4

## Intermediate Element Abundances in Galaxy Clusters

### Abstract

We present the average abundances of the intermediate elements obtained by performing a stacked analysis of all the galaxy clusters in the archive of the X-ray telescope *ASCA*. We determine the abundances of Fe, Si, S, and Ni as a function of cluster temperature (mass) from 1–10 keV, and place strong upper limits on the abundances of Ca and Ar. In general, Si and Ni are overabundant with respect to Fe, while Ar and Ca are very underabundant. The discrepancy between the abundances of Si, S, Ar, and Ca indicate that the  $\alpha$ -elements do not behave homogeneously as a single group. We show that the abundances of the most well-determined elements Fe, Si, and S in conjunction with recent theoretical supernovae yields do not give a consistent solution for the fraction of material produced by Type Ia and Type II supernovae at any temperature or mass. The general trend is for higher temperature clusters to have more of their metals produced in Type II supernovae than in Type Ias. The inconsistency of our results with abundances in the Milky Way

indicate that spiral galaxies are not the dominant metal contributors to the intra-cluster medium (ICM). The pattern of elemental abundances requires an additional source of metals beyond standard SN Ia and SN II enrichment. The properties of this new source are well matched to those of Type II supernovae with very massive, metal-poor progenitor stars. These results are consistent with a significant fraction of the ICM metals produced by an early generation of population III stars.

## 4.1 Introduction

Galaxy clusters provide an excellent environment for determining the relative abundances of the elements. Because clusters are the largest potential wells known, they retain all the enriched material produced by the member galaxies. This behavior is in stark contrast to our own Milky Way (Timmes, Woosley, & Weaver 1995) and many other individual galaxies (Henry & Worthey 1999). The accumulation of enriched material in clusters can be used as a probe to study the star formation history of the universe, the mechanisms that eject the elements into the ICM, the relative importance of different classes of supernovae, and ultimately the source of the metals in the intra-cluster medium (ICM).

The dominant baryonic component in clusters is the hot gas in the ICM, with 5–10 times as much mass as resides in the stellar component. The physics describing the dominant emission mechanism of the ICM gas is relatively simple. The ICM is optically thin, well modeled by a sphere of hydrostatic gas in thermal equilibrium, and the high temperatures and moderate densities minimize the importance of dust. Extinction, ionization, non-equilibrium and optical depth effects are minimal. As a result, cluster abundance determinations are more physically robust and reliable than those in, e.g., stellar systems, H II regions, and planetary nebulae. The hot

gas emits dominantly by thermal bremsstrahlung in the X-ray band, and the strong transitions to the  $n=1$  level (K-shell) and to the  $n=2$  level (L-shell) of the H-like and He-like ions of the elements from carbon to nickel also lie in the X-ray band. This makes the X-ray band an attractive place for elemental abundance determinations.

Early X-ray observations of galaxy clusters (Mitchell, Culhane, Davison, & Ives 1976; Serlemitsos et al. 1977) showed that the strong H- and He-like iron lines at 6.9 and 6.7 keV could lead to a value for the metal abundance in clusters. Later results (Mushotzky et al. 1978; Mushotzky 1983) derived from iron line observations showed that clusters had metal abundances of about 1/3 the solar value.

The improved spectral resolution and large collecting area of the *ASCA* X-ray telescope brought new power to studies of cluster metal abundances. In particular, the improved 0.5–10.0 keV energy range of *ASCA* allowed for better spectroscopic fits to clusters than was possible with *ROSAT*, which had an upper limit of 2.5 keV. Mushotzky et al. (1996) studied four bright clusters at temperatures such that strong line emission is present, and provided the first measurements of elemental abundances other than iron since the initial results from *Einstein* (Mushotzky et al. 1981; Becker et al. 1979; Rothenflug, Vigroux, Mushotzky, & Holt 1984). Their measurements of silicon, neon and sulfur were interpreted as high abundances of the  $\alpha$ -elements in clusters. This result suggested that type II supernovae (which produce much higher  $\alpha$  element yields than SN Ia) from massive stars are responsible for a significant fraction of the metals in the ICM. (Type Ia supernovae (SN Ia) produce high yields of elements in the iron peak, while Type II supernovae (SN II) produce yields rich in the  $\alpha$  elements Si, S, Ne, and Mg.) Later work by Fukazawa (1997) showed that clusters are more metal enriched in their centers, and that the Si/Fe ratio is about 1.5–2.0 with respect to the solar value. Fukazawa et al. (1998) showed how the silicon abundance was higher in hotter clusters, and confirmed the impor-

tance of SN II in cluster enrichment. More recently, Finoguenov, David, & Ponman (2000), Finoguenov, Arnaud, & David (2001), and Finoguenov et al. (2002) used *ASCA* and *XMM-Newton* data to show that type Ia products dominate in the centers of certain clusters and how type II products are more evenly distributed. The observation by Arnaud et al. (1992) that the metal mass in clusters is correlated with the optical light from early type galaxies and not from spirals is also important in determining the origins of metals in the ICM.

In this paper we use the *ASCA* satellite (Tanaka, Inoue, & Holt 1994) to further constrain the abundances of the intermediate elements. Previous authors referred to the elements Ne, Mg, Si, S, Ca and Ar as  $\alpha$ -elements in order to emphasize their supposed similar formation mechanism; we will refer to the elements observable with X-ray spectroscopy in the *ASCA* band as intermediate elements. This label includes nickel in the group and is preferred since the observations will show that *the  $\alpha$ -elements do not act homogeneously as a single class.*

The large database of over 300 cluster observations makes the *ASCA* satellite well suited for a overall analysis of the intermediate element abundances in galaxy clusters. While it is not possible to obtain accurate abundances of these elements for more than a few individual clusters, we jointly analyze many clusters at a time in several “stacks” in order to obtain the signal necessary for obtaining the abundances. The relatively large field of view of the *ASCA* telescope allows for spectroscopic analysis of the entire spatial extent of all but the closest clusters, and the moderate spectral resolution enables abundance determinations from the K-shell and L-shell lines.

Fukazawa (1997) and other observations of clusters obtained with *Chandra* and *XMM-Newton* have show that abundance gradients are common across the spatial extent of clusters, often with enhanced iron abundances in the cluster centers. These

observations shed valuable light on the source of the metals and help discriminate among the mechanisms that enrich the ICM. DeGrandi (2003)<sup>1</sup> has shown with *BeppoSax* measurements that the centers of clusters (within a radius where the density is 3500 times the critical density) have iron abundances that are enhanced by about 10–20%. These results indicate the importance of a physical mechanism in the very center of clusters that causes an increase in the central metallicity. However, this occurs only at small radii and does not influence average abundance measurements integrated out to large radii where most of the cluster mass resides.

With these cluster elemental abundances, we investigate the source of the metals as a mixture of canonical SN Ia and SN II, and propose alternative sources of metals necessary to match the observations.

## 4.2 The Elements

The strong  $n=2$  to  $n=1$  Ly- $\alpha$  (or K- $\alpha$ ) lines of the elements from C to Ni lie in the X-ray band between 0.1–10.0 keV. These are the largest equivalent width lines in the X-ray spectrum for clusters with temperatures greater than  $\sim 2$  keV, and the most useful for determining elemental abundances. The strength of these lines depends on the abundance of the elements and their ionization balance, which in turn depends on the temperature of the cluster. The deep gravitational potential well of clusters heats the gas and leaves it highly ionized. The gas emits primarily by thermal bremsstrahlung, and for the temperature range of galaxy clusters the ionization balance is such that most elements have a large population of their atoms in the H-like and/or He-like ionization states over most of the cluster volume. Clusters

---

<sup>1</sup>The proceedings of the Ringberg Cluster Conference, (DeGrandi 2003) can be found at: <http://www.xray.mpe.mpg.de/~ringberg03/>

are optically thin and nearly isothermal, with the result that the line emission is easily interpreted without complicating factors such as radiative transport and the imprint of non-thermal emission.

While all the elements from carbon to nickel have their main lines in the X-ray band, not all of them are easily visible. Elements like fluorine and sodium have abundances more than an order of magnitude below the more abundant elements such as silicon and sulfur, and are so far not detected in observations of galaxy clusters. The list below introduces the more abundant and important elements, and the prospects for measuring their X-ray lines with *ASCA* in galaxy clusters.

### 4.2.1 Carbon, Nitrogen and Oxygen

Low temperature clusters and groups may have nitrogen and carbon K- $\alpha$  lines with significant equivalent width. However, these lines lie below the usable bandpass of the *ASCA* detectors.

H-like oxygen has strong lines at 0.65 keV and is an important element for constraining enrichment scenarios because it is produced predominantly by type II supernovae. However, the response of the *ASCA* GIS detector is uncertain at these energies, and the efficiency of the SIS detector varies with time at low energies and is also relatively uncertain. Unfortunately, the usable bandpass we adopt for *ASCA* does not go low enough to include oxygen.

### 4.2.2 Neon and Magnesium

The K- $\alpha_1$  H-like line for neon is at 1.02 keV and falls right in the middle of the iron L-shell complex ranging from about 0.8–1.4 keV. The resolution of *ASCA* and the close spacing of the iron lines makes neon abundance determinations from the K-shell unreliable.

With its K-shell lines also lying in the iron L-shell complex (1.47 keV), magnesium suffers from the same problems as neon and is not well determined with *ASCA* data. At lower temperatures, the iron L-shell peak is very sensitive to temperature. Our analysis method of stacking together several clusters from a one keV wide bin does not allow us to constrain the temperature well enough to obtain accurate magnesium abundances. At higher temperatures, the lines are not excited enough to produce lines with sufficient equivalent width for abundance determination.

Also, results for both neon and magnesium from the high resolution RGS on *XMM-Newton* show that the CCD abundances do not match those obtained with higher resolution gratings (Sakelliou et al. 2002), indicating that CCD abundances such as those obtained from *ASCA* are not capable of giving acceptable results.

### 4.2.3 Aluminum

Aluminum has a higher solar abundance than calcium and argon (the two lowest abundance elements considered in this paper), but its H-like  $K_\alpha$  line is blended with the much stronger silicon He-like  $K_\alpha$  line and is not reliably measurable.

### 4.2.4 Silicon and Sulfur

After iron, the silicon abundance is the next most well-determined of all the elements. Its H-like  $K-\alpha_1$  line at 2.00 keV and He-like lines at 1.86 keV lie in a relatively uncrowded part of the spectrum, and silicon's large equivalent width leads to a well determined abundance.

Next to Fe and Si, the high natural abundance of sulfur and its position in an uncrowded part of the X-ray spectrum make it a well determined element. Its  $K-\alpha_1$  H-like line is at 2.62 keV.

### 4.2.5 Argon and Calcium

The natural abundance of argon is down almost an order of magnitude from sulfur, giving it a lower equivalent width. However, the K- $\alpha_1$  H-like line at 3.32 keV is in a clear part of the spectrum and measurable.

Calcium is similar to Ar, with a K- $\alpha_1$  H-like line at 4.10 keV.

### 4.2.6 Iron and Nickel

Iron has the strongest set of lines observable in the X-ray spectrum. High temperature clusters above 3 keV primarily have as their strongest lines the K- $\alpha$  set at about 6.97 and 6.67 keV for H-like and He-like iron, while lower temperature clusters excite the L-shell complex of many lines between about 0.6 and 2.0 keV. Hwang et al. (1999) have shown that *ASCA* determinations of iron abundances from just the L or K-shells give consistent results. Iron and nickel are predominantly produced by SNIa.

Like iron, nickel also has L-shell lines that lie in the X-ray band. But unlike iron, the abundance determinations are driven almost entirely by the He-like and H-like K-shell lines at 7.77 and 8.10 keV. This is because the abundance of nickel is about an order of magnitude less than iron, and the nickel L-shell lines are blended with iron's. Nickel abundances using the H-like and He-like lines are most reliable for temperatures above  $\sim 4$  keV since there is little excitation of the K-shell line below this energy.

### 4.3 Solar Abundances

There has been some controversy in the literature as to the canonical values to use for the solar elemental abundances. The values for the elemental abundances by number that are found by spectral fitting to cluster data do not depend on the chosen values for the solar abundances. However, for the sake of convenience elemental abundances are often reported with respect to the solar values.

Mushotzky et al. (1996) in their paper report cluster abundances with respect to the photospheric values in Anders & Grevesse (1989). In Anders & Grevesse (1989), the authors comment on how the photospheric and meteoritic values for the solar abundances were coming into agreement with better measurement techniques and improved values of physical constants, and give numbers for both the photospheric and meteoritic values. While almost all the elements were in good agreement, the iron abundance still showed discrepancies between the photospheric and meteoritic values. Ishimaru & Arimoto (1997) questioned the claims in Mushotzky et al. (1996) by noticing that they used the photospheric values when analyzing the data (the default in *XSPEC* then and now), but that the theoretical results they were comparing to used the meteoritic abundances. Since the discrepancy in the two values for iron was significant, and because many of the abundance ratios used in the analysis were with respect to iron, the conclusions were based on incompatible iron data.

Since 1989, the situation has improved. Reanalysis of the stellar photospheric data for iron that includes lines from Fe II in addition to Fe I as well as improved modeling of the solar lines (Grevesse & Sauval 1999) have brought the meteoritic and photospheric values into agreement. Grevesse & Sauval (1998) incorporate these changes and others and has become a *de facto* standard for the standard solar composition. Table 4.1) gives the abundances from both sources.

Table 4.1. Solar Abundances

Element	Anders & Grevesse (1989) <sup>a</sup>	Grevesse & Sauval (1998) <sup>b</sup>
H	12.00	12.000
C	8.56	8.520
N	8.05	7.920
O	8.93	8.690
Ne	8.09	8.080
Mg	7.58	7.580
Si	7.55	7.555
S	7.21	7.265
Ar	6.56	6.400
Ca	6.36	6.355
Fe	7.67	7.500
Ni	6.25	6.250

References. — (1) Anders & Grevesse 1989; (2) Grevesse & Sauval 1998.

Note. — Abundances are given on a logarithmic scale where H is 12.0.

<sup>a</sup>These numbers are the photospheric values, used as the default in `XSPEC`.

<sup>b</sup>These numbers are a straight average of the photospheric and meteoritic values (except for oxygen, which has the updated value given in Allende Prieto, Lambert, & Asplund 2001).

However, the past history of changes in the adopted solar composition implies that there might still be changes in the abundance values for some elements. Because of this, and the problems of comparing results produced with different, incompatible solar values, we quote our results for the elemental abundances by number with respect to hydrogen. We also give the abundances with respect to the Anders & Grevesse (1989) solar abundances to ease comparisons with previous works, and

in addition list our results with respect to the standard Grevesse & Sauval (1998) values for convenience and for constructing abundance ratios.

## 4.4 Observations and Data Reduction

### 4.4.1 Sample Selection

We use for our sample all the cluster observations in the archives of the *ASCA* satellite. In Horner et al. (ApJS submitted)<sup>2</sup> (hereafter ACC for *ASCA* Cluster Catalog), we describe our efforts to prepare a large catalog of homogeneously analyzed cluster temperatures, luminosities and overall metal abundances from the *rev2* processing of the *ASCA* cluster observations. There we give the full details of the data selection and reduction; only a brief summary is given here. In this paper we use the ACC sample, but our focus is the determination of the abundances for individual elements in addition to iron.

The *ASCA* satellite was launched in February 1993, and ceased scientific observations in July 2000. Over the course of its lifetime it observed 434 clusters in 564 observations. The cluster sample prepared in ACC selects 273 clusters based on the suitability of the data for spectral analysis by removing clusters with too few photons to form an analyzable spectrum, clusters dominated by AGN emission, etc, and is the largest catalog of cluster temperatures, luminosities, and abundances. However, because the catalog was designed to maximize the number of clusters obtained from the *ASCA* archives, it is not necessarily complete to any flux or redshift and could be biased because of the particular selections of the individual *ASCA* observers who originally obtained the data.

---

<sup>2</sup>The results in Horner et al. (ApJS submitted) are primarily from Don Horner's Ph.D. dissertation (Horner 2001), found online at: <http://sol.stsci.edu/~horner>

The cluster extraction regions in the ACC sample were selected to contain as much flux as possible in order to best represent the total emission of the cluster. Radial profiles of the GIS image were made and the spectral extraction regions extended out to the point where the cluster emission was  $5\sigma$  times the background level. Standard processing was applied to the event files (see ACC). For the GIS detector, we used the standard RMF and generated an ARF file for each cluster. For the SIS detector, we generated RMFs for each chip and an overall ARF for each cluster. Backgrounds for the GIS were taken from the HEASARC blank sky fields except for low galactic latitude sources ( $|b| < 20^\circ$ ) where local backgrounds were used. For the SIS, local backgrounds were used unless the cluster emission filled the field of view. In ACC, clusters with more than one observation had their spectral files combined before analysis; the joint fitting procedure described below allows us to deal with multiple observations without a problem.

#### 4.4.2 Stacking Analysis

Only the very few brightest cluster observations in the *ASCA* archives have enough signal to noise to allow spectral fitting of the intermediate elements. In order to improve our sensitivity to these elements, we jointly fit a large number of clusters simultaneously. We divide the 353 observations (of 273 clusters) in the ACC into fitting groups called stacks by placing together clusters with similar temperatures and overall abundances (see Figure 4.2). Not only does this allow us to increase our signal to noise level, but also decreases our susceptibility to systematic errors resulting from inaccuracies in the instrument calibration. Because clusters with different redshifts (but similar temperatures) are analyzed jointly, any energy-localized error in the instrument calibration will have less effect on abundance determination because the error is not likely to affect all the clusters in a single stack. This method

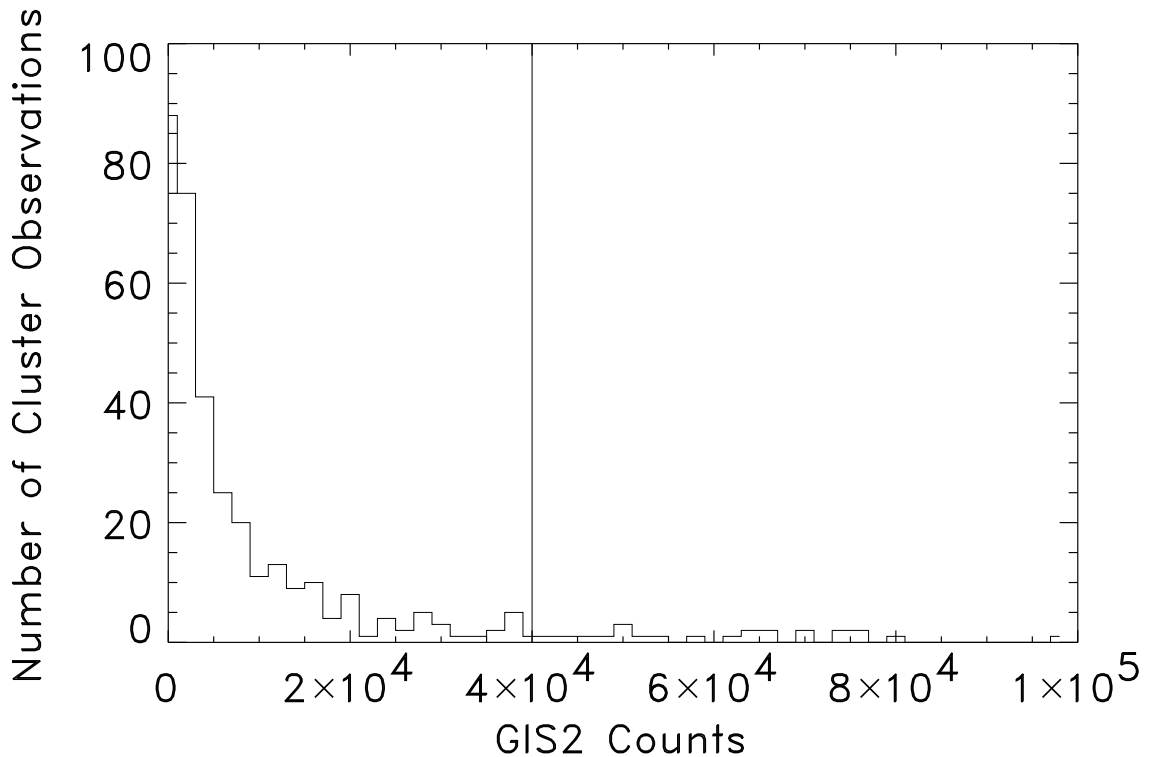


Figure 4.1: Counts per cluster histogram. We excluded clusters with more than 40k counts in the GIS2 detector from our analysis so that very bright clusters do not unduly bias the joint spectral fitting results. The vertical line shows the sample cut. There are only 25 cluster observations excluded from the analysis because they have too many counts.

of analysis also smoothes over biases that may result from the different physical conditions found in clusters (e.g., substructure and eccentricity).

Clusters with more than 40k counts in GIS2 were not included in our analysis so that very bright clusters do not unduly bias the results for a particular stack. Figure 4.1 shows a histogram of the number of counts per cluster observation, and indicates that we only lose 25 data sets by excluding observations with more than 40k counts.

The number of stacks was motivated by our desire to have a reasonable number of stacks covering the 1–10 keV temperature range, and by the limitations of the

Table 4.2. Stack Parameters

Stack Name	Temperature Bin (keV)	Number of Clusters	Total Counts
A	0.5	17	50802
B	1.5	44	228685
C	2.5	35	261267
D	3.5	47	478274
E	4.5	38	277014
F	5.5	37	391047
G	6.5	39	261484
H	7.5	20	111593
I	8.5	14	93481
J	9.5	13	171669
K	10.5	22	135321

*XSPEC* fitting program (jointly fitting more than about 20 clusters with a variable abundance model exceeds the number of free parameters allowed). We divide the clusters into 22 stacks by first separating them into one keV bins (0–1 keV, 1–2 keV, ..., 9–10 keV, 10+ keV), and then dividing each one keV bin into a high and low abundance stack using the iron abundances from ACC. The split between high and low abundance was made such that there are roughly an equal number of clusters in the high and low stack for each one keV bin. In the case where there are more clusters in a stack than it is possible to jointly fit, we divide the stack in two and recombine the results for each sub-stack after fitting. Table 4.2 and Figure 4.2 show the number of clusters in each stack and the dividing line between high and low abundance stacks, as well as how the stacks fill the abundance–temperature plane.

We jointly fit the clusters in each stack to a variable abundance model modified by galactic absorption (*tbabs\*vappec* (Wilms, Allen, & McCray 2000; Smith et al. 2001) within *XSPEC*). The *vappec* model uses the line lists of the APEC code to generate a plasma model with variable abundances for He, C, N, O, Ne, Mg, Al, Si, S,

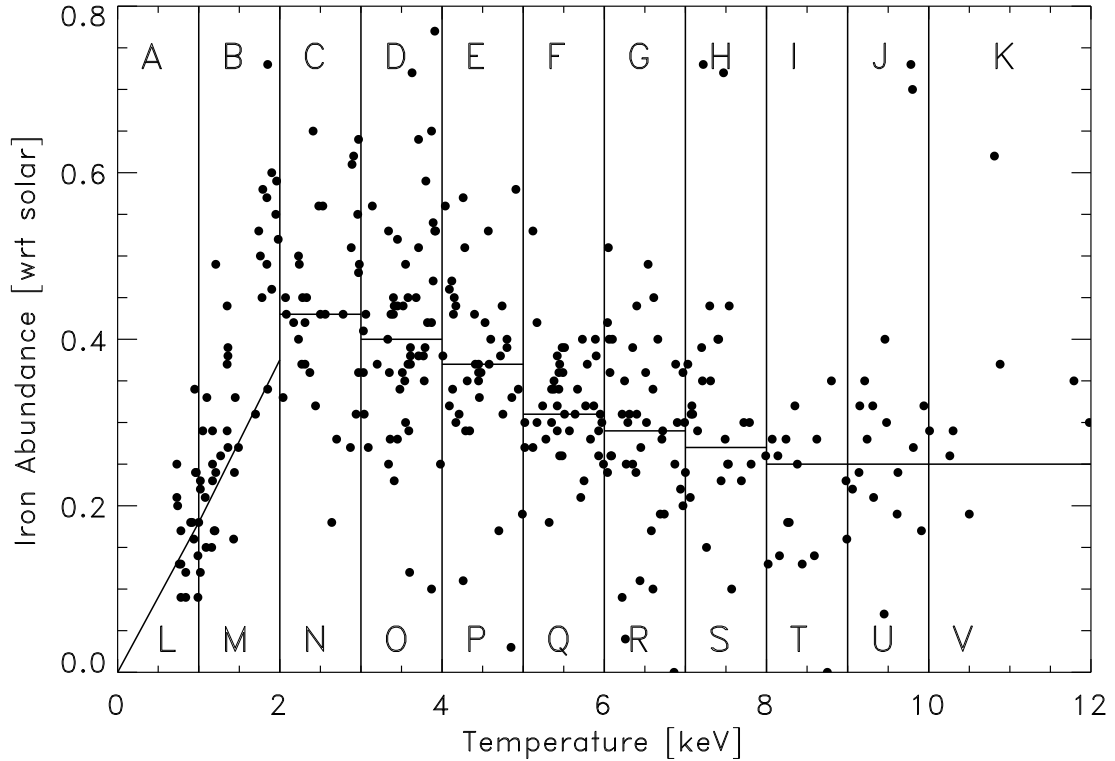


Figure 4.2: Stack selection diagram. The lines on this abundance–temperature plot show where the boundaries were placed for the individual stacks. Each point is a single cluster measurement from ACC. Stacks A through V were fit individually in *XSPEC*, and the results from the low and high abundance stacks were combined into a single result for each one-keV bin (e.g., stack A combined with stack L, etc.).

Ar, Ca, Fe, and Ni. We fixed He, C, N, O, and Al at their solar values and allowed the other elements to vary independently (except for Ne and Mg, which we tied together). After separately extracting each detector, we combine the two GIS data sets and the two SIS data sets together before fitting. The redshift for each cluster was fixed to the optical value found in the literature, except for the few clusters without published optical data (which we allowed to vary [see ACC]). The column density was fixed at the galactic value for the GIS detectors, but allowed to float for the SIS detectors in order to compensate for a varying low energy efficiency problem

(Yaqoob et al. 2000)<sup>3</sup>. The data for most clusters was fit between 0.8–10.0 keV in the GIS and 0.6–10.0 keV in the SIS. Observations made after 1998 had a higher SIS low energy bound of 0.8 keV because of the low energy efficiency problem, and about 10 other clusters had modified energy ranges because of problems with the particular observation (see ACC).

After fitting each of the 22 stacks, we combined the results from the low and high metallicity stacks in the same temperature range in order to further improve the statistics. The difference in the several elemental abundances between the low and high metallicity stacks was consistent with an overall higher or lower metallicity (i.e., the low metallicity stacks L–M have slighter lower Fe, Si, S, and Ni than the high metallicity stacks A–K). For example, stack A (the 0–1 keV high metallicity stack) was combined with stack L (the 0–1 keV low metallicity stack) into a new stack A. These final results for 11 stacks are given in the next section.

## 4.5 Results for Individual Elements

We present results for the abundance of the elements Fe, Si, S, Ar, Ca, and Ni as a function of cluster temperature. Other elements with lines present in cluster X-ray spectra (e.g., Ne, Mg and O) have statistical or systematic errors too large to allow meaningful results. The main results of our analysis are presented in Table 4.3 which lists the metal abundances of the cluster stacks. These results are given by number with respect to hydrogen. In Table 4.4 we give the same results with respect to the photospheric solar abundances in Anders & Grevesse (1989) in order to allow easy comparison with other results in the literature. Finally, in Table 4.5 we give

---

<sup>3</sup>ASCA GOF Calibration Memo (ASCA-CAL-00-06-01, v1.0 06/05/00) (Yaqoob et al. 2000) can be found at: <http://heasarc/docs/asca/calibration/nhparam.html>

Table 4.3. Galaxy Cluster Elemental Abundances by Number

Temperature Bin (keV)	kT <sup>a</sup> (keV)	Silicon <sup>b</sup>	Sulfur <sup>b</sup>	Argon <sup>b</sup>	Calcium <sup>b</sup>	Iron <sup>b</sup>	Nickel <sup>b</sup>
0.5	0.83 <sup>0.84</sup> <sub>0.82</sub>	95.8 <sup>107.9</sup> <sub>84.4</sub>	107.9 <sup>122.0</sup> <sub>94.7</sub>	154.8 <sup>177.5</sup> <sub>134.4</sub>	263.1 <sup>305.0</sup> <sub>224.0</sub>	102.0 <sup>107.1</sup> <sub>96.8</sub>	0.1 <sup>1.3</sup> <sub>0.0</sub>
1.5	1.14 <sup>1.14</sup> <sub>1.13</sub>	132.3 <sup>138.4</sup> <sub>125.6</sub>	71.7 <sup>76.1</sup> <sub>67.1</sub>	39.2 <sup>43.2</sup> <sub>35.3</sub>	52.8 <sup>58.0</sup> <sub>47.6</sub>	135.6 <sup>138.9</sup> <sub>132.4</sub>	2.6 <sup>4.1</sup> <sub>0.4</sub>
2.5	2.58 <sup>2.60</sup> <sub>2.56</sub>	163.9 <sup>183.1</sup> <sub>146.2</sub>	51.6 <sup>60.0</sup> <sub>43.3</sub>	1.0 <sup>4.7</sup> <sub>0.5</sub>	7.4 <sup>10.9</sup> <sub>4.9</sub>	220.8 <sup>228.7</sup> <sub>213.8</sub>	9.7 <sup>13.4</sup> <sub>7.3</sub>
3.5	3.68 <sup>3.70</sup> <sub>3.65</sub>	206.1 <sup>225.3</sup> <sub>188.1</sub>	42.0 <sup>51.2</sup> <sub>33.1</sub>	0.2 <sup>2.5</sup> <sub>0.0</sub>	1.1 <sup>3.5</sup> <sub>0.0</sub>	200.7 <sup>205.8</sup> <sub>196.4</sub>	20.0 <sup>23.4</sup> <sub>16.8</sub>
4.5	4.57 <sup>4.61</sup> <sub>4.54</sub>	197.6 <sup>233.1</sup> <sub>173.1</sub>	34.2 <sup>50.3</sup> <sub>20.4</sub>	0.0 <sup>3.7</sup> <sub>0.0</sub>	0.0 <sup>2.3</sup> <sub>0.0</sub>	127.7 <sup>131.4</sup> <sub>121.6</sub>	16.4 <sup>19.7</sup> <sub>11.9</sub>
5.5	5.77 <sup>5.82</sup> <sub>5.72</sub>	239.9 <sup>273.6</sup> <sub>209.0</sub>	16.2 <sup>32.8</sup> <sub>12.8</sub>	0.0 <sup>2.5</sup> <sub>0.0</sub>	0.0 <sup>1.8</sup> <sub>0.0</sub>	137.0 <sup>141.3</sup> <sub>132.4</sub>	24.5 <sup>28.6</sup> <sub>20.5</sub>
6.5	6.71 <sup>6.78</sup> <sub>6.64</sub>	212.5 <sup>254.0</sup> <sub>182.7</sub>	26.9 <sup>47.7</sup> <sub>23.4</sub>	0.0 <sup>5.0</sup> <sub>0.0</sub>	0.0 <sup>1.6</sup> <sub>0.0</sub>	88.9 <sup>92.6</sup> <sub>85.1</sub>	16.0 <sup>19.9</sup> <sub>12.4</sub>
7.5	7.45 <sup>7.60</sup> <sub>7.32</sub>	158.6 <sup>229.6</sup> <sub>100.4</sub>	51.2 <sup>84.2</sup> <sub>21.9</sub>	0.0 <sup>8.4</sup> <sub>0.0</sub>	0.0 <sup>4.5</sup> <sub>0.0</sub>	92.1 <sup>99.2</sup> <sub>85.6</sub>	23.2 <sup>29.8</sup> <sub>16.8</sub>
8.5	8.30 <sup>8.50</sup> <sub>8.12</sub>	289.9 <sup>388.2</sup> <sub>200.8</sub>	66.2 <sup>114.5</sup> <sub>20.1</sub>	2.0 <sup>25.6</sup> <sub>0.0</sub>	1.1 <sup>10.2</sup> <sub>0.0</sub>	74.8 <sup>82.8</sup> <sub>66.4</sub>	21.8 <sup>29.6</sup> <sub>14.0</sub>
9.5	9.63 <sup>9.80</sup> <sub>9.47</sub>	364.0 <sup>446.4</sup> <sub>285.3</sub>	52.2 <sup>92.8</sup> <sub>24.5</sub>	0.3 <sup>7.5</sup> <sub>0.0</sub>	0.0 <sup>4.4</sup> <sub>0.0</sub>	106.2 <sup>113.7</sup> <sub>98.7</sub>	25.8 <sup>32.9</sup> <sub>18.7</sub>
10.5	10.92 <sup>11.19</sup> <sub>10.69</sub>	298.0 <sup>405.9</sup> <sub>198.7</sub>	64.2 <sup>113.0</sup> <sub>26.1</sub>	0.0 <sup>12.4</sup> <sub>0.0</sub>	0.0 <sup>5.8</sup> <sub>0.0</sub>	85.1 <sup>93.5</sup> <sub>76.7</sub>	21.3 <sup>28.9</sup> <sub>13.6</sub>

<sup>a</sup>The values in the temperature column are the fitted temperature of the simultaneously fit clusters in this temperature bin.

<sup>b</sup>All abundances are  $1 \times 10^7$  times the number of atoms per hydrogen atom.

Note. — The numbers in the sub and superscripts for the abundances are the low and high extent of the 90% confidence region for that element.

Table 4.4. Classical Galaxy Cluster Elemental Abundances<sup>a</sup>

Stack Name	Temperature Bin	Silicon <sup>a</sup>	Sulfur <sup>a</sup>	Argon <sup>a</sup>	Calcium <sup>a</sup>	Iron <sup>a</sup>	Nickel <sup>a</sup>
A	0.5	0.27 <sup>0.30</sup> <sub>0.24</sub>	0.67 <sup>0.75</sup> <sub>0.58</sub>	4.26 <sup>4.89</sup> <sub>3.70</sub>	11.48 <sup>13.31</sup> <sub>9.78</sub>	0.22 <sup>0.23</sup> <sub>0.21</sub>	0.01 <sup>0.07</sup> <sub>0.00</sub>
B	1.5	0.37 <sup>0.39</sup> <sub>0.35</sub>	0.44 <sup>0.47</sup> <sub>0.41</sub>	1.08 <sup>1.19</sup> <sub>0.97</sub>	2.30 <sup>2.53</sup> <sub>2.08</sub>	0.29 <sup>0.30</sup> <sub>0.28</sub>	0.14 <sup>0.23</sup> <sub>0.02</sub>
C	2.5	0.46 <sup>0.52</sup> <sub>0.41</sub>	0.32 <sup>0.37</sup> <sub>0.27</sub>	0.03 <sup>0.13</sup> <sub>0.01</sub>	0.32 <sup>0.48</sup> <sub>0.21</sub>	0.47 <sup>0.49</sup> <sub>0.46</sub>	0.54 <sup>0.75</sup> <sub>0.41</sub>
D	3.5	0.58 <sup>0.64</sup> <sub>0.53</sub>	0.26 <sup>0.32</sup> <sub>0.20</sub>	0.01 <sup>0.07</sup> <sub>0.00</sub>	0.05 <sup>0.15</sup> <sub>0.00</sub>	0.43 <sup>0.44</sup> <sub>0.42</sub>	1.13 <sup>1.32</sup> <sub>0.94</sub>
E	4.5	0.56 <sup>0.66</sup> <sub>0.49</sub>	0.21 <sup>0.31</sup> <sub>0.13</sub>	0.00 <sup>0.10</sup> <sub>0.00</sub>	0.00 <sup>0.10</sup> <sub>0.00</sub>	0.27 <sup>0.28</sup> <sub>0.26</sub>	0.92 <sup>1.11</sup> <sub>0.67</sub>
F	5.5	0.68 <sup>0.77</sup> <sub>0.59</sub>	0.10 <sup>0.20</sup> <sub>0.08</sub>	0.00 <sup>0.07</sup> <sub>0.00</sub>	0.00 <sup>0.08</sup> <sub>0.00</sub>	0.29 <sup>0.30</sup> <sub>0.28</sub>	1.38 <sup>1.61</sup> <sub>1.15</sub>
G	6.5	0.60 <sup>0.72</sup> <sub>0.52</sub>	0.17 <sup>0.29</sup> <sub>0.14</sub>	0.00 <sup>0.14</sup> <sub>0.00</sub>	0.00 <sup>0.07</sup> <sub>0.00</sub>	0.19 <sup>0.20</sup> <sub>0.18</sub>	0.90 <sup>1.12</sup> <sub>0.70</sub>
H	7.5	0.45 <sup>0.65</sup> <sub>0.28</sub>	0.32 <sup>0.52</sup> <sub>0.14</sub>	0.00 <sup>0.23</sup> <sub>0.00</sub>	0.00 <sup>0.20</sup> <sub>0.00</sub>	0.20 <sup>0.21</sup> <sub>0.18</sub>	1.31 <sup>1.68</sup> <sub>0.95</sub>
I	8.5	0.82 <sup>1.09</sup> <sub>0.57</sub>	0.41 <sup>0.71</sup> <sub>0.12</sub>	0.06 <sup>0.70</sup> <sub>0.00</sub>	0.05 <sup>0.45</sup> <sub>0.00</sub>	0.16 <sup>0.18</sup> <sub>0.14</sub>	1.23 <sup>1.67</sup> <sub>0.79</sub>
J	9.5	1.03 <sup>1.26</sup> <sub>0.80</sub>	0.32 <sup>0.57</sup> <sub>0.15</sub>	0.01 <sup>0.21</sup> <sub>0.00</sub>	0.00 <sup>0.19</sup> <sub>0.00</sub>	0.23 <sup>0.24</sup> <sub>0.21</sub>	1.45 <sup>1.85</sup> <sub>1.05</sub>
K	10.5	0.84 <sup>1.14</sup> <sub>0.56</sub>	0.40 <sup>0.70</sup> <sub>0.16</sub>	0.00 <sup>0.34</sup> <sub>0.00</sub>	0.00 <sup>0.25</sup> <sub>0.00</sub>	0.18 <sup>0.20</sup> <sub>0.16</sub>	1.20 <sup>1.62</sup> <sub>0.76</sub>

<sup>a</sup>All abundances are with respect to the solar photosphere elemental abundances given in Anders & Grevesse 1989.

Note. — The numbers in the sub and superscripts for the abundances are the low and high extent of the 90% confidence region for that element.

the cluster abundances with respect to the standard solar composition given in our Table 4.1 adopted from Grevesse & Sauval (1998).

Figure 4.3 displays the same information as in Table 4.5, but in graphical form. Several interesting points are immediately apparent in the data. First, the results for iron closely follow previous results for cluster metallicities, but have much smaller error bars. The actual numerical result for the iron abundance is consistent with the previous results of about 1/3 solar, but the improved quality of the data allows the detection of trends in the iron abundance with temperature: at high temperatures

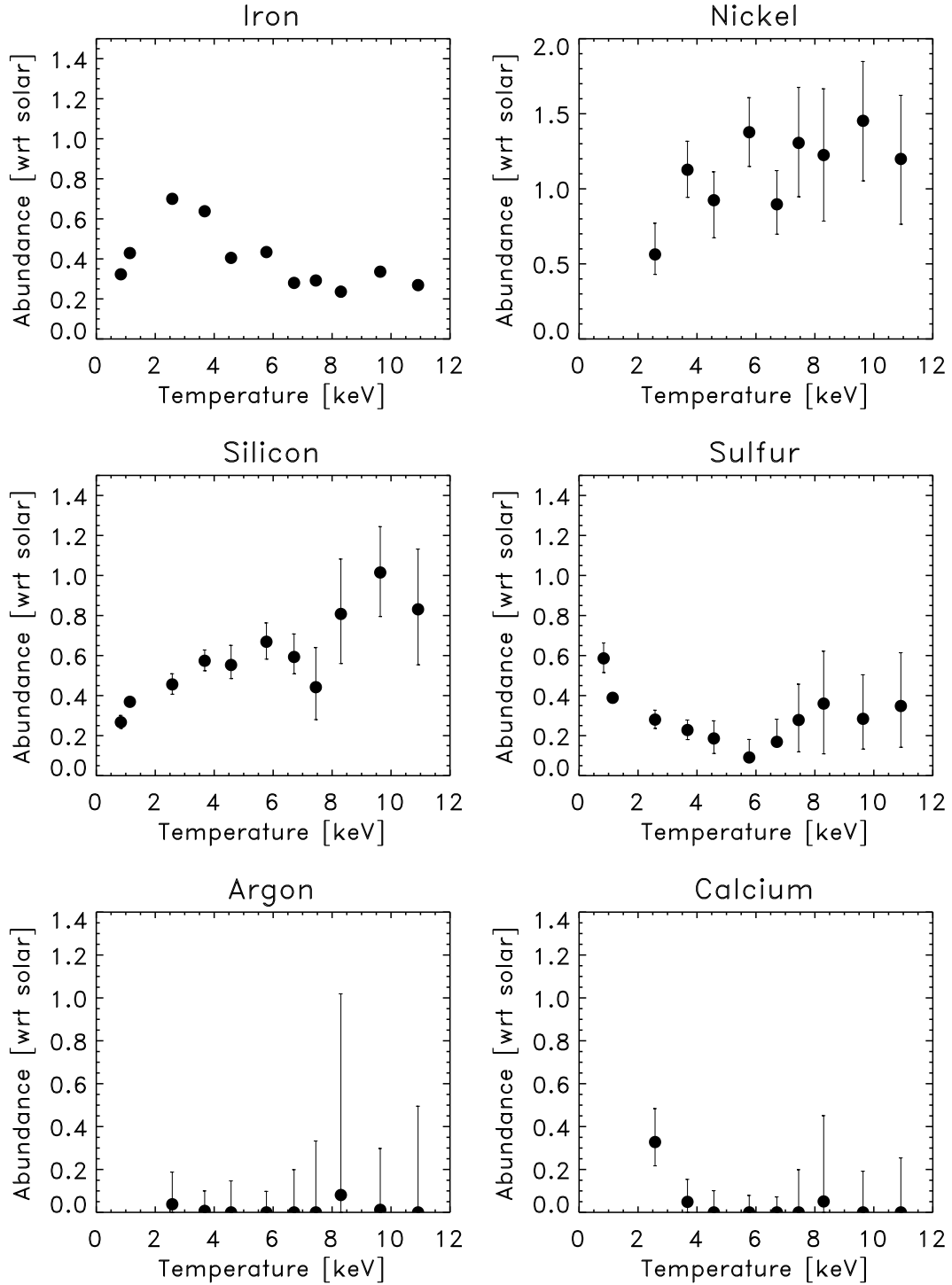


Figure 4.3: The galaxy cluster elemental abundances as a function of temperature. These abundances are with respect to the solar abundances of Grevesse & Sauval (1998). The error bars are the 90% confidence interval for that elemental abundance; the error bars for iron are smaller than the plotted points.

Table 4.5. Current Galaxy Cluster Elemental Abundances<sup>a</sup>

Stack Name	Temperature Bin	Silicon <sup>a</sup>	Sulfur <sup>a</sup>	Argon <sup>a</sup>	Calcium <sup>a</sup>	Iron <sup>a</sup>	Nickel <sup>a</sup>
A	0.5	0.27 <sup>0.30</sup> <sub>0.24</sub>	0.59 <sup>0.66</sup> <sub>0.51</sub>	6.16 <sup>7.07</sup> <sub>5.35</sub>	11.62 <sup>13.47</sup> <sub>9.89</sub>	0.32 <sup>0.34</sup> <sub>0.31</sub>	0.01 <sup>0.07</sup> <sub>0.00</sub>
B	1.5	0.37 <sup>0.39</sup> <sub>0.35</sub>	0.39 <sup>0.41</sup> <sub>0.36</sub>	1.56 <sup>1.72</sup> <sub>1.41</sub>	2.33 <sup>2.56</sup> <sub>2.10</sub>	0.43 <sup>0.44</sup> <sub>0.42</sub>	0.14 <sup>0.23</sup> <sub>0.02</sub>
C	2.5	0.46 <sup>0.51</sup> <sub>0.41</sub>	0.28 <sup>0.33</sup> <sub>0.24</sub>	0.04 <sup>0.19</sup> <sub>0.02</sub>	0.32 <sup>0.48</sup> <sub>0.21</sub>	0.70 <sup>0.72</sup> <sub>0.68</sub>	0.54 <sup>0.75</sup> <sub>0.41</sub>
D	3.5	0.57 <sup>0.63</sup> <sub>0.52</sub>	0.23 <sup>0.28</sup> <sub>0.18</sub>	0.01 <sup>0.10</sup> <sub>0.00</sub>	0.05 <sup>0.15</sup> <sub>0.00</sub>	0.63 <sup>0.65</sup> <sub>0.62</sub>	1.13 <sup>1.32</sup> <sub>0.94</sub>
E	4.5	0.55 <sup>0.65</sup> <sub>0.48</sub>	0.19 <sup>0.27</sup> <sub>0.11</sub>	0.00 <sup>0.15</sup> <sub>0.00</sub>	0.00 <sup>0.10</sup> <sub>0.00</sub>	0.40 <sup>0.42</sup> <sub>0.38</sub>	0.92 <sup>1.11</sup> <sub>0.67</sub>
F	5.5	0.67 <sup>0.76</sup> <sub>0.58</sub>	0.09 <sup>0.18</sup> <sub>0.07</sub>	0.00 <sup>0.10</sup> <sub>0.00</sub>	0.00 <sup>0.08</sup> <sub>0.00</sub>	0.43 <sup>0.45</sup> <sub>0.42</sub>	1.38 <sup>1.61</sup> <sub>1.15</sub>
G	6.5	0.59 <sup>0.71</sup> <sub>0.51</sub>	0.15 <sup>0.26</sup> <sub>0.13</sub>	0.00 <sup>0.20</sup> <sub>0.00</sub>	0.00 <sup>0.07</sup> <sub>0.00</sub>	0.28 <sup>0.29</sup> <sub>0.27</sub>	0.90 <sup>1.12</sup> <sub>0.70</sub>
H	7.5	0.44 <sup>0.64</sup> <sub>0.28</sub>	0.28 <sup>0.46</sup> <sub>0.12</sub>	0.00 <sup>0.33</sup> <sub>0.00</sub>	0.00 <sup>0.20</sup> <sub>0.00</sub>	0.29 <sup>0.31</sup> <sub>0.27</sub>	1.31 <sup>1.68</sup> <sub>0.95</sub>
I	8.5	0.81 <sup>1.08</sup> <sub>0.56</sub>	0.36 <sup>0.62</sup> <sub>0.11</sub>	0.08 <sup>1.02</sup> <sub>0.00</sub>	0.05 <sup>0.45</sup> <sub>0.00</sub>	0.24 <sup>0.26</sup> <sub>0.21</sub>	1.23 <sup>1.67</sup> <sub>0.79</sub>
J	9.5	1.01 <sup>1.24</sup> <sub>0.79</sub>	0.28 <sup>0.50</sup> <sub>0.13</sub>	0.01 <sup>0.30</sup> <sub>0.00</sub>	0.00 <sup>0.19</sup> <sub>0.00</sub>	0.34 <sup>0.36</sup> <sub>0.31</sub>	1.45 <sup>1.85</sup> <sub>1.05</sub>
K	10.5	0.83 <sup>1.13</sup> <sub>0.55</sub>	0.35 <sup>0.61</sup> <sub>0.14</sub>	0.00 <sup>0.49</sup> <sub>0.00</sub>	0.00 <sup>0.25</sup> <sub>0.00</sub>	0.27 <sup>0.30</sup> <sub>0.24</sub>	1.20 <sup>1.62</sup> <sub>0.76</sub>

<sup>a</sup>All abundances are with respect to the average of the photospheric and meteoritic solar elemental abundances given in Table 4.1 adapted from Grevesse & Sauval 1998.

Note. — The numbers in the sub and superscripts for the abundances are the low and high extent of the 90% confidence region for that element.

above 6 keV, the abundance is constant at a value of 0.3 solar. Between 2.5 keV and 6 keV, the iron abundance falls from 0.7 solar to 0.3 solar, and from 0.5 keV to 2.5 keV the abundance rises steeply from 0.3 solar to 0.7 solar.

Also of note are the results from the second and third most strongly detected elements, silicon and sulfur. Here, the abundance ratios give some important information: the value of [Si/Fe] is generally super-solar, while the value of [S/Fe] is sub-solar. Table 4.6 gives the ratios of silicon, sulfur, and nickel to iron. Figure 4.4 shows the trend of the abundance ratios [Si/Fe] and [S/Fe] as a function of the

Table 4.6. Elemental Abundance Ratios

Stack Name	Temperature Bin	[Si/Fe]	[S/Fe]	[Si/S]	[Ni/Fe]	[Fe/H]
A	0.5	$-0.08_{-0.14}^{0.03}$	$0.26_{0.20}^{0.32}$	$-0.34_{-0.42}^{-0.27}$	$-1.81_{-\infty}^{-0.64}$	$-0.49_{-0.51}^{-0.47}$
B	1.5	$-0.07_{-0.09}^{-0.04}$	$-0.04_{-0.07}^{-0.01}$	$-0.02_{-0.06}^{0.01}$	$-0.47_{-1.27}^{-0.26}$	$-0.37_{-0.38}^{-0.36}$
C	2.5	$-0.18_{-0.24}^{-0.13}$	$-0.40_{-0.47}^{-0.33}$	$0.21_{0.12}^{0.29}$	$-0.11_{-0.23}^{0.03}$	$-0.16_{-0.17}^{-0.14}$
D	3.5	$-0.04_{-0.08}^{-0.00}$	$-0.44_{-0.55}^{-0.36}$	$0.40_{0.29}^{0.49}$	$0.25_{0.17}^{0.32}$	$-0.20_{-0.21}^{-0.19}$
E	4.5	$0.13_{0.07}^{0.21}$	$-0.34_{-0.56}^{-0.17}$	$0.47_{0.23}^{0.65}$	$0.36_{0.22}^{0.44}$	$-0.39_{-0.42}^{-0.38}$
F	5.5	$0.19_{0.13}^{0.25}$	$-0.69_{-0.80}^{-0.39}$	$0.88_{0.76}^{1.19}$	$0.50_{0.42}^{0.57}$	$-0.36_{-0.38}^{-0.35}$
G	6.5	$0.32_{0.25}^{0.40}$	$-0.28_{-0.35}^{-0.04}$	$0.61_{0.51}^{0.86}$	$0.50_{0.39}^{0.60}$	$-0.55_{-0.57}^{-0.53}$
H	7.5	$0.18_{-0.02}^{0.34}$	$-0.02_{-0.39}^{0.20}$	$0.20_{-0.29}^{0.45}$	$0.65_{0.51}^{0.76}$	$-0.54_{-0.57}^{-0.50}$
I	8.5	$0.53_{0.36}^{0.67}$	$0.18_{-0.35}^{0.42}$	$0.35_{-0.27}^{0.61}$	$0.71_{0.51}^{0.85}$	$-0.63_{-0.68}^{-0.58}$
J	9.5	$0.48_{0.37}^{0.57}$	$-0.07_{-0.41}^{0.18}$	$0.55_{0.18}^{0.81}$	$0.64_{0.49}^{0.74}$	$-0.47_{-0.51}^{-0.44}$
K	10.5	$0.49_{0.30}^{0.63}$	$0.11_{-0.29}^{0.36}$	$0.38_{-0.12}^{0.64}$	$0.65_{0.44}^{0.78}$	$-0.57_{-0.62}^{-0.53}$

Note. — All abundance ratios are with respect to the current abundances given in Table 4.5. The numbers in the sub and superscripts for the abundances are the low and high extent of the 90% confidence region for that element. Abundances are given in the usual dex notation, ie:  $[A/B] \equiv \log_{10}(N_A/N_B)_{\text{cluster}} - \log_{10}(N_A/N_B)_{\odot}$ .

iron abundance. Silicon and sulfur also show disagreement in their trend with temperature—the relative abundance of silicon rises with temperature, and sulfur falls. We find that the silicon abundance rises from  $\sim 0.3$  solar in cooler clusters to  $\sim 0.7$  solar in hot clusters, in excellent agreement with the results of Fukazawa et al. (1998).

Calcium and argon are noticeable for their lack of a detectable signal. Both are not detected in the stacked *ASCA* data, yielding only upper limits over the temperature range from 2–12 keV.

The relative abundances for nickel are measured to be higher than any other

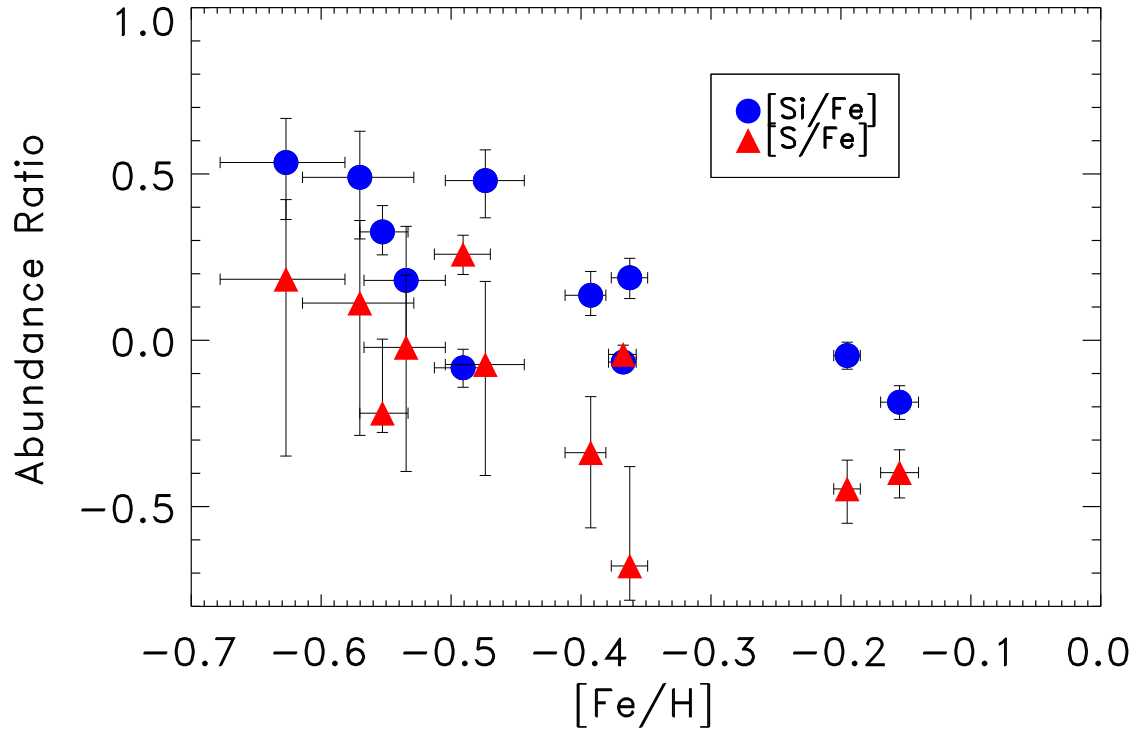


Figure 4.4: The silicon and sulfur abundances ratios with respect to iron.

element in our study. For clusters hotter than 4 keV, nickel is about 1.2 times the solar value. Lower temperature clusters are too cool to significantly excite the nickel  $K\text{-}\alpha$  transition, and abundances derived from the Ni L-shell lines are not reliable. The Ni/Fe values are extremely high at about 3 times the solar value, confirming the results of Dupke & White (2000a); Dupke & Arnaud (2001); Dupke & White (2000b).

## 4.6 Systematic Errors

The abundances results in this paper depend upon the measurement of particular spectral lines that are not always very strong. Because of this, a proper understanding of the results must take into account any systematic errors that may bias the results. Of particular concern to this work are systematic errors in the calibration of the effective area, since these often manifest themselves as lines in residual spectra of sources with a smooth continuum. If these residual lines fall at the same energy as the important elemental spectral lines they can have a significant affect on the derived elemental abundances.

The ACC catalog paper discusses general *ASCA* systematics and our sensitivity to them. In addition, there are several other tests we have undertaken to determine the effect of small line-like systematic errors in the effective area. In order to determine the size of any calibration errors, we have fit spectra from broad band continuum sources and quantified the residuals. We have also used these residuals to correct the cluster spectra, and have compared the derived elemental abundances to those from the uncorrected spectra.

We have used an *ASCA* observation of Cygnus X-1 (a bright source where the systematic errors dominate the statistical ones) to measure the size of residual lines in fitted spectra of a continuum source. These lines could be due to errors in the instrument calibration and could affect the abundance determinations in clusters. Using a `power law + diskline` model in *XPSEC*, we measure the largest residual in the Cyg X-1 spectrum to have an equivalent width of 17 eV at 3.6 eV. Using the Raymond-Smith plasma code to model the equivalent width of elemental X-ray lines, we find that the only element with a small enough equivalent width to be possibly affected by a 17 eV residual is calcium, with an equivalent width of 25 eV for very

hot clusters ( $> 6$  keV). However, the 17 eV residual lies at the wrong energy to affect calcium (lines at 3.8, 3.9, and 4.1 keV). In addition, the positive residual would serve to increase the measured calcium abundances; our measured calcium abundances are lower than expected. A similar test with the bright continuum source Mkn 421 (with the core emission removed to prevent pileup) shows a maximum residual of 18 eV equivalent width at the 2.11 keV Au edge of the mirror. These results indicate that any line-like calibration errors are not large enough to affect the cluster elemental abundance measurements in this study.

We have also used an *ASCA* observation of 3C 273 (sequence number 12601000) as a broad band continuum source to check for calibration errors in the response matrices and their effect on the derived cluster elemental abundances. We fit 3C 273 with an absorbed power law model (Figure 4.5) and extracted the ratio residuals to the best fit. We then used these residuals as a correction to the cluster data, and then refit the clusters to find the abundances. The abundances from the corrected data are completely consistent with the abundances from the uncorrected data, further indicating that errors in the effective area calibration do not affect the derived elemental abundances.

We have also investigated the abundances derived using the GIS and SIS detectors separately in order to check the consistency of our results. While the SIS has better spectral resolution, it also suffers from slight CTI and low energy absorption problems that do not affect the GIS. Figure 4.6 shows these results. In general, the GIS and SIS abundances match very well for most of the elements. However, nickel and silicon show a systematic trend of slightly higher SIS abundances. The SIS nickel abundances are not as reliable as the GIS abundances because the GIS has more effective area than the SIS at Ni K.

The systematic trend in the medium temperature silicon abundances is more

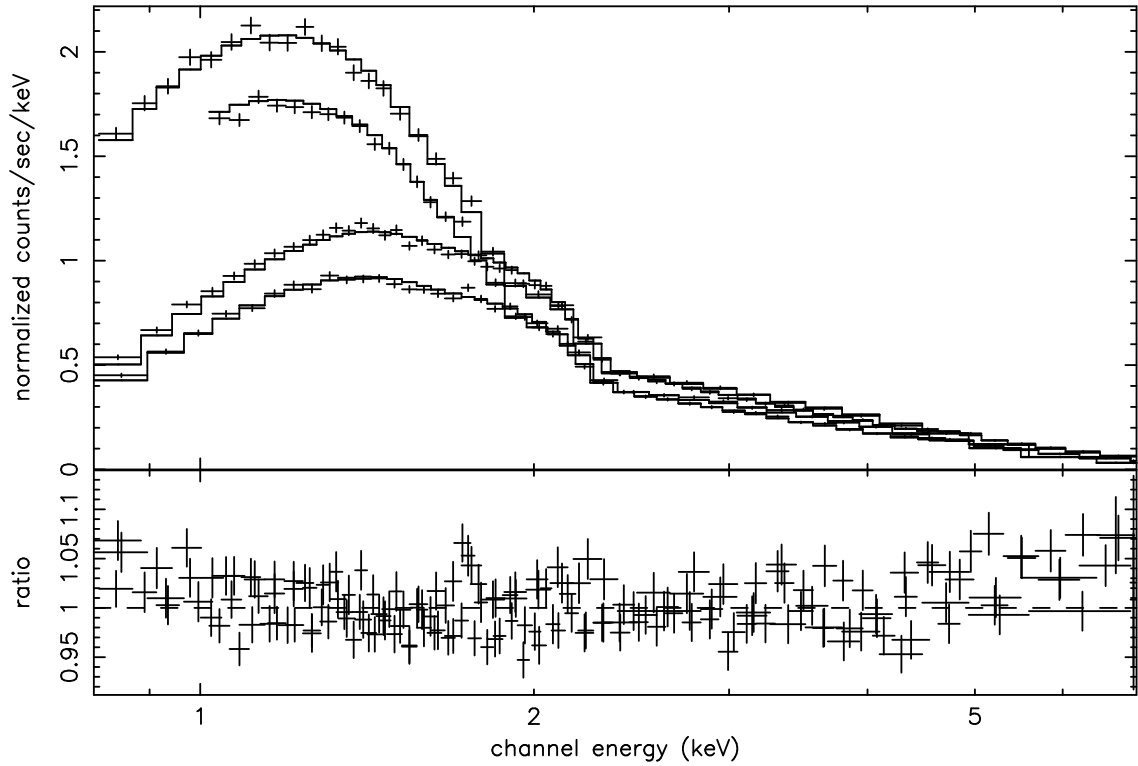


Figure 4.5: An absorbed power law fit to the *ASCA* 3C 273 data. The data and model are shown in the top panel for the 4 *ASCA* detectors, and the ratio of the data to the model is shown in the bottom panel. The lack of any significant residuals indicate that the *ASCA* effective area calibration is free of any significant line-like systematic errors.

difficult to understand. Fukazawa (1997) showed that the GIS and SIS sulfur and silicon abundances for his cluster sample were well matched. Individual analysis of the bright, medium temperature clusters Abell 496 and Abell 2199 show that the results are indeed real and verify that the SIS gives higher Si abundances than the GIS. Additional fits to the data that allow the SIS gain to vary also do not significantly affect the abundance results. One possible contribution to this problem is that the medium temperature clusters most affected by this trend mostly lie at a redshift such that the Si K-shell lines (1.86 and 2.00 keV) are redshifted very close

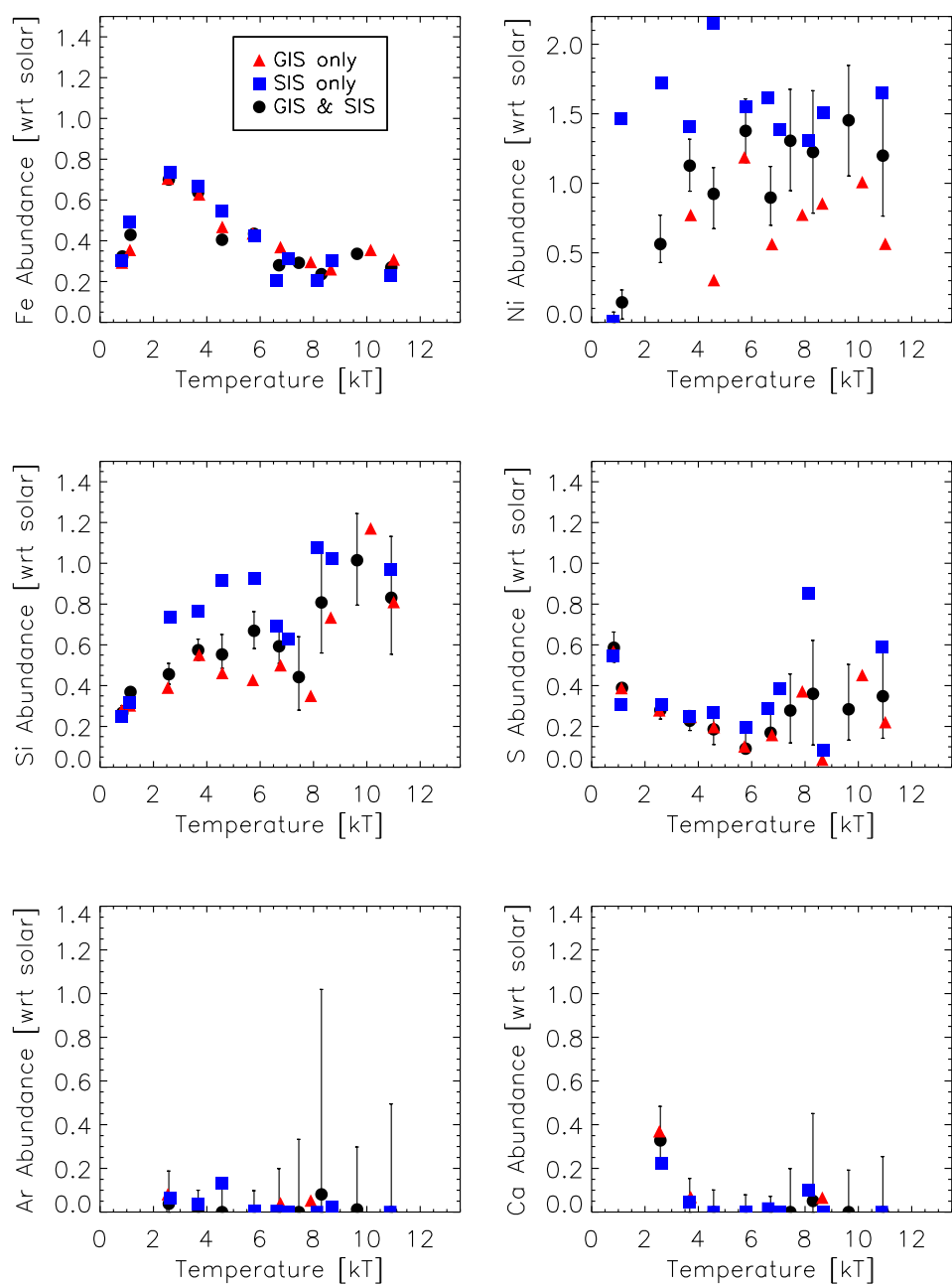


Figure 4.6: A comparison of abundance results using the GIS alone, the SIS alone, and the GIS and SIS combined. The GIS and SIS agree well except for nickel and a slight trend in the medium temperature silicon results. The nickel discrepancies are due to the lower effectiveness of the SIS at Ni K, and the SIS silicon measurements suffer from proximity to the detector Si edge. The errorbars for the GIS and SIS alone points are omitted for clarity, but are about a factor of  $\sqrt{2}$  larger than those for the combined points.

to the Si edge (1.84 keV) in the detector. These silicon abundances are less reliable because of structure present in the Si edge not well modeled in the instrument response (Mori et al. 2000).

The fit results in the 0.5 and 1.5 keV bins from Tables 4.3, 4.4, and 4.5 show elevated calcium and argon abundances. These very high fit results (1–10 times solar) are not believed to be indicative of the actual cluster abundances because of systematic errors that preferentially affect these low temperature bins. Two sources of systematic error we have identified both become important at low cluster temperatures and affect the modeled spectrum at the higher energies of the Ar and Ca K-shell lines.

The first is background subtraction: because the dominant bremsstrahlung emission is limited to lower energies for the cooler clusters, the cluster flux present at the higher energies of the Ar and Ca K-shell lines becomes comparable to the background. Small errors in the blank sky background can then significantly affect the background-subtracted data, leading to incorrect abundances at higher energies where the relative errors from the background subtraction become large.

Also important at the lower cluster temperatures where the bremsstrahlung emission does not dominate throughout the X-ray spectrum is the contribution from point sources within the individual galaxies. Angelini, Loewenstein, & Mushotzky (2001) and Irwin, Athey, & Bregman (2003) have shown with data from elliptical galaxies that the contribution from X-ray binaries is important and can be characterized with a 7 keV bremsstrahlung model. Since we do not include this component in our cluster fits, we expect that our Ar and Ca abundance for low temperature clusters will be driven upwards in an attempt to try and match the flux actually contributed by the X-ray point sources.

## 4.7 Comparisons

We believe that X-ray determinations of elemental abundances in galaxy clusters are one of the most accessible means for obtaining useful abundance measurements. While our results are consistent with and significantly expand previous cluster X-ray measurements, they do not always agree with measurements of elemental abundances in other objects.

### 4.7.1 Comparison to Other Cluster X-ray Measurements

#### *ASCA* Measurements

Measurements of abundances for elements other than iron has historically been difficult because of the low equivalent width of the lines and the limited resolution of X-ray detectors. Aside from a few limited results with crystal spectrometers on *Einstein* and other satellites, the first chemical abundance measurements of elements other than iron in galaxy clusters was made by Mushotzky et al. (1996) and made use of the high resolution of the CCD cameras onboard *ASCA*. Their results for 4 moderate temperature (2.5–5.0 keV), very bright clusters show an average Fe abundance of 0.32 solar, 0.65 solar for Si, 0.25 for S, and 1.0 for Ni. All of these results are in agreement with our results for moderate temperature clusters presented in Table 4.4. Fukazawa et al. (1998) also reported results for the silicon abundance in clusters that used *ASCA* data. Their results for 40 clusters was in general agreement with the data from Mushotzky et al. (1996), showing a generally constant iron abundance for clusters above 3 keV, and also hinted at the silicon trend with temperature presented with more detail here.

Finoguenov, David, & Ponman (2000) and Finoguenov, Arnaud, & David (2001) concentrated on the detection of abundance gradients with *ASCA*. Their data for Fe and Si at large radii are in agreement with ours. However, they present measurements of S coupled with Ar in order to reduce errors in the S determination. We see that these elements have very different abundances, and can't compare our data directly to theirs.

### ***XMM-Newton* Measurements**

Further results for the intermediate element abundances in clusters with *ASCA* were hampered by its moderate resolution, and especially because only a handful of clusters have high enough X-ray flux to allow meaningful measurements. The advent of *Chandra* and especially *XMM-Newton* have changed this with their higher resolution CCD cameras and much increased effective area. While measurements of argon and calcium are still beset with systematic problems in the *XMM-Newton* response and background subtraction, measurements of silicon and sulfur are largely free of these complications.

The much improved spatial and spectral resolution of *XMM-Newton* allow not only abundance measurements averaged over the whole cluster, but also spatially resolved ones. While our measurements in clusters are overall spatial averages, the measurements with *XMM-Newton* are usually spatially resolved and give information on abundance gradients within clusters. While this information is important and sheds valuable light on the enrichment mechanisms in clusters, we will limit our comparisons to overall abundances measured with *XMM-Newton*, or with abundances in the more voluminous outer regions of clusters with spatially resolved abundances.

The many *XMM-Newton* papers on M87 (Böhringer et al. 2001; Molendi &

Gastaldello 2001; Gastaldello & Molendi 2002; Matsushita, Finoguenov, & Böhringer 2003) all find a significant abundance gradient in the center of the cluster. In the very center, Molendi & Gastaldello (2001) find generally higher abundances than in the outer regions, with the iron abundance at about 0.6 the solar value. They find silicon to be 1.0 in the same region, giving  $[\text{Si}/\text{Fe}]$  only slightly lower than our results for a similar temperature cluster. However, sulfur is about 1.1 solar, overly abundant with respect to iron than in our results. The discrepancies between some of our results for 2.5 keV clusters and the *XMM-Newton* M87 results are tempered by the fact that earlier *ASCA* results for M87 (Matsumoto et al. 1996; Guainazzi & Molendi 1999) are similar to the *XMM-Newton* results, and by the fact that the M87 data is for only one cluster, while our *ASCA* results are for an average of several clusters at the same temperature.

Tamura et al. (2001) find sulfur and silicon to have similar abundances in the center of A496 with RGS data from *XMM-Newton*, slightly different than our results that show silicon slightly higher than sulfur by a factor of about 1.5. Unfortunately, the M87 data concentrates on the cluster core, and the A496 data is taken with the RGS, which also is limited to the centers of bright clusters. This bias toward the very centers of clusters makes a comparison with our average cluster abundances difficult.

Finoguenov et al. (2002) also look at *XMM-Newton* data for M87, but focus their paper on a discussion of the supernovae enrichment needed to account for the observed abundances. Their data leads them to conclude, as we do, that the standard yields of the canonical SN Ia and SN II models are not sufficient to explain the pattern of abundances observed. Their solution calls for an additional source of metals from a new class of type I supernovae. This scenario does not fit our data well; specifically, it leads to an overproduction of sulfur, argon and calcium, with

not enough silicon produced to match our observations. Finoguenov et al. (2002) focus on the inner 70 kpc region of M87 because of the cluster's proximity. Their results in this region are where the influence of the galaxy's stellar population and associated SNIa are most keenly apparent. Even at the outer parts of this region, the abundances show signs of a transition to a more typical cluster pattern. This inner region contributes a small fraction of the emission measure of most systems in our ACC sample, and makes comparisons difficult since we sample different areas of the cluster.

## 4.7.2 Comparison to Measurements in Different Types of Objects

### The Thin Disk

The standard solar elemental composition is based on measurements taken of the sun, which resides in the thin disk of the galaxy. Our cluster results show significant differences with stellar data from the thin disk. Figure 4.7 shows silicon and sulfur abundance ratios in clusters compared with data from Timmes, Woosley, & Weaver (1995). The stellar data is overplotted on the cluster points as grey bars. The [Si/Fe] cluster data overlaps with the stellar data, but has a much greater range. The [S/Fe] cluster data lies almost totally below the stellar data. The largest discrepancy is between the cluster and stellar nickel abundance ratios; clusters are higher than the stellar data of 0.1 by 0.5 dex. This very high value for [Ni/Fe] is not seen in stars at any metallicity.

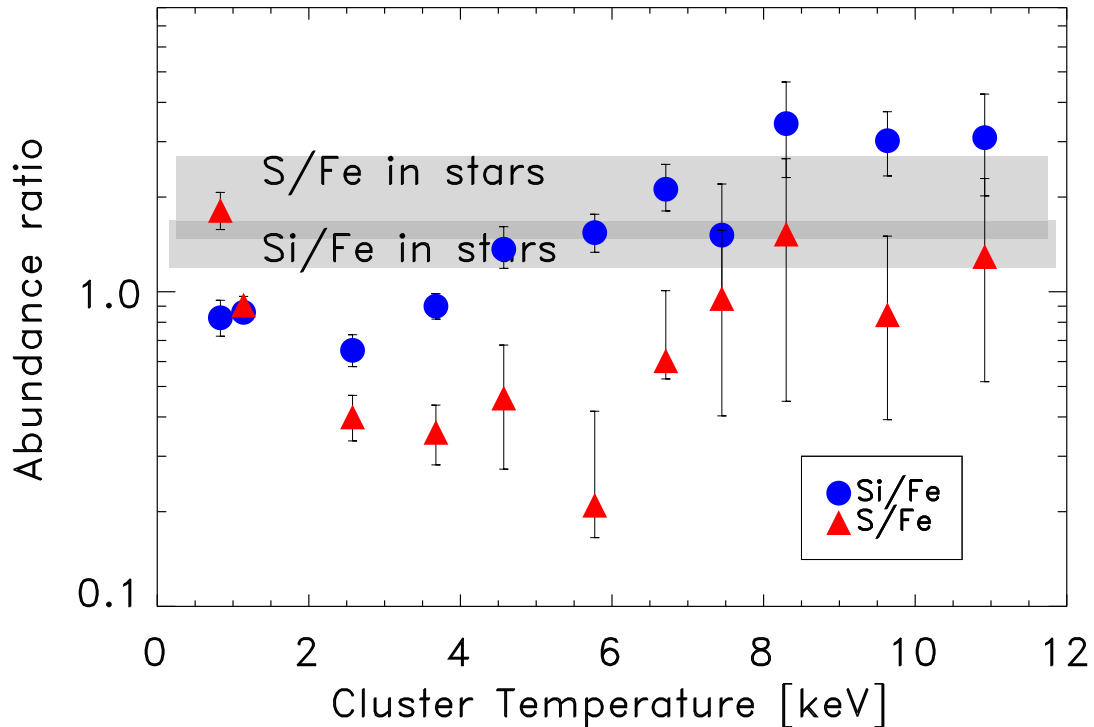


Figure 4.7: The silicon and sulfur abundances as a function of temperature, compared to their abundance in stars. The upper grey bar is the S/Fe data from Timmes, Woosley, & Weaver (1995), and the overlapping lower grey bar is the Si/Fe data from the same source.

### The Thick Disk

The majority of the stellar mass in clusters resides in elliptical galaxies and the bulges and halos of spirals (Bell, McIntosh, Katz, & Weinberg 2003). Prochaska et al. (2000) find that the abundance patterns of the thick disk are in excellent agreement with those in the bulge, suggesting that the two formed from the same reservoir of gas. If this is true, and if the majority of the enriched gas in the ICM originated in these numerically dominant stellar populations, then we would expect that the abundance pattern in the ICM is in good agreement with that in the thick disk of the Milky Way. However, reality is more complicated. While Prochaska

et al. (2000) find that the thick disk has enhanced abundances for the  $\alpha$  elements compared to the thin disk and solar neighborhood, they also find  $[\text{Ni}/\text{Fe}]$  in the thick disk is similar to its solar value. Additionally, the calcium abundance ratio is found to be super solar ( $[\text{Ca}/\text{Fe}] = 0.2$ ), and sulfur is more enhanced with respect to iron in the thick disk than in clusters. Also, the recent work of Pompeia, Barbuy, & Grenon (2003) shows a  $[\text{Si}/\text{Fe}]$  value of nearly 0.0, much lower than what we observe here.

## **H II Regions and Planetary Nebulae**

Comparison of our cluster results with H II regions or planetary nebulae is difficult because of the strong effects of dust and non-LTE conditions on abundance measurements of elements like iron and silicon (Peimbert, Carigi, & Peimbert 2001; Stasinska 2002). C, N, and O are more readily observed in these objects, but are not observed with *ASCA*.

## **Damped Ly- $\alpha$ Absorbers**

Prochaska & Wolfe (2002) show abundance measurements from a large database of damped Ly- $\alpha$  (DLA) observations. Their results are for the redshift range  $1.5 < z < 3.5$  and indicate that there is already significant  $\alpha$  element enhancement at high redshifts. This conclusion is consistent with that reached by Mushotzky et al. (1996) in an analysis of high redshift clusters. The  $[\text{Fe}/\text{H}]$  value observed by Prochaska & Wolfe of -1.6 is constant over a wide range of redshift, indicating that the enrichment was at earlier times. This value is much lower than our value of  $[\text{Fe}/\text{H}] = -0.5$  (for our higher temperature bins where the iron abundance is fairly constant), showing the importance of supernovae enrichment in the ICM. Their average  $[\text{Si}/\text{Fe}]$  value of 0.35 agrees with our results for moderate temperature clusters, and their spread of

[Si/Fe] measurements from 0.0 to 0.5 is well matched with ours. Their [Si/Fe] values are also constant over a wide redshift range, further supporting early enrichment. However, their results for sulfur differ from ours in that they show more enrichment with respect to iron ( $[S/Fe] \sim 0.4$ ) than we do. This suggests that later enrichment by supernovae into the ICM had a reduced role for sulfur in comparison to the other elements. Nickel is also different in these systems than in clusters, with  $[Ni/Fe]$  of only 0.07; much different than our very high value of  $\sim 0.5$ . While Prochaska & Wolfe (2002) have some results for argon, they are widely scattered and not easily interpreted. The differences with the cluster measurements of S and Ni indicate that the stellar population that enriched these systems is probably not the origin of the metals in the ICM.

### **Lyman Break Galaxies**

Pettini et al. (2002) present detailed observations of a lensed Lyman break galaxy at  $z = 2.7$ . Their results also indicate that significant metal enrichment have already taken place at high redshift. Their results for O, Mg, Si, S, and P are all at about 0.4 the solar value, showing the results of fast supernovae processing. However, the iron peak elements are not as enriched, with the values of Mn, Fe, and Ni at only 1/3 solar. The interpretation is that this galaxy has been caught in the middle of turning its gas into stars, and that while enrichment from SN II has occurred, not enough time has passed to allow significant enrichment from the iron peak producing SN Ia. The overall metallicity of  $[Fe/H] = -1.2$  is closer to our observed cluster value than the measurements from the DLAs are. However, the abundance ratios in this object are also sufficiently different than in clusters to indicate that the stellar population that enriched the Lyman break galaxies is also probably not the source of the metals in the ICM.

## The Ly- $\alpha$ Forest

While it is possible to probe the metallicity history of the universe as a function of redshift (Songaila 2001; Songaila & Cowie 2002), the difficulty inherent in measuring lines from many different elements in the Ly- $\alpha$  forest has made abundance measurements of most elements besides O, C, N, and Si unavailable. The reported abundances are almost two orders of magnitude lower than ours, with representative values for  $[C/H]$  around -3.4 (Schaye et al. 2003).

## 4.8 Supernovae Type Decomposition

With the results of § 4.5 for the abundance of the intermediate elements in clusters, it is possible to try to constrain the mix of supernovae types that have enriched the ICM. In § 4.8.1, we check to see how well the yields from the standard SN Ia and SN II models can reproduce the cluster observations. We find that other sources of metals are necessary. Then we comment on the expected cluster abundances derived using some of the standard models in the literature. In § 4.8.3, we investigate different SN models that produce intermediate elements with the abundance ratios necessary for reconciling the models with the observations.

### 4.8.1 SN Fraction Analysis using Canonical SN Ia and SN II Models

We use the yields of the revised W7 model (Nomoto et al. 1997b) for SN Ia and the TNH-40 yields (Nomoto et al. 1997a) (mass-averaged by integrating across the IMF to an upper limit of 40 solar masses) for SN II (shown in Figure 4.8) as our basis. Each model includes the amount of each of the intermediate elements produced in

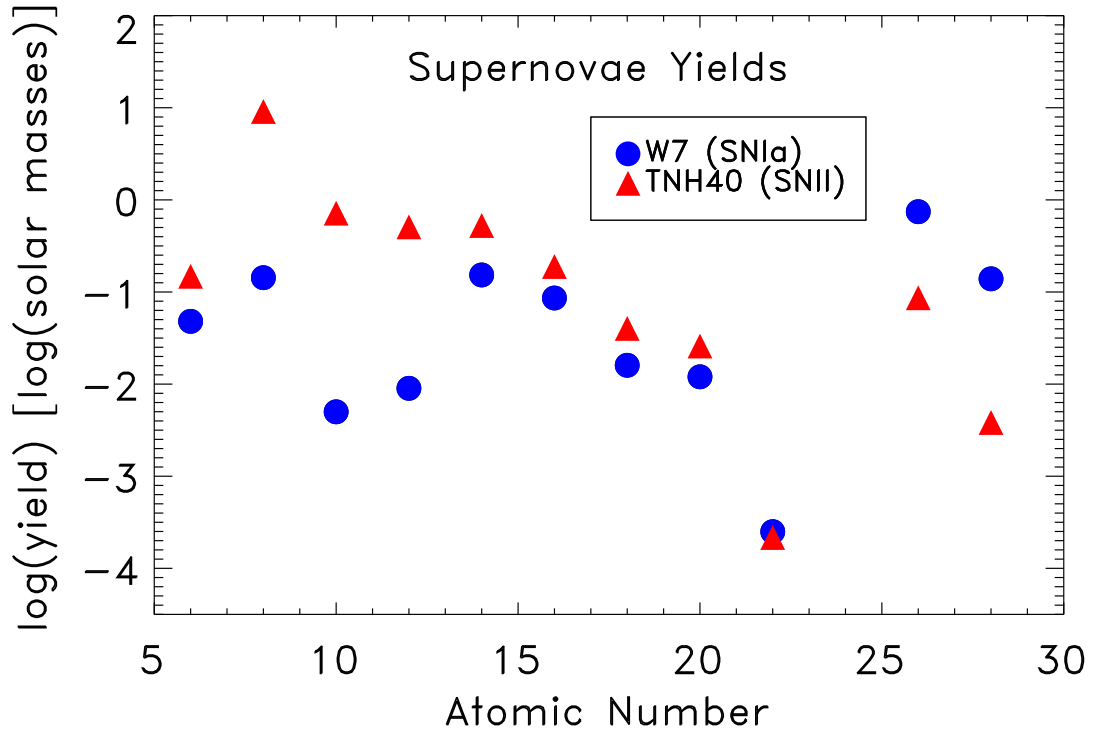


Figure 4.8: The Type Ia and Type II supernovae yields. The horizontal axis is atomic number—O is 8, Fe 26, Si 14, S 16, Ni 28. The yields are in solar masses per supernova. Iron comes mostly from SNIa and nickel even more so. Si, S, Ar, and Ca are a mix of SNII and SNIa but with a majority SNII contribution. The SNIa data comes from the W7 model, and the SNII data is from the IMF mass-averaged TNH-40 model.

a supernova of that type.

We used the data from the models to produce a table with the yields and abundance ratios for 100 different mixtures of SNIa and SNII ranging from pure SNIa enrichment to pure SNII enrichment. We then compare our two best-measured cluster abundance ratios (Si/Fe and S/Fe) with the model ratios in order to arrive at a SN type fraction. The results are plotted in Figure 4.9 and show the SN type fraction derived from both Si/Fe and S/Fe as a function of cluster temperature.

The difficulty of calculating SN yields leads to acknowledged uncertainties for

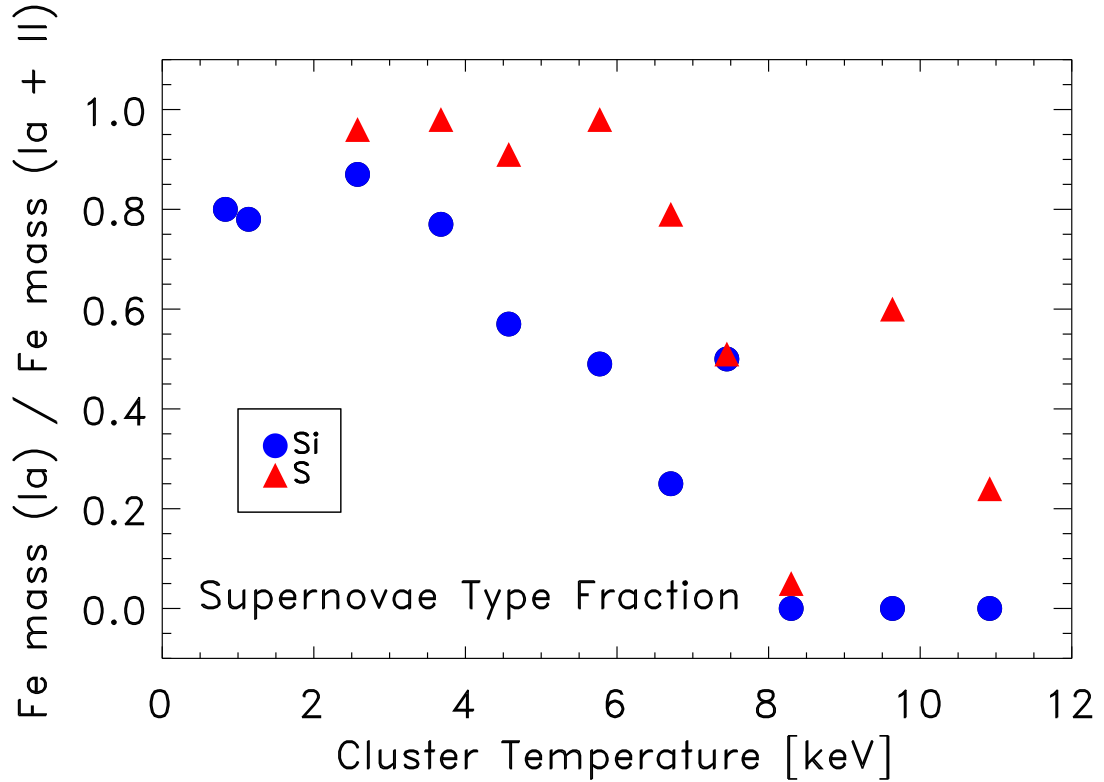


Figure 4.9: The supernovae-type ratio derived from the silicon and sulfur abundances. The SNIa yields of the W7 model (Nomoto et al. 1997b) and the SNIi yields of the IMF mass-averaged TNH-40 (Nomoto et al. 1997a) model were used to compute the Si/Fe and S/Fe abundance ratios for 100 mixtures ranging from pure SNIa enrichment to pure SNIi enrichment. The measured data was compared to the model output in order to determine the relative ratio of SNIa and SNIi. A value of 1 on the plot indicates enrichment by solely SNIa while a value of 0 indicates enrichment solely by SNIi.

some of the elements of about a factor of two (Gibson, Loewenstein, & Mushotzky 1997). In order to investigate the effects of different SN models on the derived SN fraction, we have compared the SN fractions derived from several different SN models in Figure 4.10. Each SN fraction determination uses the W7 SNIa model as revised in Nomoto et al. (1997b), but uses a different SNIi model. The result of this comparison indicates that different SNIi models can change the average value for the derived SN fraction, but does not change the fact that none of the seven

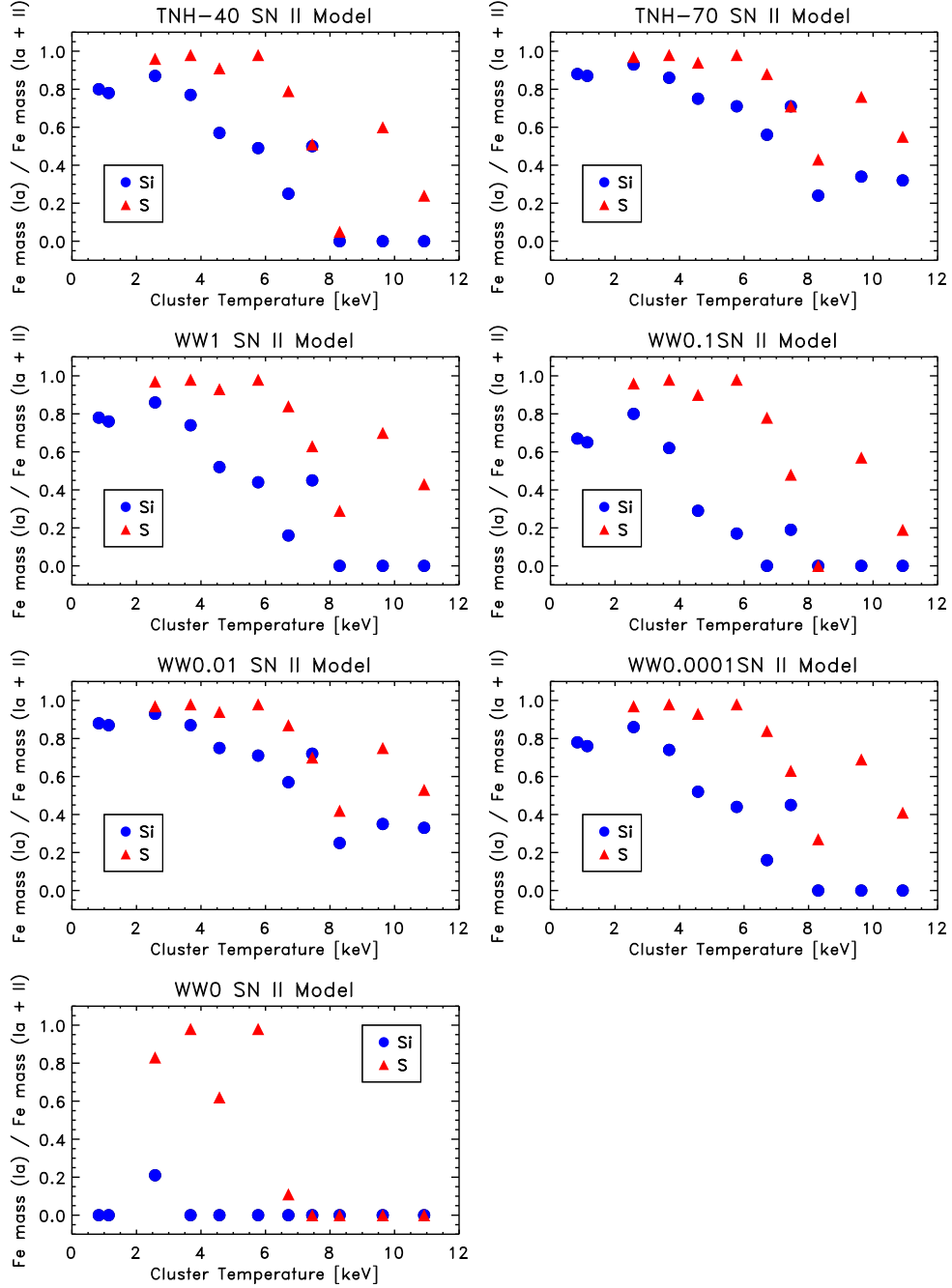


Figure 4.10: The supernovae-type ratio derived from the silicon and sulfur abundances, comparing the results from many different SN II models. This figure is similar to Figure 4.9, but shows that many different SN II models all have difficulty producing a consistent type fraction from the silicon and sulfur data. Also, the trend of cooler clusters predominantly enriched by type SN Ia products and hotter clusters enriched by SN II products does not depend on the SN II model used. Again, a value of 1 on the plot indicates enrichment by solely SN Ia while a value of 0 indicates enrichment solely by SN II.

SN II models results in a consistent SN fraction from both the cluster Si/Fe and S/Fe data.

The results we have found for the cluster intermediate element abundances do not fit the standard model where most of the elements are produced in a simple mix of standard SN Ia and SN II events. The observed silicon abundance is too high with respect to iron, and the observed sulfur abundance too low. Calcium and argon are also too low. The SN type fractions derived from the two abundance ratios are not consistent with each other, and change dramatically as a function of cluster temperature. *These results indicate that a unique, consistent decomposition of the ICM enrichment into SN Ia and SN II contributions is not possible.*

Faced with these inconsistencies, new models must be examined that can better explain our results. Some possibilities are included in the following section.

#### **4.8.2 Expected Abundances from Standard SN Models**

There are many different supernovae yield computations in the scientific literature. For SN II, there are variations in the progenitor masses, metallicities and internal structure; in explosion energy and placement of the mass cut; and in adopted nuclear reaction rates. For SN Ia, parameters include the central white dwarf progenitor density and burning front propagation speed. Initially, we consider the standard W7 deflagration SN Ia model and Salpeter-IMF-averaged SN II yields from Nomoto et al. (1997b). In all cases, a combination of SN Ia and SN II yields is necessary to match the observed results.

About 0.02 SN II events per current solar mass of stars will occur if most of the stars in cluster galaxies form over an interval much shorter than the age of the universe (indicated by the predominance of early-type galaxies in clusters) and if star formation proceeds with a standard IMF (Kroupa 2002). This calculation takes

Table 4.7. Observed and Model Abundances

Element	<i>ASCA</i>	SN II	SN Ia	SN II+SN Ia	+SN IIx <sup>a</sup>	+SN IIx <sup>b</sup>	+SN IIx <sup>c</sup>
Si	0.6–0.8	0.34	0.095	0.4	0.7	0.7	0.7
S	0.1–0.4	0.20	0.09	0.3	0.4	0.3	0.4
Ar	0.0–0.2	0.17	0.075	0.25	0.3	0.2	0.3
Ca	0.0–0.2	0.19	0.09	0.3	0.35	0.3	0.35
Fe	0.4	0.14	0.26	0.4	0.4	0.4	0.4
Ni	0.8–1.5	0.16	0.85	1.0	1.0	1.0	1.0

Note. — Abundances are given with respect to the solar values in Table 4.1, column 3.

<sup>a</sup>70  $M_{\odot}$  progenitors (Thielemann, Nomoto, & Hashimoto 1996) in addition to SN II and SN Ia.

<sup>b</sup>0.01 solar abundance, > 30  $M_{\odot}$  progenitors (Woosley & Weaver 1995) in addition to SN II and SN Ia.

<sup>c</sup>70  $M_{\odot}$  He core Pop III progenitors (Heger & Woosley 2002) in addition to SN II and SN Ia.

the mass lost to winds and remnants into account and assumes the SN II progenitors are stars with original mass > 8  $M_{\odot}$ . Column 2 of Table 4.7 shows the observational range we aim to explain, Column 3 of Table 4.7 shows the model abundances from ICM enrichment by SN II (for the gas-to-star mass ratio of 10 that is typical of a rich cluster).

If the assumption is made that SN Ia provide the remainder of the iron (The enrichment levels due solely to SN Ia enrichment are in column 4 of Table 4.7), then the total expected abundances (SN II + SN Ia) are as shown in column 5 of Table 4.7. The number of SN Ia required corresponds to an average of 1.8 SNU over  $10^{10}$  years for a typical ratio of ICM mass to stellar blue light of 40, significantly higher than the estimated optical rate at  $z = 0$  (Cappellaro et al. 1997). This combination of SN II and SN Ia accounts for the observed abundances of nickel and sulfur (compare columns 2 and 5 of Table 4.7). However, only about half of the observed silicon is

accounted for and calcium and argon are slightly overproduced. Different models must be investigated to make up this significant shortfall. The most variation in SN yields is in SN II models, and we explore some of these alternatives below.

Unfortunately, many SN II models, in particular those of Woosley & Weaver (1995) and Rauscher, Heger, Hoffman, & Woosley (2002), generally derive higher yields of sulfur, argon and calcium that exacerbate the conflict between theory and observations. In addition, SN II iron yields are uncertain by at least a factor of two (Gibson, Loewenstein, & Mushotzky 1997) because of their sensitivity to the assumed mass cut. If one arbitrarily and exclusively increases the SN II contribution to the iron yield by a factor of two, then the SNIa contribution to sulfur, argon and calcium goes down by a factor of two and is in marginal agreement with the observations. Unfortunately, this scenario increases the silicon deficit and the nickel abundance falls to the unacceptably low value of about half solar.

Models that explicitly synthesize more iron (e.g., those of Woosley & Weaver (1995) with enhanced explosion energy) also generally produce more sulfur, argon and calcium that enhances the problem with those elements. However, the Woosley & Weaver (1995) enhanced energy models having zero metallicity progenitors have a very different nucleosynthetic profile—the production of iron and nickel averaged over the IMF is doubled without an increase in sulfur, argon and calcium. Unfortunately, silicon and nickel remain underproduced by a factor of two if these SN II yields are adopted.

Other variations on the SN II yields also fail to explain the low ratio of sulfur, argon and calcium to silicon. Neither adopting delayed detonation SNIa models (Finoguenov et al. 2002) nor increasing the silicon abundance by assuming a flat IMF (Loewenstein & Mushotzky 1996) solves the problem. Finoguenov et al. (2002) explain the abundance pattern and its radial variation in M87 by proposing (1) a

radially increasing SNII/SNIa ratio, (2) high Si and S yields from SNIa (favoring delayed detonation models) and an *ad hoc* reduction in SNII S yields, and (3) a radial variation in SNIa yields (corresponding to delayed detonation models with different deflagration-to-detonation transition densities). While this scenario appears promising with regard to the galaxy-dominated inner regions of rich clusters and, perhaps groups, there are difficulties—as Finoguenov et al. (2002) acknowledge—in explaining the pattern in the large scale abundances of high-temperature clusters.

One possible solution is to assume a flat IMF to boost SNII silicon production (and account for at least half of the iron), combined with *ad hoc* reductions in sulfur, argon and calcium yields by a factor of two. An increase in the SNII nickel yields (uncertain by a factor of two because of mass cut and core neutron excess uncertainties, Nakamura et al. 1999) would also have to be instated to account for the lowered nickel from the reduced SNIa output. On the other hand, if a standard IMF is maintained, then less significant decreases in SNII production of sulfur, argon and calcium are needed. For this case, the silicon deficit would have to be made up by another mechanism; enhanced hydrostatic production of silicon or a suppressed efficiency of silicon burning are possibilities.

### 4.8.3 Alternate Enrichment Scenarios

If the observed cluster iron abundance and stellar elemental abundances are used to set the contribution from supernovae, then the theoretical yields will meet or slightly exceed the *ASCA* abundance observations for argon and calcium while silicon itself will be significantly underproduced by a factor of  $\sim 2$ . If we accept the standard SNII enrichment given in column 3 of Table 4.7, then we must have an additional nucleosynthetic source that produces substantial silicon, but little or no sulfur, argon, or calcium. Some possibilities exist in the literature, and we explore

some of these scenarios below. We have chosen single mass SN II models that can selectively enhance silicon, and collectively call these models “SN IIx” to distinguish them from the canonical SN II models. For the models presented below, we calculate the number of SN IIx events necessary to produce the observed amounts of iron and silicon that are not produced by regular SN II.

### **Very Massive Stars**

Thielemann, Nomoto, & Hashimoto (1996) have calculated the yields for a  $70 M_{\odot}$  progenitor with solar metallicity. The abundance ratios in the ejecta with respect to silicon are: 0.4, 0.28, 0.26, 0.048, and 0.12 relative to solar for S, Ar, Ca, Fe, and Ni. With these results, the observational overabundance of silicon can be accounted for with  $\sim 2 \times 10^{-4}$  SN IIx per solar mass in the ICM. This rate will provide the extra silicon necessary, is only about 10% of the total number of SN II expected by integrating a normal IMF, and only produces minor perturbations in the other elements. The abundances expected from the combination of SN Ia, canonical SN II, and SN IIx from very massive progenitors is given in column 6 of Table 4.7.

### **Massive, Metal-poor Stars**

Very small amounts of the elements heavier than silicon are produced in the high mass ( $> 25 M_{\odot}$ ), low-metallicity (0.01, 0.1 solar) models of Woosley & Weaver (1995). These yields give less than 10% of the solar ratios (with respect to silicon) for elements heavier than silicon. Hence, silicon abundances can be increased without causing the other elements to exceed their observed values. In order to produce the observed abundances, about  $5.7 \times 10^{-4}$  SN IIx per solar mass in the ICM are necessary, assuming progenitors of 30–40  $M_{\odot}$  with 0.01 solar abundance and an IMF that goes as  $M^{-1}$ . The abundances expected from the combination of

SN Ia, canonical SN II, and SN IIx from massive, metal-poor progenitors is given in column 7 of Table 4.7.

### **Population III Stars**

The ejecta of supernovae preceded by very massive, zero metallicity progenitor stars (Pop III stars) have a substantially different composition than standard SN II ejecta (e.g., Heger & Woosley (2002)). If the Pop III mass function is dominated by the low mass (He cores  $< 80 M_{\odot}$ ) models of Heger & Woosley (2002), then the relative Si overabundance from observations can be explained. If higher core masses are used, the silicon overabundances are not as well explained, but more modest underabundances are found for sulfur, argon, and calcium. For example, about  $2.3 \times 10^{-5}$  SN IIx events per solar mass in the ICM from progenitors with  $70 M_{\odot}$  He cores matches our observed abundances and produce the abundances given in column 8 of Table 4.7.

Figure 4.11 is based on Table 4.7 and shows graphically what proportion of each element's abundance comes from SN Ia, SN II, and SN IIx. The three different SN IIx models all produce similar results, and provide the silicon necessary to match the observational overabundance without unduly exacerbating the low observed abundances of sulfur, argon and calcium.

#### **4.8.4 Discussion**

The anomalous abundance patterns found here in galaxy clusters are unique. The relative simplicity and uncomplicated nature of the X-ray emission from clusters and their role as a repository for all the enriched gas produced by supernovae makes them important objects for understanding the production and evolution of metals in the universe.

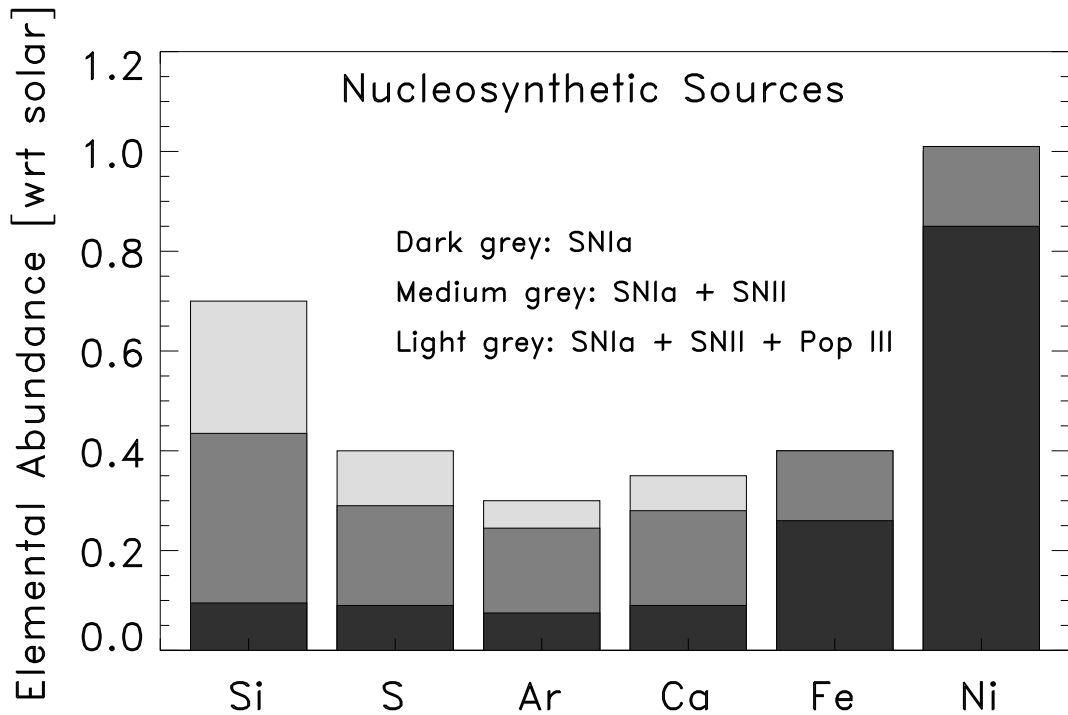


Figure 4.11: A decomposition of the intermediate element abundances into their nucleosynthetic origins based on Table 4.7. The lowest band in each bar is the contribution from SN Ia, the middle band adds the yields from the canonical SN II, and the top band includes the contribution from an early population of high mass, low metallicity Pop III supernovae progenitors. Iron and nickel both are dominated by SN Ia products, with no contribution by SN IIx from Pop III progenitors.

However, no combination of SN Ia and SN II products using current theoretical yields can produce the abundances observed with *ASCA*. Manipulating the standard models by changing the IMF or appealing to different physical models such as delayed detonation can help mitigate only some of the inconsistencies between models and observations. A new source of metals is needed in order satisfactorily explain the cluster abundances. The low ratios of S/Si, Ar/Si and Ca/Si are indicative of a fundamentally different mode of heavy metal enrichment. We have identified three

different SN models that can produce these metals in the correct proportions and have calculated the number of events necessary to match the observations when combined with metals produced in ordinary SNIa and SNII. These models all have in common very massive, metal poor progenitor stars.

It is natural to associate these with the earliest generation of (Pop III) stars. This primordial population must have existed, and its distinct characteristics are well matched to those required to explain the ICM abundance anomalies: zero metallicity, and a top-heavy IMF that has an important contribution from very massive stars (Bromm, Coppi, & Larson 1999; Abel, Bryan, & Norman 2000). Enhanced explosion energies are indicated, and nucleosynthetic production is high with an abundance pattern quite distinct from other SNII (Heger & Woosley 2002).

Loewenstein (2001) proposed hypernovae associated with Pop III as a means of enhancing silicon relative to oxygen in the ICM, and inferred a hypernovae rate of the same order as the SNIIx from Pop III stars derived here. The precise required number is subject to assumed values of the ICM/stellar ratio, the IMF and SNII yields for Pop II stars, and the IMF and SNIIx yields for Pop III stars, but is in the range of 10–30 times larger than the average value ( $\Omega_{III} \sim 4 \times 10^{-6}$ ) predicted in the semi-analytic models of Ostriker & Gnedin (1996). This could be the result of enhanced primordial star formation in these extremely overdense environments. Evidence also exists for more nearly solar abundance ratios in less massive clusters (Finoguenov et al. 2002).

Both observations and theory suggest the idea that a large population of massive, metal-poor Pop III stars was present at very high redshift and constituted the first generation of stars. The heavy metal products from this first generation would have been formed at the same time as the first galaxies or even before, and would now be widely dispersed in the ICM. Galaxy clusters serve as the largest repositories of both

enriched gas from cluster galaxies and of gas expelled by the earliest generations of stars and then accreted onto clusters. A combination of X-ray observations well matched to observing metal abundances in clusters and the importance of galaxy clusters as large retainers of Pop III enriched gas make these observations one of the best views onto the earliest generations of stars in the universe.

## 4.9 Summary

We have presented intermediate element abundances for galaxy clusters based on *ASCA* observations. Our measurements of the iron and silicon abundances agree with the past *ASCA* results of Fukazawa (1997) and Mushotzky et al. (1996), but achieve much higher precision and extend the temperature range from 0.5–12 keV. The measurements of the individual element abundances show some surprising new results: silicon and sulfur do not track each other as a function of temperature in clusters, and argon and calcium have much lower abundances than expected.

These results show that the  $\alpha$ -elements do not behave homogeneously as a single group. The unexpected abundance trends with temperature probably indicate that different enrichment mechanisms are important in clusters with different masses. The wide scatter in  $\alpha$ -element abundances at a single temperature could indicate that SN models need some fine tuning of the individual element yields, or that a different population of SN needs to be considered as important to metal enrichment in clusters.

We have also attempted to use our measured abundances to constrain the SN types that caused the metal enrichment in clusters. A first attempt to split the metal content into contributions from canonical SN Ia and SN II led to inconsistent results with both the individual elemental abundances and with the abundance ratios of

our most well measured elements. An investigation of different SN models also could not lead to a scenario consistent with the measured data, and we deduce that no combination of SN Ia and SN II fits the data. Another source of metals is needed.

This extra source of metals must be able to produce enough silicon to match the measurements, but not so much sulfur, argon, or calcium to exceed them. An investigation of SN models in the literature led to three separate models that could fulfill these requirements. All three models were similar, and had as progenitor stars massive and/or metal poor stars. The combination of canonical SN Ia and SN II with one of the new models does a much better job of matching the observations. These sorts of massive, metal poor progenitor stars are exactly the stars that are supposed to make up the very early Population III stars. The conjunction of our required extra source of metals with SN from population III-like progenitors supports the idea that a significant amount of metal enrichment was from the very earliest stars.

Clusters are a unique environment for elemental abundance measurements because they retain all the metals produced in them. The relatively uncomplicated physical environment in clusters also allows well-understood abundance measurements. Future abundance analyses using a large sample of *XMM-Newton* data will allow an even better understanding of the SN types and enrichment mechanisms important in galaxy clusters.

The authors would like to thank K. Gendreau for early assistance with this work and K. Kuntz for continued useful conversations and technical advice. The prompt and useful comments of the referee, A. Finoguenov, were also greatly appreciated. This research has made extensive use of data obtained from the High Energy Astrophysics Science Archive Research Center (HEASARC), provided by NASA's Goddard Space Flight Center; the NASA/IPAC Extragalactic Database (NED) which is operated by the Jet Propulsion Laboratory, California Institute of Technology,

under contract with the National Aeronautics and Space Administration; and the SIMBAD database, operated at CDS, Strasbourg, France. The authors extend their sincere thanks to the people responsible for making these resources available online.

# Bibliography

- Abel, T., Bryan, G. L., & Norman, M. L. 2000, *ApJ*, 540, 39
- Allende Prate, C., Lambert, D. L., & Asplund, M. 2001, *ApJ*, 556, L63
- Anders, E. & Grevesse, N. 1989, *Geochim. Cosmochim. Acta*, 53, 197
- Angelini, L., Loewenstein, M., & Mushotzky, R. F. 2001, *ApJ*, 557, L35
- Arnaud, M., Neumann, D. M., Aghanim, N., Gastaud, R., Majerowicz, S., & Hughes, J. P. 2001, *A&A*, 365, L80
- Arnaud, M., Rothenflug, R., Boulade, O., Vigroux, L., & Vangioni-Flam, E. 1992, *A&A*, 254, 49
- Becker, R. H., Smith, B. W., White, N. E., Holt, S. S., Boldt, E. A., Mushotzky, R. F., & Serlemitsos, P. J. 1979, *ApJ*, 234, L73
- Bell, E. F., McIntosh, D. H., Katz, N., & Weinberg, M. D. 2003, *ArXiv Astrophysics e-prints*, 2543
- Böhringer, H. et al. 2001, *A&A*, 365, L181
- Bromm, V., Coppi, P. S., & Larson, R. B. 1999, *ApJ*, 527, L5
- Cappellaro, E., Turatto, M., Tsvetkov, D. Y., Bartunov, O. S., Pollas, C., Evans, R., & Hamuy, M. 1997, *A&A*, 322, 431
- DeGrandi, S. 2003 in proceedings of the Ringberg Cluster Conference
- Dupke, R. A. & Arnaud, K. A. 2001, *ApJ*, 548, 141
- Dupke, R. A. & White, R. E. 2000a, *ApJ*, 528, 139

- Dupke, R. A. & White, R. E. 2000b, *ApJ*, 537, 123
- Finoguenov, A., Arnaud, M., & David, L. P. 2001, *ApJ*, 555, 191
- Finoguenov, A., David, L. P., & Ponman, T. J. 2000, *ApJ*, 544, 188
- Finoguenov, A., Matsushita, K., Böhringer, H., Ikebe, Y., & Arnaud, M. 2002, *A&A*, 381, 21
- Fukazawa, Y. 1997, Ph.D. Dissertation, University of Tokyo
- Fukazawa, Y., Makishima, K., Tamura, T., Ezawa, H., Xu, H., Ikebe, Y., Kikuchi, K., & Ohashi, T. 1998, *PASJ*, 50, 187
- Gastaldello, F. & Molendi, S. 2002, *ApJ*, 572, 160
- Gibson, B. K., Loewenstein, M., & Mushotzky, R. F. 1997, *MNRAS*, 290, 623
- Heger, A. & Woosley, S. E. 2002, *ApJ*, 567, 532 [
- Henry, R. B. C., & Worthey, G. 1999, *PASP*, 111, 119
- Horner, D. 2001, Ph.D. Dissertation, Department of Astronomy, University of Maryland College Park
- Horner, D. J., Baumgartner, W. H., Gendreau, K. C., & Mushotzky, R. F. 2003, *ApJS*, submitted
- Hwang, U., Mushotzky, R. F., Burns, J. O., Fukazawa, Y., & White, R. A. 1999, *ApJ*, 516, 604
- Irwin, J. A., Athey, A. E., & Bregman, J. N. 2003, *ApJ*, 587, 356
- Ishimaru, Y. & Arimoto, N. 1997, *PASJ*, 49, 1
- Kroupa, P. 2002, *Science*, 296, 82
- Grevesse, N. & Sauval, A. J. 1998, *Space Science Reviews*, 85, 161
- Grevesse, N. & Sauval, A. J. 1999, *A&A*, 347, 348
- Guainazzi, M. & Molendi, S. 1999, *A&A*, 351, L19
- Loewenstein, M. 2001, *ApJ*, 557, 573
- Loewenstein, M. & Mushotzky, R. F. 1996, *ApJ*, 466, 695

- Matsumoto, H., Koyama, K., Awaki, H., Tomida, H., Tsuru, T., Mushotzky, R., & Hatsukade, I. 1996, PASJ, 48, 201
- Matsushita, K., Finoguenov, A., & Böhringer, H. 2003, A&A, 401, 443
- Mitchell, R. J., Culhane, J. L., Davison, P. J. N., & Ives, J. C. 1976, MNRAS, 175, 29P
- Molendi, S. & Gastaldello, F. 2001, A&A, 375, L14
- Mori, K. et al. 2000, Proc. SPIE, 4012, 539
- Mushotzky, R. F. 1983, Presented at the Workshop on Hot Astrophys. Plasmas, Nice, 8-10 Nov. 1982, 83, 33826
- Mushotzky, R. F., Holt, S. S., Boldt, E. A., Serlemitsos, P. J., & Smith, B. W. 1981, ApJ, 244, L47
- Mushotzky, R. F. & Loewenstein, M. 1997, ApJ, 481, L63
- Mushotzky, R., Loewenstein, M., Arnaud, K. A., Tamura, T., Fukazawa, Y., Matsushita, K., Kikuchi, K., & Hatsukade, I. 1996, ApJ, 466, 686
- Mushotzky, R. F., Serlemitsos, P. J., Boldt, E. A., Holt, S. S., & Smith, B. W. 1978, ApJ, 225, 21
- Nakamura, T., Umeda, H., Nomoto, K., Thielemann, F., & Burrows, A. 1999, ApJ, 517, 193
- Nomoto, K., Hashimoto, M., Tsujimoto, T., Thielemann, F.-K., Kishimoto, N., Kubo, Y., & Nakasato, N. 1997, Nuclear Physics A, 616, 79
- Nomoto, K., Iwamoto, K., Nakasato, N., Hashimoto, Thielemann, F.-K., Brachwitz, F., Tsujimoto, T., Kubo, Y., & Kishimoto, N. 1997, Nuclear Physics A, 621, 467
- Ostriker, J. P. & Gnedin, N. Y. 1996, ApJ, 472, L63
- Peimbert, M., Carigi, L., & Peimbert, A. 2001, Astrophysics and Space Science Supplement, 277, 147
- Peterson, J. R., Kahn, S. M., Paerels, F. B. S., Kaastra, J. S., Tamura, T., Bleeker,

J. A. M., Ferrigno, C., & Jernigan, J. G. 2002, ArXiv Astrophysics e-prints, 10662

Pettini, M., Rix, S. A., Steidel, C. C., Adelberger, K. L., Hunt, M. P., & Shapley, A. E. 2002, ApJ, 569, 742

Pipino, A., Matteucci, F., Borgani, S., & Biviano, A. 2002, New Astronomy, 7, 227

Pompeia, L., Barbuy, B., & Grenon, M. 2003, ArXiv Astrophysics e-prints, 04282

Prochaska, J. X., Naumov, S. O., Carney, B. W., McWilliam, A., & Wolfe, A. M. 2000, AJ, 120, 2513

Prochaska, J. X. & Wolfe, A. M. 2002, ApJ, 566, 68

Rauscher, T., Heger, A., Hoffman, R. D., & Woosley, S. E. 2002, ApJ, 576, 323

Rothenflug, R., Vigroux, L., Mushotzky, R. F., & Holt, S. S. 1984, ApJ, 279, 53

Sakelliou, I. et al. 2002, A&A, 391, 903

Schaye, J., Aguirre, A., Kim, T., Theuns, T., Rauch, M., & Sargent, W. L. W. 2003, ApJ, 596, 768

Serlemitsos, P. J., Smith, B. W., Boldt, E. A., Holt, S. S., & Swank, J. H. 1977, ApJ, 211, L63

Smith, R. K., Brickhouse, N. S., Liedahl, D. A., & Raymond, J. S. 2001, ApJ, 556, 91

Songaila, A. 2001, ApJ, 561, L153

Songaila, A. & Cowie, L. L. 2002, AJ, 123, 2183

Stasinska, G. 2002, ArXiv Astrophysics e-prints, 7500

Tamura, T., Bleeker, J. A. M., Kaastra, J. S., Ferrigno, C., & Molendi, S. 2001, A&A, 379, 107

Tanaka, Y., Inoue, H., & Holt, S. S. 1994, PASJ, 46, L37

Thielemann, F., Nomoto, K., & Hashimoto, M. 1996, ApJ, 460, 408

Timmes, F. X., Woosley, S. E., & Weaver, T. A. 1995, ApJS, 98, 617

Wilms, J., Allen, A., & McCray, R. 2000, ApJ, 542, 914

Woosley, S. E. & Weaver, T. A. 1995, ApJS, 101, 181

Yaqoob, T. and the *ASCA* team. *ASCA* GOF Calibration Memo (ASCA-CAL-00-06-01, v1.0 06/05/00)

## Part II

# The InFOC $_{\mu}$ S Hard X-ray

## Telescope

# Chapter 5

## The InFOC $\mu$ S Hard X-ray Telescope: Pixellated CZT Detector/Shield Performance and Flight Results

### Abstract

The CZT detector on the InFOC $\mu$ S hard X-ray telescope is a pixellated solid-state device capable of imaging spectroscopy by measuring the position and energy of each incoming photon. The detector sits at the focal point of an 8 m focal length multilayered grazing incidence X-ray mirror which has significant effective area between 20–40 keV. The detector has an energy resolution of 4.0 keV at 32 keV, and the InFOC $\mu$ S telescope has an angular resolution of 2.2 arcminute and a field of view of about 10 arcminutes. InFOC $\mu$ S flew on a balloon mission in July 2001 and observed Cygnus X-1. We present results from laboratory testing of the detector to measure the uniformity of response across the detector, to determine the spectral

resolution, and to perform a simple noise decomposition. We also present a hard X-ray spectrum and image of Cygnus X-1, and measurements of the hard X-ray CZT background obtained with the SWIN detector on InFOC $\mu$ S.

## 5.1 Introduction

The International Focusing Optics Collaboration for  $\mu$ -Crab Sensitivity (InFOC $\mu$ S) is a balloon borne hard X-ray telescope for the hard X-ray bands 20–40 and 65–70 keV. InFOC $\mu$ S uses grazing incidence multilayer mirrors (Berendse et al. 2002; Ogasaka et al. 2002; Okajima et al. 2002; Owens et al. 2002) to focus astronomical photons onto a pixellated planar CdZnTe (CZT) detector.

CZT detectors are a natural fit for high energy X-ray astronomy. They have better energy resolution than scintillator detectors such as CsI or NaI, and the rather large bandgap allows us to dispense with the cryogenic cooling necessary for Ge detectors. The high atomic number of the CZT constituents provides a large cross section for photoelectric interaction with photons, allowing detectors to be built with small thicknesses in order to reduce sensitivity to volume dependent background components such as the particle flux in the upper atmosphere. CZT can be manufactured with pixellated contacts that allow fine spatial determination of the incoming photons, and when operated at moderate temperatures (around 0° C) the low leakage current of the CZT causes minimal noise and permits a very high sensitivity.

The complete InFOC $\mu$ S design calls for four mirrors and four focal planes. This plan allots one mirror for the low energy band of 20–40 keV, and three mirrors to cover the higher energy band 65–70 keV around the 68 keV  $^{44}\text{Ti}$  line from supernova remnants. Each of the confocal 8 meter focal length mirrors will have its own CZT

Table 5.1: InFOC $\mu$ S parameters. These numbers for the low energy mirror and detector document the details of the July 2001 science flight.

Parameter	Low Energy	High Energy
Focal Length	8.0 m	8.0 m
Bandpass	20–40 keV	65–70 keV
Number of Mirrors	1	3
Mirror Diameter	40 cm	30 cm
Effective Area	42 cm <sup>2</sup> @ 30 keV	70 cm <sup>2</sup>
Field of View	9.6 arcmin	2–3 arcmin
Angular Resolution	2.2 arcmin FWHM	1 arcmin
PSF	4 mm FWHM	2 mm FWHM
Detector Material	CdZnTe (CZT)	CZT
Detector Size	2.7×2.7×0.2 cm	
Pixel Array Size	12 × 12	
Pixel Spacing	2.1 mm	
	54 arcsec	
Active Shield	3.0 cm CsI	
Energy Resolution	4.0 keV @ 32 keV	5 keV
$\Delta E/E$	8% at 60 keV	
Threshold	18 keV	
Shield FOV	8.1°	
Background	$(2.7 \pm 1.2) \times 10^{-4}$ cts/cm <sup>2</sup> /sec/keV	

detector and shield. The design parameters for the complete InFOC $\mu$ S telescope are given in Table 5.1. The detectors on InFOC $\mu$ S have flown on two balloon flights: a June 2000 flight of only the focal plane, and the first science flight of the entire telescope in July 2001. The first science flight in July 2001 included only one mirror and detector in the low energy band; future flights will add more mirrors and detectors as they are completed. This paper concentrates on the detector performance; mirror results can be found in (Berendse et al. 2002; Ogasaka et al. 2002; Okajima et al. 2002; Owens et al. 2002). For reference, the effective area of the first

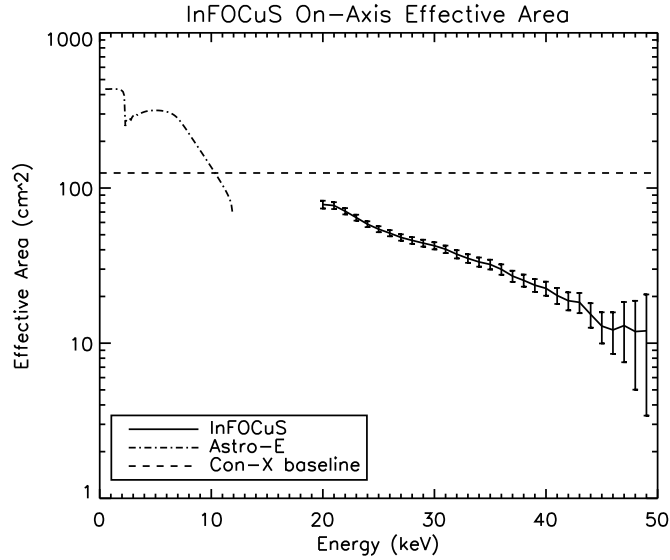


Figure 5.1: The effective area of the first InFOCuS multilayer mirror. These data come from a raster scan of a collimated X-ray tube onto the mirror and focal plane that was performed in the lab before flight (Owens et al. 2002).

InFOCuS 20–40 keV multilayer mirror is given in Figure 5.1.

With the mirror and detector performance achieved in the first science flight and projected for the high energy band we have computed a sensitivity curve for InFOCuS which we give in Figure 5.2. For this calculation, we assumed the background to be the same as measured in the 2001 flight (see Section 5.4), and present the 3 sigma continuum detection sensitivity based on an altitude of 130,000 ft ( $3.3 \text{ g cm}^{-2}$  of residual atmosphere), the measured mirror effective area given in Figure 5.1, and the parameters given in Table 5.1. We also take into account the varying atmospheric attenuation as the source moves across the sky.

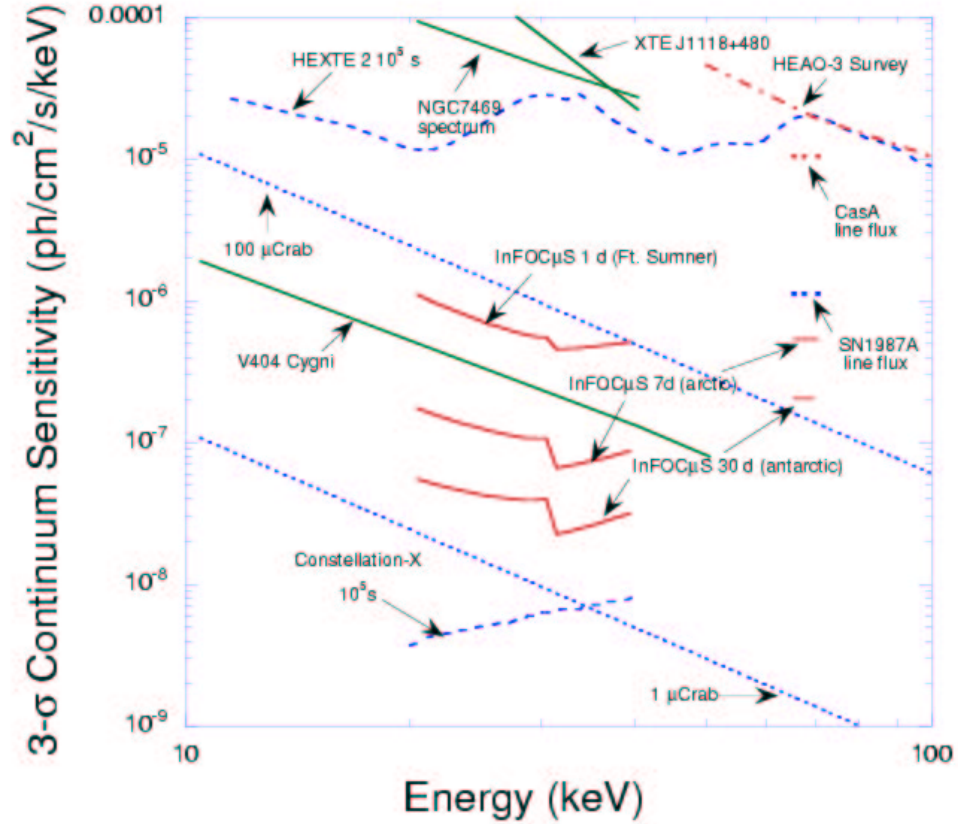


Figure 5.2: The sensitivity of the InFOC $\mu$ S telescope. The assumptions made in the calculation are presented in the text. The different InFOC $\mu$ S lines refer to different length balloon missions. For comparison, we have included some typical source spectra and the sensitivity limits for other telescopes.

## 5.2 Focal Plane

The active components of the InFOC $\mu$ S focal plane consist of a  $2.7 \text{ cm} \times 2.7 \text{ cm} \times 0.2 \text{ cm}$  piece of CZT, and a 3 cm thick CsI anticoincidence shield. The CZT detector is configured with a planar Pt contact on one of the large faces, and a  $12 \times 12$  segmented array of contacts on the opposite face delineating the detector pixels. The pixels are 2.0 mm square, and are placed on 2.1 mm centers. The detector is mounted on the top of a 4 cm cube of aluminum that serves as a base for the detector and its associated electronics, and as a coldfinger to connect the detector

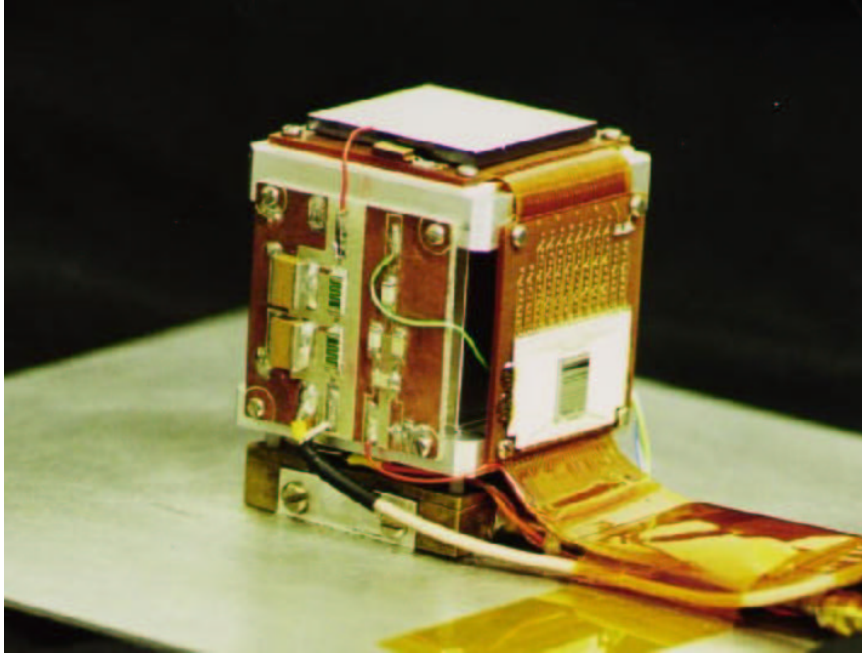


Figure 5.3: The InFOC $\mu$ S detector cube assembly. The 2.7 cm square CZT detector is the thin slab on top of the cube. The bias HV supply is filtered by the components on the nearest side panel and connected to the detector by the small wire leading to the top of the cube. The XA-1 ASIC is visible mounted on a white ceramic board on the right panel of the cube just above the ribbon cable leading to the readout electronics. The long trace length between the CZT and the ASIC adds to the input capacitance and is the leading contributor to the electronics noise that limits the energy resolution.

to a thermoelectric cooler and liquid heat exchanger. A photograph of the detector cube assembly is shown in Figure 5.3.

The detector is connected with conductive epoxy dots under each pixel to traces on a PC board that route the detector signals through a semi-rigid flex cable and onto a separate circuit board on the side of the cube. This circuit board contains the decoupling capacitors and bleed off resistors for each pixel, a ceramic fan-in assembly, and an XA-1 ASIC. The filter circuitry for the detector bias voltage is located on a separate side panel of the cube. The detector bias voltage is applied so that the top planar contact acts as the cathode and the pixels as anodes. The operating voltage is typically  $-200$  volts applied to the cathode, leaving the pixels

and the ASIC inputs at ground potential.

The XA-1 ASIC we use is the same one used in the *Swift* BAT detector, and accepts 128 input channels. (Four pixels in each corner of the  $12 \times 12$  detector pixel array are left unconnected in order to arrive at 128 input signals for the XA-1.) The ASIC contains a charge sensitive preamplifier and shaping circuit for each pixel, and allows the setting of a threshold for event detection. The ASIC also contains a pulser circuit that can be routed to the inputs in order to test the response of the system.

We place the detector cube assembly in the bottom of a well of 3.0 cm thick CsI that acts as an active shield to reduce the background from particles and photons not incident along the mirror focal direction. We are able to set an operating threshold of 15 keV for the shield, and operate it as an anti-coincidence veto for signals recorded in the detector. The detector sits 32 cm behind the opening on the front surface of the shield, and sees a shield opening angle of  $8.1^\circ$ . The 15 keV threshold is sufficient to reduce contamination from high energy background components. Figure 5.4 shows a photograph of the InFOC $\mu$ S shield assembly.

### 5.3 Detector Test Results

The CZT detector program at Goddard has tested several designs for a CZT-ASIC combination. All of them are designed around the same size piece of CZT,  $2.7 \text{ cm} \times 2.7 \text{ cm} \times 0.2 \text{ cm}$ . We were able to achieve these large dimensions for our detector with the aid of IR scanning and X-ray screening techniques that allowed us to examine CZT wafers in order to find large homogeneous pieces without defects (Parker et al. 1999; Parker et a. 2001).

The first generation detector system tested at Goddard was based on a University

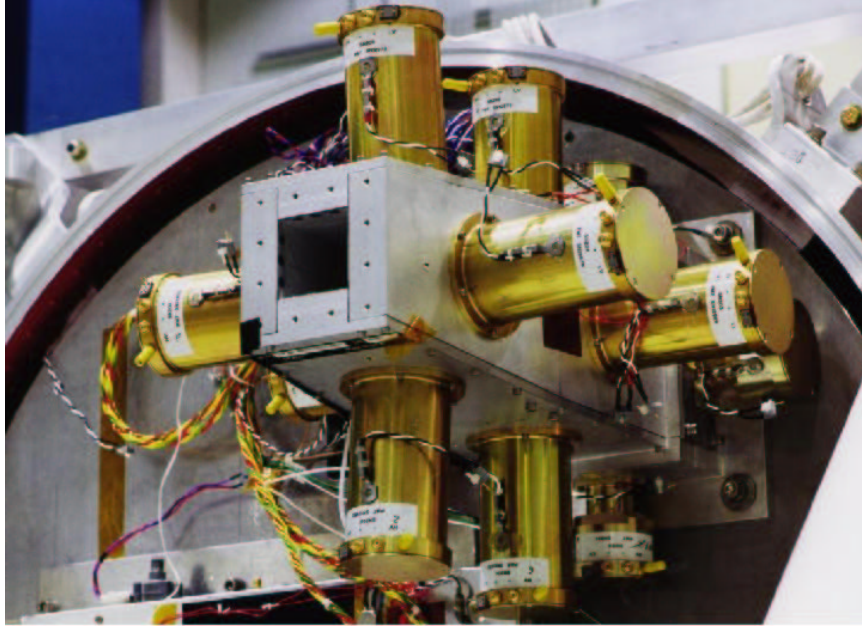


Figure 5.4: The InFOC $\mu$ S active shield. The detector cube sits in the bottom of the square well formed by the 3 cm thick CsI scintillator. The cylinders projecting from the shield contain the photomultiplier tubes used to form the veto signal.

of Arizona ASIC designed for medical imaging. This ASIC utilized an integrating amplifier mechanism which read out every pixel each readout cycle, had a  $64 \times 64$  array of  $380 \mu\text{m}$  pixels, and was constructed so that the CZT detector could be directly connected to the ASIC using indium bump bonding. With this detector we achieved an energy resolution of 2.3 keV FWHM for the 22 keV  $^{109}\text{Cd}$  line (Figure 5.5), but the ASIC readout mechanism had an unacceptable deadtime for astronomical applications. The main advantage of the UA detector was the excellent energy resolution that came from the small pixel effect<sup>1</sup> and the low input capacitance inherent to the bump bonding technique.

---

<sup>1</sup>The small pixel effect is a geometry dependent effect present in pixellated planar detectors that have pixel sizes small compared to the detector thickness. The effect allows for increased spectral resolution because most of the signal is generated by high mobility electrons instead of low mobility holes.

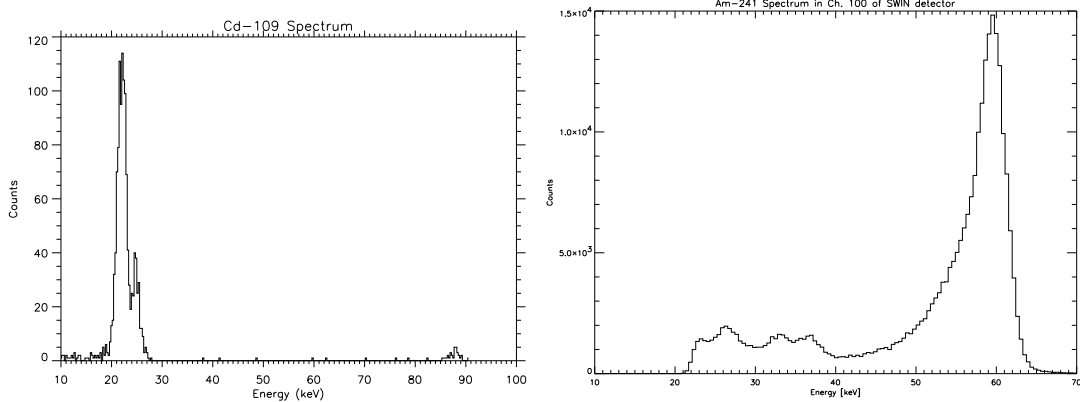


Figure 5.5: Single pixel CZT spectra. The left panel is a  $^{109}\text{Cd}$  spectrum from the University of Arizona detector. The source was collimated to shine onto the center of a  $380\ \mu\text{m}$  pixel. The detector was 2 mm thick, and operated at  $0^\circ\text{C}$  with a bias of  $-200$  volts. The resolution at the 22 keV line is 2.3 keV FWHM. The right panel is an  $^{241}\text{Am}$  spectrum from the flight SWIN detector. The detector was flood illuminated, and a representative pixel chosen. The resolution at the 60 keV line is 4.8 keV FWHM.

The second generation detector developed at Goddard was based on an ASIC that used a sparse readout mechanism. Like the UA detector, it also was an integrating ASIC meant to be directly bump bonded to a CZT detector with small pixels. The sparse readout mechanism was designed to only read out those pixels with events by comparing the pixel signals to a set of hold capacitors storing a bias frame. Unfortunately, the Mitel foundry  $3\ \mu\text{m}$  process used in the ASIC construction was unable to produce a matched set of hold capacitors for each pixel that allowed a suitable triggering mechanism to be implemented. More troubling, the digital switching signals in the ASIC easily coupled through the CZT into the inputs, severely increasing noise and reducing the energy resolution achievable with this design. The switching signals also coupled onto the top side cathode signal, degrading it and preventing us from using it as an event trigger.

The third detector design tested at Goddard was a fallback plan based on the design for the *Swift* BAT CZT detector, and was called the SWIN detector (for

*Swift*-InFOC $\mu$ S). This is the detector design that was flown on the balloon flights. The XA-1 is not an integrating ASIC, and uses the more conventional design of a charge sensitive preamplifier and shaping stages before a discriminator to detect events above a preset threshold. The SWIN detector also differs from the previous detectors in that the CZT is not directly bump bonded to the ASIC; in SWIN, the signal is routed from the CZT to the ASIC via traces on a circuit board and a fan-in assembly. Also, the XA-1 ASIC has only 128 channels, so the pixel size was increased from 380  $\mu$ m to 2.0 mm in order to match the number of pixels to the number of ASIC channels. A 2.0 mm pixel still oversamples the 4.0 mm PSF of the mirror, but no longer benefits from the small pixel effect.

We measured the SWIN detector for uniformity of response among the pixels and for gain and offset determination by flood illuminating the detector with a  $^{133}\text{Ba}$  source. Test data for the SWIN detector taken under flight-like conditions ( $T = 10^\circ\text{C}$  and bias voltage =  $-200$  volts) are given in Figure 5.6. Flood illumination data show that the SWIN detector response is rather uniform across the face of the CZT. About 10% of the pixels suffer from low gain or very high noise. The position of these pixels is not coincident with any known defects in the crystal found by imaging with an IR scan. Since most of these pixels are adjacent to each other on the detector, we conclude that they are shorted pixels caused by spreading of the conductive epoxy dots joining the CZT to the carrier board. Tests with a collimated source confirm this conclusion. This problem does not significantly affect the telescope performance because the central part of the pixel array at the focus of the mirror is relatively free of shorted pixels.

The spectral resolution of an average pixel in the SWIN detector under flood illumination at the 60 keV  $^{241}\text{Am}$  line is 4.8 keV (Figure 5.5). The overall leakage current of the entire detector under flight conditions is about 20 nA. The measured

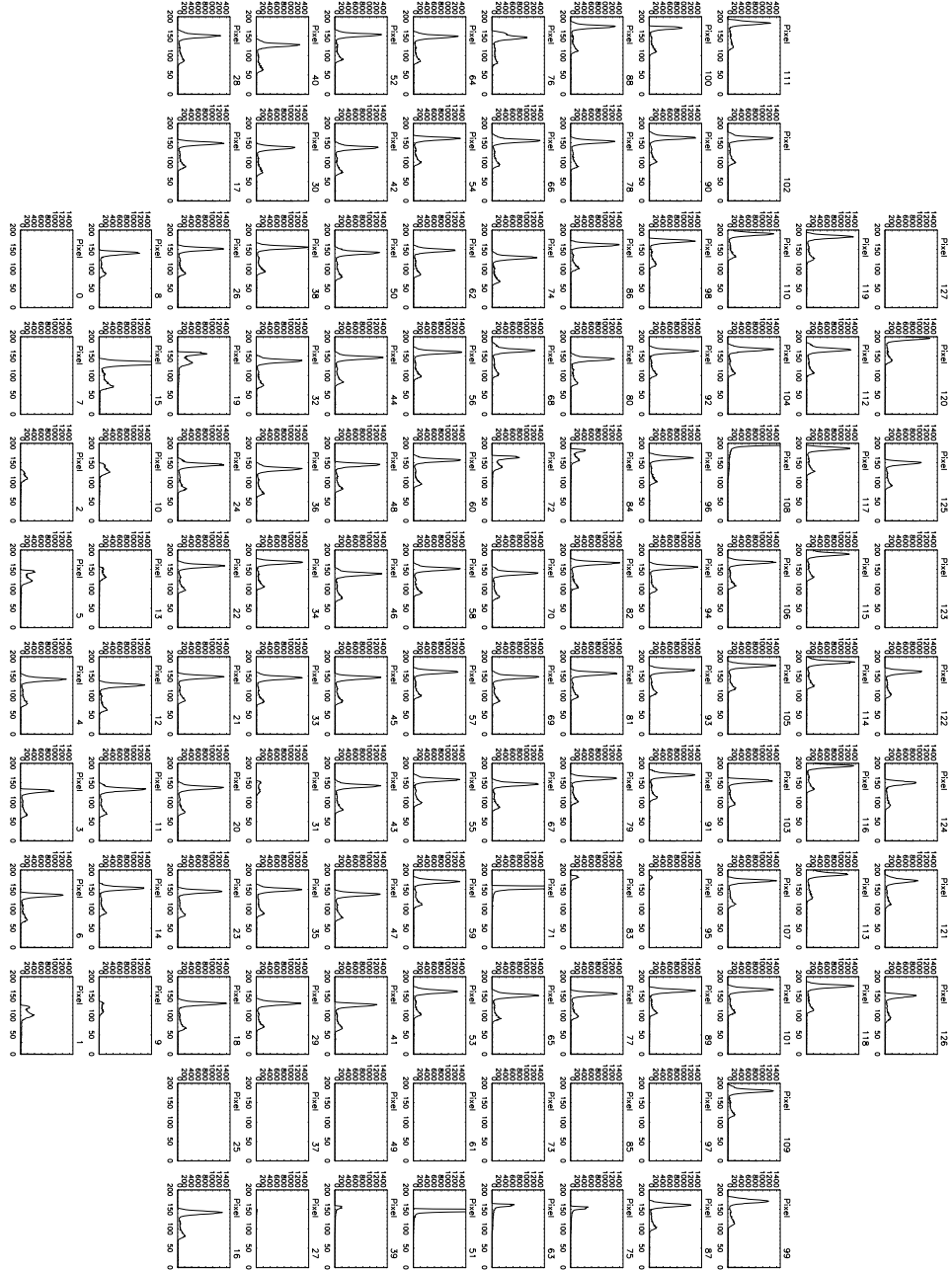


Figure 5.6:  $^{133}\text{Ba}$  spectra in the SWIN detector. There is one graph for each pixel of the detector. The vertical axes are counts, and the horizontal axes are detector channel number and are related to the event energy. This data was produced by flood illuminating the detector with the  $^{133}\text{Ba}$  source, and are similar to that used to calibrate the gain and offset of the detector. The data organized in this form are an end to end demonstration of the operation of the entire focal plane and make it easy to locate bad pixels to be electronically masked off in flight. (The pixels without spectra in this figure are pixels that have already been masked). Bad pixels were usually the result of shorting caused by a spreading of the conductive epoxy used to connect the detector to the carrier board.

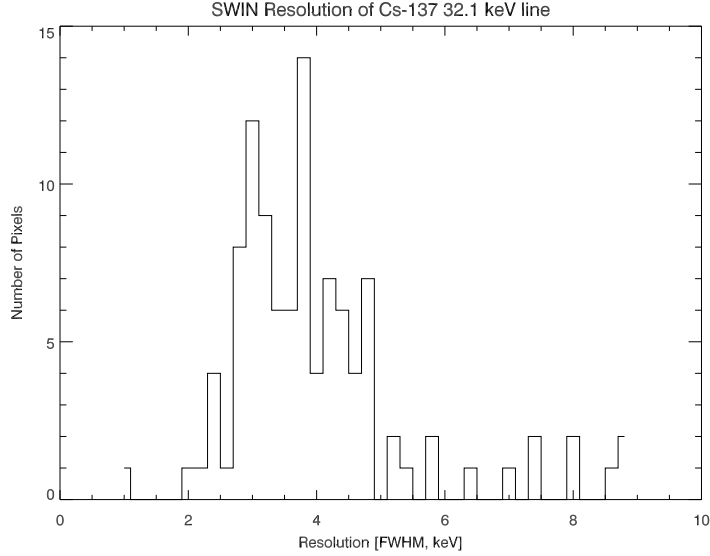


Figure 5.7: A histogram of the FWHM energy resolution of the SWIN detector pixels at the  $^{137}\text{Cs}$  32.1 keV line.

resolution of the SWIN detector at the  $^{137}\text{Cs}$  32.1 keV line is 4.0 keV FWHM (see Figure 5.7).

With these spectral resolution measurements at two different energies, we can begin to decompose the line spread function into its different components. To first order, the line spread function is composed of an energy independent part and a component that is linearly dependent on energy:

$$\sigma^2 = \sigma_n^2 + \sigma_{cc}^2,$$

where  $\sigma$  is the measured energy resolution,  $\sigma_n$  is the constant term, and  $\sigma_{cc}$  is the energy dependent term. The constant term,  $\sigma_n$ , is primarily due to noise (such as leakage current), and the energy dependent term,  $\sigma_{cc}$ , depends heavily on the charge collection properties of the CZT material. If we take  $\sigma_{cc} = \alpha E$ , then we have

$$\sigma^2 = \sigma_n^2 + \alpha^2 E^2,$$

an equation in the two unknowns  $\sigma_n$  and  $\alpha$ . Using our two measured spectral

resolutions at 32.1 keV and 59.5 keV and eliminating  $\alpha$ , we obtain  $\sigma_n = 3.6$  keV. Solving for  $\sigma_{cc}$ , we get  $\sigma_{cc30} = 1.7$  keV at 32.1 keV and  $\sigma_{cc60} = 3.2$  keV at 59.5 keV. These numbers indicate that flat spectrum noise is the dominant contribution to the line spread function in our energy range of 20–40 keV. Incomplete charge collection in the CZT detector becomes important at higher energies, but is only a secondary factor at 30 keV.

In order to investigate the noise contribution to the line spread function, we used the internal XA-1 pulser circuit connected to the inputs of the ASIC. Pulser measurements of the ASIC alone show a line spread function of less than 1 keV, indicating that noise generated within the ASIC electronics is not the dominant component of the noise contribution. Pulser resolution measurements with the CZT detector connected to the ASIC inputs are consistent with measurements taken with a radioactive source, indicating that the dominant source of noise contributing to the energy independent noise term is external to the ASIC and comes from the detector and its circuitry. We varied the temperature of the detector/ASIC and the bias voltage to investigate the effects of leakage current on the line spread function and find that the leakage current component of the noise is not a dominant contribution. The most likely cause of the high noise term is the high input capacitance caused by the long lead lengths connecting the pixels to the ASIC.

## 5.4 Flight Results

### 5.4.1 The August 2000 Focal Plane Test Flight

In August 2000, we took InFOC $\mu$ S to Palestine, Texas to fly the detector at the National Scientific Balloon Facility. The main purpose of the flight was to test our detector at float altitudes to determine the count rate from the particle background,

and the effectiveness of our anti-coincidence shield system. This measurement was a key parameter in the determination of the sensitivity of the instrument. No mirror was present, and no astronomical objects were observed. Also flying on this test flight were two BAT detectors from the *Swift* mission that were being checked for similar reasons. Another main goal of the flight was to check other flight systems in a realistic environment.

The balloon was launched on August 29, flew for seven hours at 118,000 ft, and was successful in measuring a relatively flat CZT background in flight of  $(7.1 \pm 3.5) \times 10^{-4}$  cts sec<sup>-1</sup> cm<sup>-2</sup> keV<sup>-1</sup>.

### 5.4.2 July 2001 Science Flight

In July, 2001 InFOC $\mu$ S flew its first science flight from with a complete mirror and detector system from Palestine, Texas. This flight achieved three hours at float altitude and allowed InFOC $\mu$ S to become the first telescope to utilize a multilayer mirror and detect an astronomical source using CZT detectors.

#### Cygnus X-1 results

During the July 2001 science flight, the pointing system failed to achieve the necessary one arcminute pointing to track a source. InFOC $\mu$ S concentrated on obtaining as many photons as possible from the bright source Cyg X-1. Analysis of the attitude data after the flight showed stochastic long time scale 30–45 arcminute pointing errors probably caused by turbulence and wind shifts in the upper atmosphere. Figure 5.8 shows the lightcurve for a two hour observation of Cyg X-1, and indicates several high count rate periods when we detected Cyg X-1 when the pointing was momentarily good.

Figure 5.9 shows the spectrum extracted from these high count rate times and

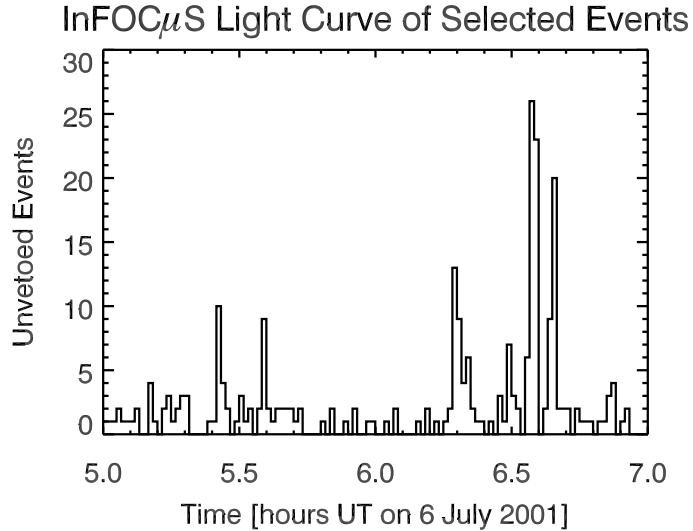


Figure 5.8: The InFOC $\mu$ S Cyg X-1 light curve. The data is binned in one minute intervals. The low level of background is evident, as well as peaks when the pointing coincided with the position of the source. If the pointing had been on target at all times, we would have received about 80 counts per minute from Cyg X-1.

confirms the detection of Cyg X-1. The peak indicated in the spectrum between 30–50 keV falls in the approximate location of the mirror bandpass, trails off at low energy as would a continuum source attenuated by the atmosphere, and also falls at high energies as the effective area of the mirror decreases. The apparent mismatch between the 20–60 keV width of the peak and the 20–40 keV mirror bandpass is due to ASIC offset drift that could not be calibrated because of a defective inflight pulser system. The actual calibration used is based on the best available ground calibration with radioactive sources. Figure 5.9 also shows an image of the photons detected during these high count rate times derived from post-flight attitude reconstructed data convolved with the telescope PSF.

We also used the exposure corrected image to determine the flux of Cyg X-1. Starting from the exposure corrected image, we subtracted the background rate to

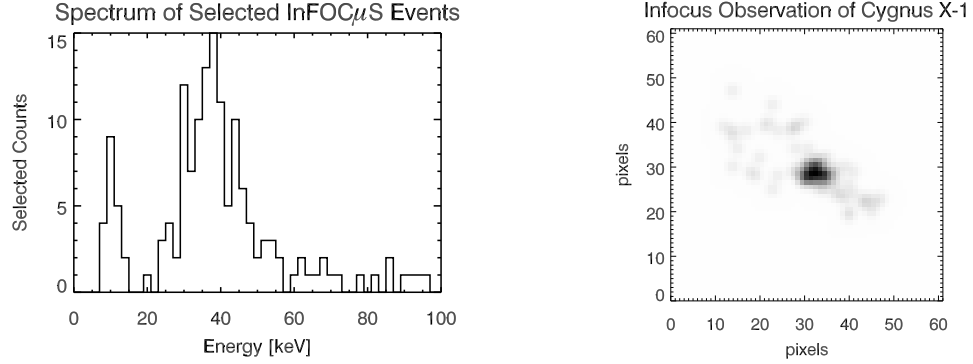


Figure 5.9: The InFOC $\mu$ S astronomical results. The left panel shows the Cyg X-1 spectrum. The peak centered at about 30 keV matches very well to our pre-flight predictions of the Cyg X-1 spectrum. The small peak below 20 keV results from noise below the detector threshold. The energy scale could only be roughly calibrated to laboratory data because of the failure of the in-flight pulsar calibration mechanism. The right panel shows the InFOC $\mu$ S Cyg X-1 image. Each detector pixel is 54 arcseconds. The image was made by using gyro and star camera data to determine the aspect of the telescope for each photon detected within the bandpass of the mirror during periods when the Cyg X-1 count rate was high. The photon map was divided by the exposure map and then convolved with the 2 arcminute HPD of the telescope PSF. The peak of the exposure map indicates about 80 seconds on the location of Cygnus X-1.

obtain the observed Cyg X-1 count rate in the 20–40 keV band. We then folded the Cyg X-1 spectrum given by Doberiner et al. (1995) through our model atmosphere ( $3.3 \text{ g cm}^{-2}$  and an elevation of  $75^\circ$ ) and measured mirror effective area to obtain the model count rate. The ratio of the count rates multiplied by the model flux gives us our observed flux of  $4.9 \times 10^{-9} \text{ ergs sec}^{-1} \text{ cm}^{-2}$ . This value is in good agreement with the Doberiner *HEXE* result of  $6.48 \times 10^{-9} \text{ ergs sec}^{-1} \text{ cm}^{-2}$  given the known variability of Cyg X-1.

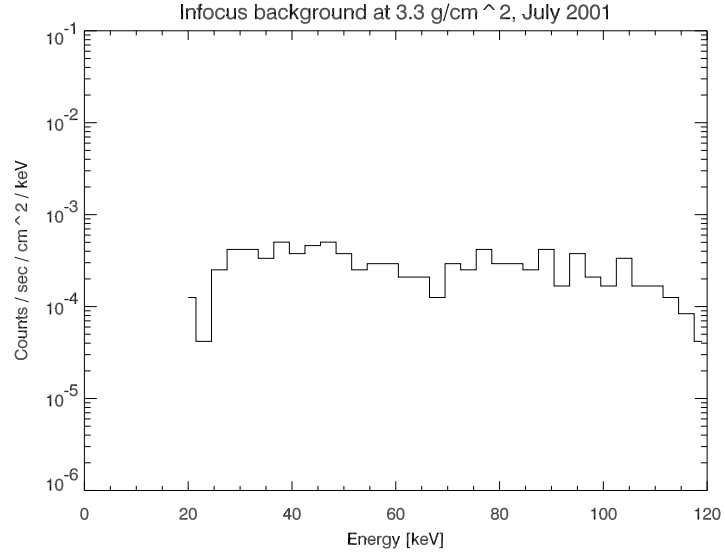


Figure 5.10: InFOCUS background spectrum. This spectrum was measured using the InFOCUS SWIN detector during the science flight of July 2001 from Palestine, Texas during times when we were not observing an astrophysical source. The balloon altitude was 130,000 ft and the shield threshold was set at 15 keV. The spectrum is well characterized by the value  $(2.7 \pm 1.2) \times 10^{-4}$  cts  $\text{sec}^{-1} \text{cm}^{-2} \text{keV}^{-1}$  in the band from 20–120 keV.

### Inflight background

The other principal goal of the flight was to measure the background for the CZT detectors in order to determine the sensitivity of InFOCUS in future flights, to verify the measurement made in the test flight of 2000, and to demonstrate the suitability of our active CsI shield. Figure 5.10 shows the InFOCUS detector background determined in July 2001. The measured background from a two hour observation is rather flat from 20–120 keV, and lies at  $(2.7 \pm 1.2) \times 10^{-4}$  cts  $\text{sec}^{-1} \text{cm}^{-2} \text{keV}^{-1}$ . This number was determined by taking the spectrum in Figure 5.10 and computing the average and variance of the background level in all the 3 keV wide bins between 20–120 keV. The somewhat high uncertainty is mostly statistical and comes from the fact that even with a two hour observation we have very few photons ( $\sim 10$ ) in

each bin.

This measurement was taken at float altitude of 130,000 ft without using any depth determination techniques to further reduce the background. This measurement gives a lower background than the test flight measurement, but we are more confident of the lower value because the test flight background spectrum was slightly contaminated by interference noise in some of the pixels. We have carefully measured the deadtime in the detector, and find that the largest contribution (from the shield veto) gives less than 1.5% deadtime. The correct measurement of the Cygnus X-1 flux (Section 5.4.2) verifies that the signal chain is operating correctly and does not suffer from any deadtime effects that could affect the background level.

Rothschild et al. (1999) and Slavis et al. (1999) show that the dominant CZT background components are uniformly distributed in the volume of the CZT detector and that depth determination techniques can reduce the background level by a factor of seven. If we apply their factor of seven to our uncorrected measured results, the InFOC $\mu$ S background is the lowest CZT background yet measured. These results indicate that a heavy active shield operated with a low threshold in conjunction with a depth determination algorithm are both necessary to achieve the lowest possible CZT background levels and the best instrument sensitivity.

## 5.5 Conclusions and Future Plans

The InFOC $\mu$ S telescope has demonstrated the effectiveness of a CZT detector coupled to a multilayer mirror for hard X-ray astronomy. The moderate resolution SWIN detector has become the first CZT detector to observe astrophysical photons, and our heavy CsI shielding has enabled us to achieve a very low in flight background. The InFOC $\mu$ S implementation needs improvements in the pointing system

before it can do high precision astronomy, but the new technology behind the mirror and detector have proven sound. Even with an on target observation time of only about a minute, we have detected the astrophysical source Cyg X-1 with very high significance.

### 5.5.1 Detector Improvements

Our laboratory and flight experience with the SWIN CZT detector and the InFOC $\mu$ S telescope have given us valuable experience to direct future improvements. The most important goal is to improve the spectral resolution of the detector. Our plans for the next generation InFOC $\mu$ S detector will have an improved layout that will reduce input capacitance by shortening the lead length between the CZT and ASIC. Reducing the pixel size and adding steering electrodes will improve charge collection, also improving the energy resolution. Another possibility for reducing the input capacitance is to remove the decoupling capacitors between the CZT and ASIC. This requires a very low leakage current, but this can be achieved by running the detector much colder. Takahashi et al. (1999) have shown improved energy resolution in CZT detectors by operating at a very high voltage in order to improve charge collection. This also requires very low temperatures in order to minimize the leakage current, but our detector temperature regulation system is able to go down to  $-25^\circ$  without modification, and colder with some minor hardware changes.

New ASICs are another important step towards improving energy resolution. We are currently designing a custom ASIC specifically for our detector configuration that should not be as sensitive to input capacitance effects. Also, a newer generation of XA-1 ASIC has been developed with much improved temperature stability that will significantly reduce our susceptibility to offset drifts. This ASIC is being used in the *Swift* BAT flight detectors, and will be tested for future InFOC $\mu$ S detectors.

Other groups have shown the importance of using a depth determination mechanism to achieve the lowest detector background and best sensitivity. We have been experimenting with two different techniques, one based on utilizing the cathode signal and another based on using the measured charge spreading in neighboring small pixels to determine the depth of interaction. The cathode signal method is simpler to operate but more difficult to implement since the cathode signal has an inherently worse resolution because most of its signal is generated by holes. A possible solution to this problem is to segment the cathode electrode into strips, lowering the capacitance and improving the resolution so that the cathode signal can be used.

Marks (2000) has shown in his Ph.D. thesis that determining the photon depth of interaction by observing the signal in the neighboring pixels is possible. However, this is also difficult in practice because of the computational complexity, and because it requires the neighboring pixel signals. More recent versions of the XA-1 ASIC than the one used in SWIN have this capability, and we will explore this method for background rejection.

## 5.5.2 Future Flight Plans

The most important enhancement to the InFOC $\mu$ S platform will be to improve the pointing system to allow long-term stable pointing at the one arcminute level. Our flight experience has given us valuable data on high-altitude winds and turbulence that will be incorporated into a future design utilizing more robust pointing mechanisms with a larger dynamic range.

Future flights of InFOC $\mu$ S will also fly more advanced technology as it becomes available. The Nagoya group is working on a second low-energy multilayer mirror that will have improved performance and will fly on the next flight. Future flights are planned to include the high-energy mirrors for  $^{44}\text{Ti}$  studies of supernovae remnants.

Each of these planned future flights will use an improved CZT detector based on the knowledge we have gained with the SWIN detector and incorporating the changes mentioned above.

## **Acknowledgements**

We would like to thank the NSBF flight crew for all their help and for a successful flight. We would also like to especially thank Chris Miller, Steve Derdeyn, Kiran Patel, Steve Snodgrass, Holly Hancock and all the dedicated Goddard engineers and technicians whose hard work and countless extra hours made InFOC $\mu$ S possible.

# Bibliography

- F. Berendse et al., “Production and Performance of the Infocus 20-40 keV Graded Multilayer Mirror,” *Applied optics*, submitted, 2002.
- Y. Ogasaka et al., “Supermirror hard X-ray telescope and the results of first observation flight of Infocus,” in *X-Ray and Gamma-Ray Telescopes and Instruments for Astronomy*, J. Truemper, H. Tannanbaum, eds., *Proc. SPIE* **4851**, these proceedings, 2002.
- T. Okajima et al., “Characterization of the supermirror hard X-ray telescope for the Infocus balloon experiment,” *Applied optics*, in press, 2002.
- S. Owens et al., “Characterization and performance of the Infocus 20-40 keV X-ray focusing mirror,” in *X-Ray Optics for Astronomy: Telescopes, Multilayers, Spectrometers, and Missions*, P. Gorenstein; R. Hoover, eds., *Proc. SPIE* **4496**, p. 115–126, 2002.
- B. Parker et al., “Correlation between bulk material defects and spectroscopic response in cadmium zinc telluride detectors,” in *Hard X-Ray, Gamma-Ray, and Neutron Detector Physics*, R. James, R. Schirato, eds., *Proc. SPIE* **3768**, p. 129–137, 1999.
- B. Parker et al., “Effect of twin boundaries on the spectroscopic performance of CdZnTe detectors,” in *Hard X-Ray and Gamma-Ray Detector Physics III*, R. James ed., *Proc. SPIE* **4508**, p. 68–78, 2001.

- S. Dobereiner et al., “HEXE Observations of Cygnus X-1,” *Astronomy and Astrophysics* **302**, p. 115, 1995.
- R. Rothschild et al., “Actively shielded CZT focal plane detectors for the Fine Angular Resolution X-ray Imaging Telescope (FAR\_XITE),” in *EUV, X-Ray, and Gamma-Ray Instrumentation for Astronomy X*, O. Siegmund, K. Flanagan, eds., *Proc. SPIE* **3765**, p. 360–367, 1999.
- K. Slavis et al., “High-altitude balloon flight of CdZnTe detectors for high-energy x-ray astronomy: II,” in *EUV, X-Ray, and Gamma-Ray Instrumentation for Astronomy X*, O. Siegmund, K. Flanagan, eds., *Proc. SPIE* **3765**, p. 397–406, 1999.
- T. Takahashi et al., “High-resolution CdTe detector and applications to imaging devices,” in *IEEE Transactions on Nuclear Science* **48**, no. 3, p. 287, 2001.
- D. A. Marks. Ph.D. thesis. University of Arizona, 2000.
- F. Harrison et al., “Development of the High-Energy Focusing Telescope (HEFT) balloon experiment,” in *X-ray Optics, Instruments, and Missions III*, J. Truemper, B. Aschenbach, eds., *Proc. SPIE* **4012**, p. 693, 2000.
- P. Bloser et al., “Balloon flight background measurement with actively-shielded planar and imaging CZT detectors,” in *X-Ray and Gamma-Ray Instrumentation for Astronomy XII*, K. Flanagan, O. Siegmund; eds., *Proc. SPIE* **4497**, p. 88, 2002.

# Chapter 6

## Summary and Conclusions

This dissertation has presented new results on the galactic oxygen abundance and on elemental abundances in galaxy clusters. It has also described the development and performance of a new type of solid-state detector for hard X-ray astronomy in the 10–150 keV band and the results of the first science flight of the InFOC $\mu$ S X-ray telescope using this new CZT detector. The notable results from this research are summarized below.

### 6.1 Galactic ISM Oxygen Abundance

Chapter 3 details an investigation into the galactic ISM using the *XMM-Newton* X-ray telescope. *XMM-Newton* is the first X-ray observatory with sufficient collecting area and spectral resolution to allow an investigation of the galactic ISM with CCD observations of the absorption edge from photoionization of the K-shell of oxygen at 542 eV. For moderate to high column densities in our galaxy ( $n_H \approx 1.0 \times 10^{21} \text{ cm}^{-2}$ ) corresponding to observations near but not directly in the galactic plane, the optical depth of the oxygen K-edge is about unity, making it ideal for measurements of the oxygen elemental abundance. X-ray measurements of the oxygen abundance from

the K-edge have the advantage of being sensitive to all forms and ionization states of oxygen, including gas, dust, and molecules.

We observed eleven galaxy clusters chosen to have high X-ray fluxes and  $n_H$  in the range for a good oxygen measurement. Clusters were chosen as the background source for the absorption measurements because of their relatively simple and featureless spectra, abundant X-ray flux, and because of their lack of variability. For each cluster we measured the X-ray galactic hydrogen column ( $n_H$ ) and oxygen abundance. We have found that:

- The X-ray derived galactic hydrogen columns above  $n_H \approx 0.5 \times 10^{21} \text{ cm}^{-2}$  are higher than the corresponding total hydrogen columns from 21 cm measurements. Above  $n_H \approx 1.0 \times 10^{21} \text{ cm}^{-2}$ , the X-ray equivalent hydrogen column is 1.5–2.5 times the 21 cm values. This is in agreement with the results of Arabadjis & Bregman (1999) and indicates that molecular hydrogen plays an important part in the total hydrogen absorption at high columns.
- A comparison of the X-ray derived molecular hydrogen component of the ISM to CO derived observations of galactic  $\text{H}_2$  for two lines of sight show that they are in good agreement.
- The observed X-ray oxygen abundance derived from the K-edge absorption is 0.9 times the most recent solar values. This result indicates that depletion of oxygen in the ISM is not occurring at the high level previously believed.
- The ISM oxygen abundance is found to be nearly uniform across our eleven lines of sight. These eleven lines of sight span an order of magnitude in total hydrogen column  $n_{H_X}$ . Since we have found that high X-ray  $n_{H_X}$  is associated with  $\text{H}_2$  which is preferentially found in clouds, this result suggests that the galactic oxygen abundance does not depend on ISM density. This would mean

that the oxygen abundance is the same in dense clouds and in the more diffuse parts of the ISM.

## 6.2 Elemental Abundances in Galaxy Clusters

Chapter 4 presents measurements of the average elemental abundances of over 300 galaxy clusters observed by *ASCA*. By using a joint fitting technique to simultaneously analyze clusters with similar temperatures (masses) and metallicities we obtained the most precise measurements of the cluster abundances of the elements iron, silicon, sulfur, calcium, argon, and nickel. X-ray abundance measurements offer some of the same advantages outlined in the previous section, providing a clean and easily understood measurement uncomplicated by non-thermal conditions, ionization corrections and radiative transfer problems.

Galaxy clusters are a unique environment in that all metals produced by the star formation throughout the cluster history are retained in the deep cluster potential. This is in contrast to the case in galaxies, where winds from supernovae and external pressures such as ram pressure stripping can remove metals. Thus, measurements of elemental abundances in the cluster ICM present a unique opportunity to examine the integrated history of star formation in a closed environment. Because of this, a comparison of the abundances and abundance ratios in the ICM can be made with the yields of SN Ia and SN II.

We present the results from this investigation below:

- Galaxy cluster iron abundances average about 0.4 times current solar values. The iron abundance is the same for clusters above 3 keV, but the abundance peaks for cluster with temperatures about 1-2 keV. This is thought to be a contribution from SN Ia products from the central cD galaxy in many clusters.

This allows the metals associated with the central galaxy to make more of a contribution to the total iron abundance than in higher temperature ( $T > 3$  keV), more massive clusters where more of the metals lie in the outer layers. Below 1 keV, the iron abundance falls off rapidly. This is thought to be a result of these small galaxy groups' lesser gravitational potential being unable to hold on to all the metals produced and expelled by member galaxies.

- As mentioned above the metallicity of clusters is fairly constant above 3 keV. This is evidence against ram pressure stripping as the dominant mechanism for transporting metals from galaxies into the ICM. Ram pressure stripping is much more efficient at higher densities, so if it were the dominant transport mechanism we would expect to see higher metallicities at higher cluster masses.
- Silicon, sulfur, calcium and argon are all considered  $\alpha$ -elements, or elements formed by adding successive  $\alpha$ -particles to oxygen nuclei. This similar production mechanism has led to the prediction that these elements should have similar abundances. We find that this is not the case. Silicon is generally overabundant with respect to iron in clusters, and sulfur slightly underabundant. Argon and calcium are not detected at all. These are widely varying abundances for the separate  $\alpha$ -elements. Further, the silicon abundance increases in higher mass clusters while the sulfur abundance falls off. We conclude that the  $\alpha$ -elements are not produced homogeneously as a single class.
- A comparison of our measured abundance ratios  $[\text{Si}/\text{Fe}]$  and  $[\text{S}/\text{Fe}]$  with theoretical predictions for a mix of SN Ia and SN II shows that no mix of these supernovae products can account for the abundance ratios we measure. An additional source of metals is needed.
- The general trend is for higher mass clusters to have more of their metals

produced by SN II than by SN Ia.

- This additional source of metals is most likely from very high mass, low metallicity progenitor stars. Yields from theoretical models of population III type stars produce elements in the ratios needed to account for our observational results.

### 6.3 The InFOC $\mu$ S Hard X-ray Telescope and its CZT Detectors

The InFOC $\mu$ S hard X-ray telescope is one of the first in the class of hard X-ray (10–100 keV) telescopes. The hard X-ray band is where thermal emission starts to become less dominant as a source of astrophysical emission and underlying non-thermal emission can be studied. InFOC $\mu$ S utilizes focusing optics by employing multi-layer coatings on grazing incidence optics in order to improve reflectivity at hard X-ray energies. The use of focusing optics allows the use of much smaller detectors and eliminates most of the particle background that limits sensitivity at these energies. Just as important is the ability to form true images.

The InFOC $\mu$ S telescope uses CZT detectors at the focal plane. CZT is well suited for hard X-ray observations because of its ability to have good detection efficiency in a small volume. Also attractive is its capability of operating at warm temperatures, eliminating the need for expensive and heavy cryogenics. Our achievements with CZT and InFOC $\mu$ S include:

- The development of three generations of CZT detector arrays.
- The SWIN CZT detector flown in the 2001 science flight had a measured energy resolution of about 4.8 keV. This result is limited by our particular

arrangement of electronic components and is far short of the  $< 1$  keV inherent resolution of these detectors. However, since the mirror passband for the 2001 flight was restricted to 20–40 keV, this degraded spectral resolution does not limit InFOC $\mu$ S’s science capabilities because no spectral lines are expected in that energy band.

- The 2000 flight of the InFOC $\mu$ S focal plane measured the particle background at flight altitudes of 130,000 ft and verified the need for heavy active shielding to achieve the lowest possible background rate. This very low rate of  $(2.7 \pm 1.2) \times 10^{-4}$  cts cm<sup>2</sup> sec<sup>-1</sup> keV<sup>-1</sup> is the best yet reported for this type of instrument.
- The multi-layer optic and CZT detector flown in the 2001 science flight have proven successful and substantiated the use of these new technologies in future hard X-ray experiments such as *Constellation-X*. InFOC $\mu$ S detected the astrophysical source Cyg X-1 with high confidence and provided the first detection of astrophysical photons with CZT detectors. The pointing of the telescope suffered from stochastic long-time scale errors, but post-processing has enabled an aspect solution sufficient to significantly detect the source with only a minute of pointing on target.
- The measured Cyg X-1 flux from this observation is consistent with expectations from previous observations with other telescopes. This concordance verifies our performance expectations calculated from laboratory measurements.

# Bibliography

# Bibliography

- Abel, T., Bryan, G. L., & Norman, M. L. 2000, ApJ, 540, 39
- Abell, G. O. 1958, ApJS, 3, 211
- Allende Prieto, C., Lambert, D. L., & Asplund, M. 2001, ApJ, 556, L63
- Anders, E. & Grevesse, N. 1989, Geochim. Cosmochim. Acta, 53, 197
- André, M. K. et al. 2003, ApJ, 591, 1000
- Angelini, L., Loewenstein, M., & Mushotzky, R. F. 2001, ApJ, 557, L35
- Arabadjis, J. S. & Bregman, J. N. 1999, ApJ, 510, 806
- Arnaud, M., Rothenflug, R., Boulade, O., Vigroux, L., & Vangioni-Flam, E. 1992, A&A, 254, 49
- Arnaud, M., Neumann, D. M., Aghanim, N., Gastaud, R., Majerowicz, S., & Hughes, J. P. 2001, A&A, 365, L80
- Asplund, M., Grevesse, N., Sauval, A. J., Prieto, C. A., & Kiselman, D. 2003, ArXiv Astrophysics e-prints, astro-ph/0312290
- Becker, R. H., Smith, B. W., White, N. E., Holt, S. S., Boldt, E. A., Mushotzky, R. F., & Serlemitsos, P. J. 1979, ApJ, 234, L73
- Bell, E. F., McIntosh, D. H., Katz, N., & Weinberg, M. D. 2003, ArXiv Astrophysics e-prints, 2543
- F. Berendse et al., “Production and Performance of the Infocus 20-40 keV Graded Multilayer Mirror,” *Applied optics*, submitted, 2002.

- P. Bloser et al., “Balloon flight background measurement with actively-shielded planar and imaging CZT detectors,” in *X-Ray and Gamma-Ray Instrumentation for Astronomy XII*, K. Flanagan, O. Siegmund; eds., *Proc. SPIE* **4497**, p. 88, 2002.
- Böhringer, H. et al. 2001, *A&A*, 365, L181
- Boulanger, F., Abergel, A., Bernard, J.-P., Burton, W. B., Desert, F.-X., Hartmann, D., Lagache, G., & Puget, J.-L. 1996, *A&A*, 312, 256
- Bromm, V., Coppi, P. S., & Larson, R. B. 1999, *ApJ*, 527, L5
- Burstein, D. & Heiles, C. 1982, *AJ*, 87, 1165
- Cappellaro, E., Turatto, M., Tsvetkov, D. Y., Bartunov, O. S., Pollas, C., Evans, R., & Hamuy, M. 1997, *A&A*, 322, 431
- Cardelli, J. A., Sofia, U. J., Savage, B. D., Keenan, F. P., & Dufton, P. L. 1994, *ApJ*, 420, L29
- Cardelli, J. A., Meyer, D. M., Jura, M., & Savage, B. D. 1996, *ApJ*, 467, 334
- Cartledge, S. I. B., Meyer, D. M., Lauroesch, J. T., & Sofia, U. J. 2001, *ApJ*, 562, 394
- Cavaliere, A. & Fusco-Femiano, R. 1976, *A&A*, 49, 137
- Crinklaw, G., Federman, S. R., & Joseph, C. L. 1994, *ApJ*, 424, 748
- DeGrandi, S. 2003 in proceedings of the Ringberg Cluster Conference
- Dame, T. M., Hartmann, D., & Thaddeus, P. 2001, *ApJ*, 547, 792
- Deharveng, L., Peña, M., Caplan, J., & Costero, R. 2000, *MNRAS*, 311, 329
- Dickey, J. M. & Lockman, F. J. 1990, *ARA&A*, 28, 215
- S. Dobereiner et al., “HEXE Observations of Cygnus X-1,” *Astronomy and Astrophysics* **302**, p. 115, 1995.
- Draine, B. T. 2003, ArXiv Astrophysics e-prints, astro-ph/0312592
- Dupke, R. A. & Arnaud, K. A. 2001, *ApJ*, 548, 141

- Dupke, R. A. & White, R. E. 2000a, ApJ, 528, 139
- Dupke, R. A. & White, R. E. 2000b, ApJ, 537, 123
- Federman, S. R., Glassgold, A. E., & Kwan, J. 1979, ApJ, 227, 466
- Finoguenov, A., Matsushita, K., Böhringer, H., Ikebe, Y., & Arnaud, M. 2002, A&A, 381, 21
- Finoguenov, A., Arnaud, M., & David, L. P. 2001, ApJ, 555, 191
- Finoguenov, A., David, L. P., & Ponman, T. J. 2000, ApJ, 544, 188
- Fitzpatrick, E. L. 1996, ApJ, 473, L55
- Fukazawa, Y. 1997, Ph.D. Dissertation, University of Tokyo
- Fukazawa, Y., Makishima, K., Tamura, T., Ezawa, H., Xu, H., Ikebe, Y., Kikuchi, K., & Ohashi, T. 1998, PASJ, 50, 187
- Gastaldello, F. & Molendi, S. 2002, ApJ, 572, 160
- Gibson, B. K., Loewenstein, M., & Mushotzky, R. F. 1997, MNRAS, 290, 623
- Grevesse, N. & Sauval, A. J. 1998, Space Science Reviews, 85, 161
- Grevesse, N. & Sauval, A. J. 1999, A&A, 347, 348
- Guainazzi, M. & Molendi, S. 1999, A&A, 351, L19
- Haffner, L. M., Reynolds, R. J., Tufte, S. L., Madsen, G. J., Jaehnig, K. P., & Percival, J. W. 2003, ApJS, 149, 405
- F. Harrison et al., “Development of the High-Energy Focusing Telescope (HEFT) balloon experiment,” in *X-ray Optics, Instruments, and Missions III*, J. Truemper, B. Aschenbach, eds., *Proc. SPIE* **4012**, p. 693, 2000.
- Heger, A. & Woosley, S. E. 2002, ApJ, 567, 532
- Henry, R. B. C., & Worthey, G. 1999, PASP, 111, 119
- Henry, R. B. C., Kwitter, K. B., & Balick, B. 2004, ArXiv Astrophysics e-prints, astro-ph/0401156
- Holweger, H. 2001, AIP Conf. Proc. 598: Joint SOHO/ACE workshop ”Solar and

- Galactic Composition”, 598, 23
- Horner, D. J., Baumgartner, W. H., Gendreau, K. C., & Mushotzky, R. F. 2003, ApJS, submitted
- Horner, D. 2001, Ph.D. Dissertation, Department of Astronomy, University of Maryland College Park
- Hwang, U., Mushotzky, R. F., Burns, J. O., Fukazawa, Y., & White, R. A. 1999, ApJ, 516, 604
- Irwin, J. A., Athey, A. E., & Bregman, J. N. 2003, ApJ, 587, 356
- Ishimaru, Y. & Arimoto, N. 1997, PASJ, 49, 1
- Jenkins, E. B. 1987, ASSL Vol. 134: Interstellar Processes, 533
- Jenkins, E. B. 2003, ArXiv Astrophysics e-prints, 9651
- Jensen, A. G., Rachford, B. L., & Snow, T. P. 2003, American Astronomical Society Meeting, 203,
- Juett, A. M., Schulz, N. S., & Chakrabarty, D. 2003, ArXiv Astrophysics e-prints, astro-ph/0312205
- King, I. 1962, AJ, 67, 471
- Kroupa, P. 2002, Science, 296, 82
- Kuntz, K. D. 2001, Ph.D. Thesis, Department of Astronomy, University of Maryland College Park
- Laor, A., Fiore, F., Elvis, M., Wilkes, B. J., & McDowell, J. C. 1997, ApJ, 477, 93
- Lodders, K. 2003, ApJ, 591, 1220
- Loewenstein, M. & Mushotzky, R. F. 1996, ApJ, 466, 695
- Loewenstein, M. 2001, ApJ, 557, 573
- D. A. Marks. Ph.D. thesis. University of Arizona, 2000.
- Mathis, J. S. 1996, ApJ, 472, 643
- Matsumoto, H., Koyama, K., Awaki, H., Tomida, H., Tsuru, T., Mushotzky, R., &

- Hatsukade, I. 1996, PASJ, 48, 201
- Matsushita, K., Finoguenov, A., & Böhringer, H. 2003, A&A, 401, 443
- Meyer, D. M., Jura, M., Hawkins, I., & Cardelli, J. A. 1994, ApJ, 437, L59
- Mitchell, R. J., Culhane, J. L., Davison, P. J. N., & Ives, J. C. 1976, MNRAS, 175, 29P
- Molendi, S. & Gastaldello, F. 2001, A&A, 375, L14
- Moos, H. W. et al. 2002, ApJS, 140, 3
- Mori, K. et al. 2000, Proc. SPIE, 4012, 539
- Mushotzky, R. F. & Loewenstein, M. 1997, ApJ, 481, L63
- Mushotzky, R. F., Serlemitsos, P. J., Boldt, E. A., Holt, S. S., & Smith, B. W. 1978, ApJ, 225, 21
- Mushotzky, R. F., Holt, S. S., Boldt, E. A., Serlemitsos, P. J., & Smith, B. W. 1981, ApJ, 244, L47
- Mushotzky, R., Loewenstein, M., Arnaud, K. A., Tamura, T., Fukazawa, Y., Matsushita, K., Kikuchi, K., & Hatsukade, I. 1996, ApJ, 466, 686
- Mushotzky, R. F. 1983, Presented at the Workshop on Hot Astrophys. Plasmas, Nice, 8-10 Nov. 1982, 83, 33826
- Nakamura, T., Umeda, H., Nomoto, K., Thielemann, F., & Burrows, A. 1999, ApJ, 517, 193
- Navarro, J. F., Frenk, C. S., & White, S. D. M. 1997, ApJ, 490, 493
- Nomoto, K., Hashimoto, M., Tsujimoto, T., Thielemann, F.-K., Kishimoto, N., Kubo, Y., & Nakasato, N. 1997, Nuclear Physics A, 616, 79
- Nomoto, K., Iwamoto, K., Nakasato, N., Hashimoto, Thielemann, F.-K., Brachwitz, F., Tsujimoto, T., Kubo, Y., & Kishimoto, N. 1997, Nuclear Physics A, 621, 467
- Y. Ogasaka et al., “Supermirror hard X-ray telescope and the results of first observation flight of Infocus,” in *X-Ray and Gamma-Ray Telescopes and Instruments*

- for Astronomy*, J. Truemper, H. Tannanbaum, eds., *Proc. SPIE* **4851**, 2002.
- T. Okajima et al., “Characterization of the supermirror hard X-ray telescope for the Infocus balloon experiment,” *Applied optics*, in press, 2002.
- Oliveira, C. M., Hébrard, G., Howk, J. C., Kruk, J. W., Chayer, P., & Moos, H. W. 2003, *ApJ*, 587, 235
- Ostriker, J. P. & Gnedin, N. Y. 1996, *ApJ*, 472, L63
- S. Owens et al., “Characterization and performance of the Infocus 20-40 keV X-ray focusing mirror,” in *X-Ray Optics for Astronomy: Telescopes, Multilayers, Spectrometers, and Missions*, P. Gorenstein; R. Hoover, eds., *Proc. SPIE* **4496**, p. 115–126, 2002.
- Paerels, F. et al. 2001, *ApJ*, 546, 338
- Page, M. J., Soria, R., Wu, K., Mason, K. O., Cordova, F. A., & Friedhorsky, W. C. 2003, *MNRAS*, 345, 639
- B. Parker et al., “Effect of twin boundaries on the spectroscopic performance of CdZnTe detectors,” in *Hard X-Ray and Gamma-Ray Detector Physics III*, R. James ed., *Proc. SPIE* **4508**, p. 68–78, 2001.
- B. Parker et al., “Correlation between bulk material defects and spectroscopic response in cadmium zinc telluride detectors,” in *Hard X-Ray, Gamma-Ray, and Neutron Detector Physics*, R. James, R. Schirato, eds., *Proc. SPIE* **3768**, p. 129–137, 1999.
- Peimbert, M., Carigi, L., & Peimbert, A. 2001, *Astrophysics and Space Science Supplement*, 277, 147
- Peterson, J. R., Kahn, S. M., Paerels, F. B. S., Kaastra, J. S., Tamura, T., Bleeker, J. A. M., Ferrigno, C., & Jernigan, J. G. 2002, *ArXiv Astrophysics e-prints*, 10662
- Peterson, J. R., Kahn, S. M., Paerels, F. B. S., Kaastra, J. S., Tamura, T., Bleeker, J. A. M., Ferrigno, C., & Jernigan, J. G. 2003, *ApJ*, 590, 207

- Pettini, M., Rix, S. A., Steidel, C. C., Adelberger, K. L., Hunt, M. P., & Shapley, A. E. 2002, *ApJ*, 569, 742
- Pilyugin, L. S., Ferrini, F., & Shkvarun, R. V. 2003, *A&A*, 401, 557
- Pipino, A., Matteucci, F., Borgani, S., & Biviano, A. 2002, *New Astronomy*, 7, 227
- Pompeia, L., Barbuy, B., & Grenon, M. 2003, *ArXiv Astrophysics e-prints*, 04282
- Ponman, T. J., Sanderson, A. J. R., & Finoguenov, A. 2003, *MNRAS*, 343, 331
- Pratt, G. W. & Arnaud, M. 2003, *A&A*, 408, 1
- Prochaska, J. X. & Wolfe, A. M. 2002, *ApJ*, 566, 68
- Prochaska, J. X., Naumov, S. O., Carney, B. W., McWilliam, A., & Wolfe, A. M. 2000, *AJ*, 120, 2513
- Rauscher, T., Heger, A., Hoffman, R. D., & Woosley, S. E. 2002, *ApJ*, 576, 323
- Rothenflug, R., Vigroux, L., Mushotzky, R. F., & Holt, S. S. 1984, *ApJ*, 279, 53
- R. Rothschild et al., “Actively shielded CZT focal plane detectors for the Fine Angular Resolution X-ray Imaging Telescope (FAR\_XITE),” in *EUV, X-Ray, and Gamma-Ray Instrumentation for Astronomy X*, O. Siegmund, K. Flanagan, eds., *Proc. SPIE* **3765**, p. 360–367, 1999.
- Rybicki, G. B. & Lightman, A. P. 1979, New York, Wiley-Interscience, 1979. 393 p.160
- Sakelliou, I. et al. 2002, *A&A*, 391, 903
- Sarazin, C. L. 1988, Cambridge Astrophysics Series, Cambridge: Cambridge University Press, 1988
- Savage, B. D., Drake, J. F., Budich, W., & Bohlin, R. C. 1977, *ApJ*, 216, 291
- Schaye, J., Aguirre, A., Kim, T., Theuns, T., Rauch, M., & Sargent, W. L. W. 2003, *ApJ*, 596, 768
- Schlegel, D. J., Finkbeiner, D. P., & Davis, M. 1998, *ApJ*, 500, 525
- Serlemitsos, P. J., Smith, B. W., Boldt, E. A., Holt, S. S., & Swank, J. H. 1977,

- ApJ, 211, L63
- K. Slavis et al., “High-altitude balloon flight of CdZnTe detectors for high-energy X-ray astronomy: II,” in *EUUV, X-Ray, and Gamma-Ray Instrumentation for Astronomy X*, O. Siegmund, K. Flanagan, eds., *Proc. SPIE* **3765**, p. 397–406, 1999.
- Smith, R. K., Brickhouse, N. S., Liedahl, D. A., & Raymond, J. S. 2001, ApJ, 556, 91
- Smith, R. K., Brickhouse, N. S., Liedahl, D. A., & Raymond, J. C. 2001, ApJ, 556, L91
- Sofia, U. J. & Meyer, D. M. 2001, ApJ, 554, L221
- Songaila, A. & Cowie, L. L. 2002, AJ, 123, 2183
- Songaila, A. 2001, ApJ, 561, L153
- Stasinska, G. 2002, ArXiv Astrophysics e-prints, 7500
- Strasser, S. T. & Taylor, A. R. 2004, ArXiv Astrophysics e-prints, astro-ph/0401248
- T. Takahashi et al., “High-resolution CdTe detector and applications to imaging devices,” in *IEEE Transactions on Nuclear Science* **48**, no. 3, p. 287, 2001.
- Tamura, T., Bleeker, J. A. M., Kaastra, J. S., Ferrigno, C., & Molendi, S. 2001, A&A, 379, 107
- Tanaka, Y., Inoue, H., & Holt, S. S. 1994, PASJ, 46, L37
- Thielemann, F., Nomoto, K., & Hashimoto, M. 1996, ApJ, 460, 408
- Timmes, F. X., Woosley, S. E., & Weaver, T. A. 1995, ApJS, 98, 617
- Verner, D. A., Ferland, G. J., Korista, K. T., & Yakovlev, D. G. 1996, ApJ, 465, 487
- Vuong, M. H., Montmerle, T., Grosso, N., Feigelson, E. D., Verstraete, L., & Ozawa, H. 2003, A&A, 408, 581
- Weisskopf, M. C., O’Dell, S. L., Paerels, F., Elsner, R. F., Becker, W., Tennant, A. F., & Swartz, D. A. 2004, ApJ, 601, 1050

- Willingale, R., Aschenbach, B., Griffiths, R. G., Sembay, S., Warwick, R. S., Becker, W., Abbey, A. F., & Bonnet-Bidaud, J.-M. 2001, *A&A*, 365, L212
- Wilms, J., Allen, A., & McCray, R. 2000, *ApJ*, 542, 914
- Wolfire, M. G., McKee, C. F., Hollenbach, D., & Tielens, A. G. G. M. 2003, *ApJ*, 587, 278
- Woosley, S. E. & Weaver, T. A. 1995, *ApJS*, 101, 181
- Yaqoob, T. and the *ASCA* team. *ASCA GOF Calibration Memo* (*ASCA-CAL-00-06-01*, v1.0 06/05/00)
- Zwicky, F. 1937, *ApJ*, 86, 217
- de Vries, C. P., den Herder, J. W., Kaastra, J. S., Paerels, F. B., den Boggende, A. J., & Rasmussen, A. P. 2003, *A&A*, 404, 959